ENGINEERED CARBON MATERIALS WITH NANO-GRAPHITIC DOMAINS DERIVED FROM LIGNIN

A Dissertation Presented for the
Doctor of Philosophy
Degree
The University of Tennessee, Knoxville

Valerie García Negrón
December 2020

Copyright © 2020 by Valerie García Negrón
All rights reserved.

DEDICATION

To my parents, Alberto E. García Pérez and Idalia Negrón Oquendo, thank you for your support and love. Also, my fiancé Eduardo M. Ponce Mojica, thank you for joining me in this journey, for your love, caring, and discipline.

ACKNOWLEDGMENTS

I would like to thank the following individuals for research support: My committee members, Professor David P. Harper, Professor David. J. Keffer, Professor Claudia Rawn, and Professor Orlando Rios, for providing guidance and support during my doctoral preparation. I would like to acknowledge their individual time, patience, guidance, and wisdom for the preparation of this work during my education. The support of the faculty and staff from the Center for Renewable Carbon and the Materials Science and Engineering Department at the University of Tennessee. Lastly, my research group, the students and staff group for their research contribution and support.

I am sincerely thankful for all the unique experiences I encounter during my doctoral career. It has been an honor and a great pleasure to work with each of you.

ABSTRACT

This work focuses on establishing a comprehensive understanding of lignin-derived materials as a function of carbonization with the goal of identifying processing-structure-property-performance relationships. A combination of modeling, statistical, and empirical materials characterization techniques are applied to lignin materials varying in feedstock source, extraction method, and processing conditions. The first part of this study evaluates the structure of carbon composite materials, possessing both crystalline and amorphous domains, using scattering techniques. One approach performs atomistic simulations of a proposed structure, from which the analogous scattering pattern can be obtained for validation. An alternative approach based on a hierarchical decomposition of the radial distribution function is used to generate a physics-based model allowing rapid interpretation of scattering data. The model is compared with atomistic simulation results in order to demonstrate that the contributions of the crystalline and amorphous domains, as well as their interfaces, are correctly captured. Present-day challenges exist in understanding how the distribution of monomeric units in lignin feedstocks impacts the structure and properties of carbon composites as a function of processing. The effect of lignin feedstock and processing conditions on the structure of carbon composites is studied. X-ray data was collected at a synchrotron source for lignin from hardwood, softwood, and grass feedstocks, processed under varying temperature and environmental conditions. The changes in the pair distribution function correspond to changes in material structure and it supports the observation that graphitic structures form and grow in size with increasing reduction temperature. The third part of this study resolves the structure of lignin carbon composites using small and wide angle x-ray scattering techniques. The study will help describe particles and aggregates in the lignin carbon structure. In this experiment complementary SAS techniques helps visualize voids and lignin structure as function of carbonization. Ultimately, this work enriches the understanding of controlling lignin feedstocks derived carbon product to support and develop products from systems that are sustainable and based on renewable resources. Results will help tune lignin carbon production to enable high-quality materials with targeted nanostructure for application in areas that are rapidly expanding such as advanced materials, energy storage, and biochemicals.

TABLE OF CONTENTS

CHAPTER 1: INTRODUCTION **1**

1.1 Lignin in nature 2
1.2 Extraction of feedstocks 2
1.3 Commercial Impact and Applications 4
1.4 Motivation and Objectives 5
1.5 Research Chapter Summaries 8
1.5.1 Chapter 2: Evaluation of Nano- and Mesoscale Structural Features in Composite Materials through Hierarchical Decomposition of the Radial Distribution Function 8
1.5.2 Chapter 3: Elucidating Nano- and Meso- Structure in Lignin-Based CarbonComposites: A Comprehensive Study of Feedstock and Temperature 8
1.5.3 Chapter 4: Small and Wide angle X-ray scattering of lignin-derived carbon composites 9

CHAPTER 2: EVALUATION OF NANO- AND MESOSCALE STRUCTURAL FEATURES IN COMPOSITE MATERIALS THROUGH HIERARCHICAL DECOMPOSITION OF THE RADIAL DISTRIBUTION FUNCTION **10**

2.1 Introduction 11
2.2 Model Development and Applications 15
2.2.1 General Form of the Decomposition 15
2.2.2 Description of Components at the Atomic Level 18
2.2.3 Amorphous-amorphous, Intraplanar (AA, intraP) 19
2.2.4 Crystalline-crystalline, Intracrystallite, Intraplanar (CC, intraC,intraP) 22
2.2.5 Description of Components at the Mesoscale 24
2.2.5.1 Crystalline-crystalline, Intracrystallite, Interplanar (CC, intraC, interP) 24
2.2.5.2 Crystalline-crystalline, Intercrystallite (CC, interC) 25

2.2.6 Contributions Described with Perturbations to a Mean Field 29
2.2.6.1 Amorphous-amorphous, Interplanar (AA, interP) 31
2.2.6.2 Amorphous-crystalline (AC) 34
2.2.7 Total RDF 34
2.2.8 Conclusion 37

CHAPTER 3: ELUCIDATING NANO- AND MESO- STRUCTURE IN LIGNIN-BASED CARBON COMPOSITES: A COMPREHENSIVE STUDY OF FEEDSTOCK AND TEMPERATURE 39

3.1 Introduction 40
3.2 Experimental Section 43
3.2.1 Processing 43
3.2.1.1 Feedstock Extraction 43
3.2.1.2 Carbonization 44
3.2.2 Material Characterization 44
3.2.2.1 APS X-ray Data 44
3.2.2.2 Lignin NMR Spectroscopy 46
3.2.2.3 Transmission Electron Microscopy 46
3.3 Results and Discussion 47
3.3.1 Control of Crystallite Size 52
3.3.2 Effect of Reduction Temperature 54
3.3.3 Correlated Effects 64
3.3.4 Atomic Structure in Carbon Composite 67
3.3.5 Effect of Moisture Content 70
3.3.6 Conclusion 74

CHAPTER 4: STRUCTURAL ANALYSIS OF CARBONIZED LIGNIN USING SMALL AND WIDE ANGLE X-RAY SCATTERING 76

4.1 Introduction 77
4.2 Experimental Methods 82
4.3 Results and Discussion 83
4.3.1 Analysis of Lignin as Function of Feedstock 86
4.3.2 Analysis of Lignin as Function of Heat Treatment 93
4.3.3 Conclusion 98

CHAPTER 5: CONCLUSIONS **100**
5.1 Chapter Conclusions 101
5.1.1 HRDF Model Development for Carbon Composite 101
5.1.2 Structural Characterization of Lignin Carbon Composite 101
5.1.3 Feedstock and Processing Structure Analyses via X-ray Scattering for Lignin-Derived Carbon 102
5.2 Impact and Significance 103
5.3 Future Work 104

REFERENCES **107**

APPENDICES **126**
A Supplementary Data for Chapter 2 127
B Supplementary Data for Chapter 3 154

VITA **167**

LIST OF TABLES

Table 1-1. Global production of commercial lignin [36, 100, 158]. 6

Table 2-1. System parameters grouped by origin (experiment or model) or scale within the model. 20

Table 3-1. Crystallite size based on (002) plane for lignin carbons at processed reduction temperatures. 53

Table 3-2. Elemental analysis of lignin carbon composite at each processing condition. 62

Table 3-3. Aromatic constituents in lignin characterized via 2D-HSQC spectroscopy. 63

Table 3-4. Pore volume and surface area in pyrolyzed kraft softwood with different water content. 72

Table 4-1. Porod fits, $I \propto q^{-n}$, for intensity profile in SAXS for lignin carbon composite. 88

Table 4-2. Characterization of the crystal plane as a function of heat treatment in the (002) plane positioned at $q = 1.84$ $\mathring{A}^{-1}$ in graphite that is observed in the WAXS region [121]. Current results are compared with measurements from two references. 92

Table B-1. C-C distances from reference and experimental data of composites reduced at 1050, 1500, and 2000 °C. 157

Table B-2. 2D-NMR (^{13}C-^{1}H-HSQC) spectra of lignin feedstocks identifying the signal of principal groups. 161

LIST OF FIGURES

Figure 1-1. Principal monomeric units found in lignin structure. 3

Figure 1-2. Hexagonal graphite crystal structure composed of stacked graphene layers. 7

Figure 2-1. Model structure and the general formulation of the hierarchical decomposition of a carbon composite. (a) Structural model of lignin-derived carbon composite used as a battery anode material consisting of crystalline graphitic nanoparticles (in grey) distributed in a matrix of amorphous carbon (in blue). Terminating hydrogen atoms are not shown. (b) Schematic of the six components of the hierarchical decomposition of the structure. 17

Figure 2-2. Comparison of the model and simulation RDF for the amorphous-amorphous intraplanar (*AA intraP*) in the three different composites. Note that the reported temperature corresponds to processing conditions. All RDFs were measured at room temperature. 21

Figure 2-3. Comparison of the model and simulation RDF for the crystalline-crystalline intracrystallite intraplanar (*CC intraC intraP*) in the three different composites. Note that the reported temperature corresponds to processing conditions. All RDFs were measured at room temperature. 23

Figure 2-4. (a) A typical example of an RDF due to a single pair of planes, with $r_{p,1} = 10.0$ Å, $r_{p,2} = 15.0$ Å and $d_p = 3.4$ Å. (b) Schematic of single crystallite displaying model mesoscale distribution of discs. 26

Figure 2-5. Comparison of the model and simulation RDF for the crystalline-crystalline intracrystallite interplanar (*CC intraC interP*) in the three different composites. Note that the reported temperature corresponds to processing conditions. All RDFs were measured at room temperature. The composite processed at 2000 °C corresponds to the schematic of Figure 2-4b. 27

Figure 2-6. (a) A typical example of an RDF due to a single pair of spheres, with $r_{c,1}$ = 10.0 Å, $r_{c,2}$ = 10.0 Å, and d_c = 25.0 Å. (b) A typical mesoscale distribution of spheres and the convolution of the single pair RDF in (a) with the mesoscale distribution. 28

Figure 2-7. Comparison of the model and simulation RDF for the crystalline-crystalline inter-crystallite (*CC interC*) in the three different composites. Note that the reported temperature corresponds to processing conditions. All RDFs were measured at room temperature. 30

Figure 2-8. Schematic of amorphous-amorphous, interplanar modeling approach. (a) The impact of atomic excluded volume (AEV) and mesoscale excluded volume (MEV) on the mean field approximation. (b) A typical diffuse interface modeled as a linear weighting of the amorphous contribution from Figure 2-8(a) and the crystalline contribution from Figure 2-5 (2000 °C).. 32

Figure 2-9. Comparison of the model and simulation RDF for the amorphous-amorphous interplanar (*AA, interP*) in the three different composites. Note that the reported temperature corresponds to processing conditions. All RDFs were measured at room temperature. 33

Figure 2-10. Comparison of the model and simulation RDF for the amorphous-crystalline (*AC*) in the three different composites. Note that the reported temperature corresponds to processing conditions. All RDFs were measured at room temperature. 35

Figure 2-11. Comparison of the total RDF from the model to results from MD simulation and NS experiments in the three different composites. Note that the reported temperature corresponds to processing conditions. All RDFs were measured at room temperature. Two model RDFs are shown. The first model, denoted "model-simulation" is parameterized to simulation and is the sum of components shown in Figures 2-2, 2-3, 2-5, 2-7, 2-9 and 2-10. The second model, denoted "model-experiment", otherwise functionally identical, is further optimized to the experimental data. 36

Figure 3-1. Pair distribution functions of three samples of switchgrass carbon composites reduced at 2000 °C. 45

Figure 3-2. Comparison of reduced lignin carbon composites. 48
Figure 3-3. Processed lignin carbons as a function of carbonization stages. 50
Figure 3-4. Example of KSW lignin during carbonization at reduction temperatures of 1050, 1500, and 2000 °C. 55
Figure 3-5. Pair distribution functions of reduced carbon composites. 56
Figure 3-6. PDFs of reduced carbon composites 0 to 10 Å and carbon-carbon neighbors in hexagonal plane of graphite [56]. C-C distance pairs from an intracrystalline-intraplanar model (dashed lines) are overlaid with the PDFs [54]. 58
Figure 3-7. Envelope shapes of $r^2G(r)$ for lignin carbons reduced at 1050 (left column) and 2000 °C (right column). A left arrow (dotted line) outlines the general trends of PDF data and is used to gain insights on structural coherence at respective radial distances. Appendix B includes plots for graphite and carbon composite reduced at 1500 °C. 60
Figure 3-8. PDF carbon composites projected on first pair of principal components: a) pyrolysis, b) reduced temperature of 1050 °C, c) reduction temperatures of 1050, 1500, and 2000 °C, and d) reduced temperature of 2000 °C. Duplicate symbols represent processed samples that were repeated. RT refers to a water content of 18 g m^{-3} and HT to 105 g m^{-3}. Variance explained by each principal component: a) PC-1 (80%), PC-2 (12%), b) PC-1 (66%), PC-2 (27%), c) PC-1 (64%) , PC-2 (30%), and d) PC-1 (43%), PC-2 (26%). 65
Figure 3-9. Correlations of $G(r)$ for lignin feedstock with respect to reduction temperatures. The coefficients correspond to a Pearson (linear) correlation for each radial position. 66
Figure 3-10. HR-TEM images and diffraction patterns of carbon composites reduced at 1050 and 2000 °C. 68
Figure 3-11. Diffracted patterns with indexed Bragg peaks of carbon composites reduced at 1050 and 2000 °C. Lines in red represent the graphite model fitted to the diffract patterns of carbon composites. The yellow line represents the actual data converted to Cartesian coordinates. 69

Figure 3-12. X-ray diffraction of kraft softwood at increasing water densities: 0, 18, 45, 75, and 105 $g\,m^{-3}$ during pyrolysis collected at a synchrotron source. 71
Figure 3-13. SEM micrographs show structural morphology of kraft softwood under pyrolysis at increasing water densities: 0, 18, 45, 75, and 105 $g\,m^{-3}$. A micrograph after ball milled (ABM 105 $g\,m^{-3}$) confirms particle size distribution. 73
Figure 4-1. Representative SAXS and WAXS log-log intensity profile of lignin powder carbons reduced at 1500–2000 °C for the range of $0.005 \leq q \leq 2.68$ Å. Hierarchichal structures are associated with different characteristic lengths. SAXS region describes graphene stacking in the mesoscopic regime. The mesoscopic region is further subdivided into three levels (L1–L3) where Porod fits show power law dependences. At high q, the WAXS region clearly presents the graphitic peak of plane (002). 84
Figure 4-2. Guinier plots at $0.005 \leq q \leq 0.01$ $Å^{-1}$ for KSW lignin powder sample presenting particle aggregation characteristics. The intensity profile of graphite is included as reference. 85
Figure 4-3. Log-log intensity profile of SAXS for raw and carbonized lignin powders. The intensity profile of graphite is included as reference. 87
Figure 4-4. Log-log intensity profile of WAXS for raw and carbonized lignin powders. The intensity profile of graphite is included as reference. 91
Figure 4-5. SAXS log-log intensity profiles for all lignin-derived powder samples. Fluctuations in scattering signal increase during carbonization among a single lignin feedstock evidencing partial graphitization. 95
Figure 4-6. WAXS log-log intensity profiles for all lignin-derived powder samples. Fluctuations in scattering signal increase during carbonization among a single lignin feedstock evidencing partial graphitization. 96

Figure 4-7. Log-log intensity profile of scattering data measured at BNL and Advanced Photon Source for KSW reduced at 1050 °C. The APS data was collected in 2θ, converted to q in the range of $1.78 \leq q \leq 6.2$ Å^{-1}, and merged. At high q the graphitic peaks corresponding to crystallographic planes (002), (010), (011), and (014) are present. Additional small peaks are due to contaminants from ball milling (Fe), refer to Figure 2 from [55]. 97

Figure B-1. PDF of carbon composites pyrolyzed in wet nitrogen with water density of 105 g m^{-3} and reduced at (top) 1050 °C, (middle) 1500 °C, and (bottom) 2000 °C. 155

Figure B-2. Pair distribution functions of kraft softwood at increasing water densities: 0, 18, 45, 75, and 105 g m^{-3} during pyrolysis and after reduced at (top) 1050 °C, (middle) 1500 °C, and (bottom) 2000 °C collected at a synchrotron source. 156

Figure B-3. a) Correlations of $G(r)$ for lignin feedstock with respect to humidity (water density). The coefficients correspond to a Pearson (linear) correlation for each radial position. Contrary to statistical analyses of temperature, humidity correlations of PDFs do not show a clear trend among the different lignin feedstocks. SG is the only feedstock to produce multiple high positive and negative correlations. we know that humidity manipulates microstructure (density of pores and sizes)..... 158

Figure B-4. ^{1}H-NMR spectra of lignin feedstocks (KSW, HW, SW, and SG) with typical functional groups in lignin. 159

Figure B-5. Aromatic region, side chain region, and alkyl region from ^{13}C-^{1}H (HSQC) spectra of all lignin feedstocks. Syringyl (S) unit, guaiacyl (G) unit, *p*-hydroxyphenyl (H) unit, para-coumarates (pCA), methoxy (OMe), dimethyl sulfoside deuterated (DMSO)..... 160

Figure B-6. Explained variances against principal components of a) pyrolyzed, b) all lignin reduced to 1050 °C, c) all lignin reduced to 2000 °C, and d) all lignin reduced to temperatures of 1050, 1500, and 2000 °C. These results are part of PCA shown in Figure 3-8. 163

Figure B-7. Loadings against radial distance of each principal components of a) pyrolyzed, b) all lignin reduced to 1050 °C, c) all lignin reduced to 2000 °C, and d) all lignin reduced to temperatures of 1050, 1500, and 2000 °C. These results are part of PCA shown in Figure 3-8. 164

Figure B-8. Envelope function of $r^2G(r)$ for graphite standard and lignin carbons reduced at 1500 °C. 165

Figure B-9. Kraft softwood lignin under pyrolysis to different water content evaluating isotherms during desorption and adsorption respect to relative pressure..... 166

CHAPTER 1
INTRODUCTION

1.1 Lignin in nature

Lignin is an organic polymer found mostly in the middle lamella and cell walls of plants, embedded along with other polymers and polysaccharides, and is a component that helps the plant's structural configuration by affecting stiffness, stability, and flexibility [141]. The complex, cross-linked, aromatic, and amorphous structure of lignin is made up of phenolic constituents, carbon-carbon bonds, and ether bonds. Functional groups are attached to the phenyl popanoid skeleton, leading to the benzyl hydroxyl, carbonyl, and phenolic hydroxyl groups. The frequency of these groups varies with wood species and extraction method [97]. Depending on the wood source, the content of lignin monomeric units varies in *p*-coumaryl alcohols, coniferyl alcohol, and sinapyl alcohol. Phenolic units precursors form *p*-hydroxyphenyl (H), guaiacyl (G), and syringyl (S) (Figure 1-1). The principal lignin types analyzed in this work are: indulin AT softwood, southern yellow pine softwood, yellow poplar hardwood, and swithchgrass.

The content of lignin varies between plant species. For example, hardwoods have 18–25%, softwoods have 25–35%, and switchgrasses contain 17–24%. Also, the quality or composition of lignin differs among plants based on factors such as species and age. Gymnosperms primarily contain coniferyl alcohol or guaiacyl units (G). Angiosperms contain coniferyl alcohol and sinapyl alcohol (G and S). Grasses primarily contains *p*-coumaryl alcohol (H). In other words, softwoods mainly have G units with small amount of H, hardwoods have S and G in various proportions, and grasses contain G, H, and S units [62, 90]. Lignin is a natural and major source of carbon with added-value to commercial applications [58].

1.2 Extraction of feedstocks

Multiple methods to extract lignin from plants are available, which in turn produce black liquors of different composition and containing lignin of varying properties and purity [100]. The following list describes the most common extraction methods for lignin feedstocks [65, 97].

- **Lignosulfonate or Sulfite Lignin:** Sulfite pulping is a chemical process that bleaches pulp grade wood for paper products using sulfurous acid salts and generates lignin as a by-product [68]. Lignin is recovered from the spent pulping liquids. Current global production is about 1 million metric tonnes per year. Lignosulfonates are soluble in water and can be used in soaps and other detergent products.

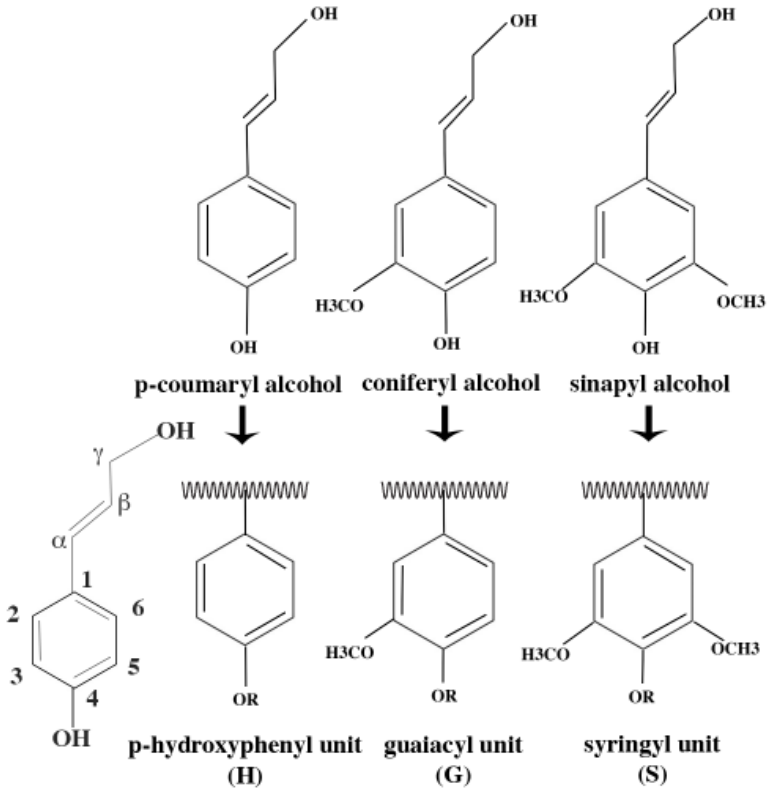


Figure 1-1. Principal monomeric units found in lignin structure.

- **Kraft Sulfate Pulping:** Kraft pulping is used for commercial paper production and is also consider a chemical pulping. This method utilizes sodium sulfide as catalyst to separate the organic lignin from the plant cellulose. The lignin to be extracted undergoes processing during paper-production stages. The lignin is captured in the black liquor and is typically recovered only to be burned on-site for energy. The neutralization of the phenolic hydroxyl groups in lignin occurs when the pH level is in the range of 10.5–11, then a precipitated and concentrated liquor is obtained. The isolation consists of acidification, filtration, and washing. During the aforementioned steps the black liquor is acidified with mineral acids (sulfuric and hydrochloric acid) followed by filtration to obtain pure lignin that is then typically suctioned and washed with water [97]. Lignin produced through this process typically contains some residual sulfur contamination [47].

- **Organosolv Lignin:** The lignin is recovered via pulping liquor by precipitation in water from organic solvents. Acid is use as catalyst at high temperature and under pressure followed by a salt and water separation. The clean fractions make organosolv an attractive method that can target high-value applications when compared to kraft pulping. However, it has not achieved a high rate of commercial use.

- **Soda Lignin:** The soda lignin is derived from the soda anthraquinone process and is mainly industrialized for non-wood fiber products. It is a chemical process where wood pulp is cooked with sodium hydroxide. The alkaline pulping process is then converted to kraft pulping due to its stronger pulp and energy efficiency. However, biorefineries are using this process due to its ability to produce sulfur-free lignin and crystalline cellulose. Sodium hydroxide decreases the carbohydrate degradation. The soda process produces a high yield of hardwood pulps, and the black liquor is mainly used for energy recovery [5].

This work focuses on kraft and organosolv fractionation as feedstock extraction methods given that the former is an accessible recyclable byproduct of pulp industry and the latter can be made in-house with high purity.

1.3 Commercial Impact and Applications

The abundant organic polymer has unique and large aromatic structures that make it suitable for a wide range of applications. Nowadays, lignin material is synthesized and chemically manipulated for applications such as: foams, carbon fibers, chemicals, batteries, fuels, bioplastics, adsorbents, dispersants, lubricants, and emulsifiers. Initiatives

and incentives for the development of bioeconomics that focus on the use of renewable products is calling attention to the production of bio-products such as lignin [14]. The use of raw materials rather than fossil materials couple with bio-based innovation is desired for upcoming technologies, which emphasize reduced carbon footprints. However, understanding the global system is important in the development of new methods for energy production. Promising solutions, such as using biomass instead of oil to produce heat and chemicals, fuels, and power, give rise to value-added products for example intermediate products such as: carbon fibers, dispersants, plastic materials, binders, and other end products like: activated carbon, sorbents, surfactant, and chemicals [6, 95]. These applications emphasize the use of lignin. Using such sustainable materials may have a positive impact on the economy and environment. Table 1-1 presents an estimate of the cost, quantity, and main producers of commercial lignin.

Lignin has a high concentration of carbon, thus, is suitable for producing domestic graphitic carbon materials. Under controlled processing conditions, lignin-based carbons form small graphitic crystals with high degree of crystallinity. Graphite is a parallel 2D carbon layer of carbons sp^2 hybrid bonding in aromatic rings, see Figure 1-2. The turbostratic structure in carbon occurs with random stacking layers as result of translation and rotation displacement. Graphite is attractive due to its electromagnetic properties and high thermal stability.

Graphite is used for a numerous applications: lubricants, pencils, refractory materials, steel industries, electronics, batteries, and carbon-based composites. Natural graphite can be found in three types: vein, flake, and microcrystalline or amorphous. The natural flake graphite tends to be high purity grade graphite and has desirable properties such as: size, softness, high heat conductivity, and high heat resistance. The high purity grade graphite enhances the efficiency of typical battery anodes [162]. Electrochemical storage applications and vehicular industries are examples of industries that can clearly benefit from a cheap and domestic source of lignin based carbon materials. This work extends the characterization of a carbon material produced from kraft lignin softwood, and the evaluation of its electrochemical properties as an anode in lithium-ion coin cells [53].

1.4 Motivation and Objectives

Understanding the atomic and microstructural properties of domestic renewable materials that can serve as graphite substitutes is an essential step towards low-cost and high-availability commercial carbon-based products.

Table 1-1. Global production of commercial lignin [36, 100, 158].

Extraction method	**Main producers**	**Cost (USD/ton)**	**Annual production (kilotons/yr)**
Lignosulfonates	Borregardi Lignotech, Tembec, and Nippon paper chemicals	180–500	250–2000
Kraft pulping	MeadWestvaco, Domtar (lignoboost)	260–585	60–250
Organosolv	Dedini, CIMv	280–615	3–25
Soda lignin	Northway lignin chemical, Green value	200–385	5–65

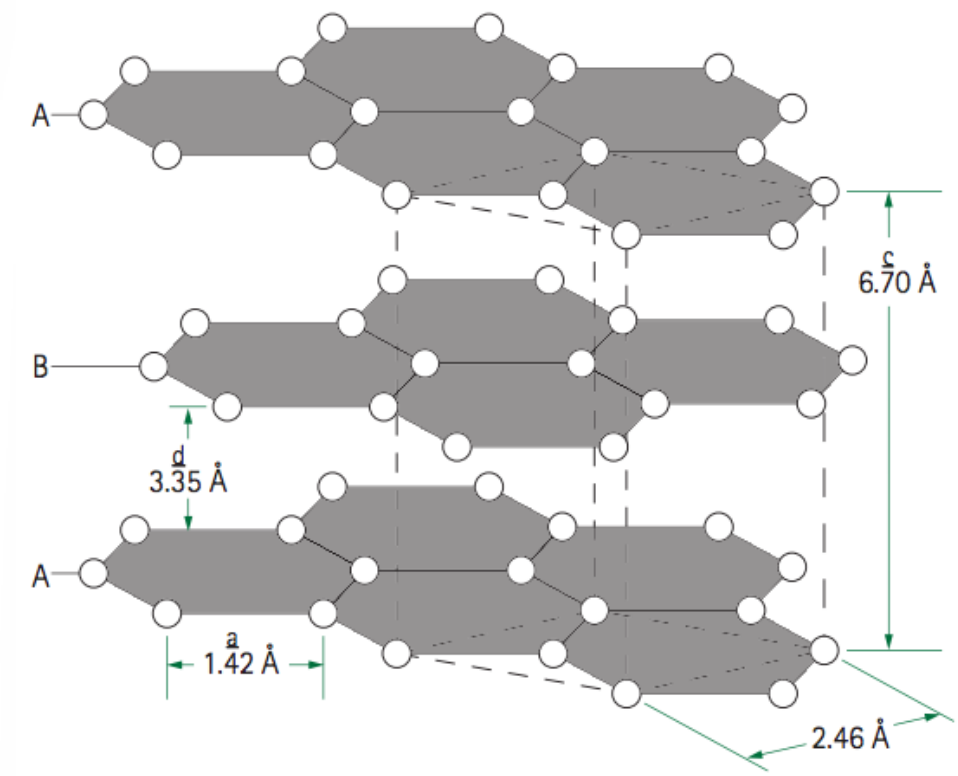


Figure 1-2. Hexagonal graphite crystal structure composed of stacked graphene layers.

The main goal is to synthesize in-house carbon materials from renewable sources to serve as substitutes for mineral and fossil derived carbon-based materials. This work presents a comprehensive evaluation of lignin feedstocks—kraft softwood, organosolv softwood, organosolv switchgrass, and organosolv hardwood—and their conversion into lignin carbon composites. The relationships between degrees of graphitization of lignin carbon products as a function of feedstock, processing conditions, and heat treatments are resolved. The resulting nanostructure composites are composed of graphitic crystallites and amorphous carbon domains as established by characterization techniques and a physics-based model of the radial distribution function.

1.5 Research Chapter Summaries

1.5.1 Chapter 2: Evaluation of Nano- and Mesoscale Structural Features in Composite Materials through Hierarchical Decomposition of the Radial Distribution Function

Composite materials possessing both crystalline and amorphous domains, when subjected to x-ray and neutron scattering, generate diffraction patterns that are often difficult to interpret. One approach is to perform atomistic simulations of a proposed structure, from which the analogous diffraction pattern can be obtained for validation. The structure can be iteratively refined until simulation and experiment agree. The practical drawback to this approach is the significant computational resources required for the simulations. In this work, an alternative approach based on a hierarchical decomposition of the radial distribution function is used to generate a physics-based model allowing rapid interpretation of scattering data. In order to demonstrate the breadth of this approach, it is applied to a series of carbon composites. The model is compared with atomistic simulation results in order to demonstrate that the contributions of the crystalline and amorphous domains, as well as their interfaces, are correctly captured. Because the model is more efficient, additional structural refinement is performed to increase the agreement of the simulation result with the experimental data. The model achieves a reduction in computational effort of six orders of magnitude relative to simulation. The model can be generally extended to other composite materials.

1.5.2 Chapter 3: Elucidating Nano- and Meso- Structure in Lignin-Based CarbonComposites: A Comprehensive Study of Feedstock and Temperature

The production of carbon materials from renewable biofeedstocks is rapidly expanding with commercial applications in the areas of advanced materials, energy storage, and

biochemicals. Present-day challenges exist in understanding how the distribution of monomeric units in lignin feedstocks impacts the structure and properties of carbon composites as a function of processing. This research investigates the effect of lignin feedstock and processing conditions on the structure of carbon composites. X-ray data was collected at a synchrotron source for lignin from hardwood, softwood, and grass feedstocks, processed under varying temperature and environmental conditions. The relative abundance of the principal monomeric units—guaiacyl, *p*-hydroxyphenyl, and syringyl—varies with feedstock and result in reproducible variations in the x-ray data. Statistical analysis for over fifty carbon materials was performed to determine the influence of feedstock, reduction temperature, and furnace humidity. The changes in the pair distribution function are then related to changes in material structure. The changes in the pair distribution function correspond to changes in material structure. Taken together, the analyses support the observation that graphitic structures form and grow in size with increasing reduction temperature. The characteristic size of the graphitic crystallites varies with feedstock, with kraft softwood and organosolv switchgrass leading to carbon composites with larger graphitic domains.

1.5.3 Chapter 4: Small and Wide angle X-ray scattering of lignin-derived carbon composites

Small and wide angle x-ray scattering were collected for powder lignin feedstocks—softwood, hardwood, and switchgrass—processed at different temperatures in order to resolve atomic and mesoscale features. The scattering analysis is a complementary technique that alllows us to obtain information regarding the surface roughness, structure, crystallite sizes, and interatomic distances. This work provides at different q-regions an insight of the nature of the lignin during processing the structure to carbon composites.

CHAPTER 2

EVALUATION OF NANO- AND MESOSCALE STRUCTURAL FEATURES IN COMPOSITE MATERIALS THROUGH HIERARCHICAL DECOMPOSITION OF THE RADIAL DISTRIBUTION FUNCTION

Chapter 2 includes an extended draft version of the of latest published article. The chapter includes introduction, model development and results, and conclusion. The latest version can be found in *Journal of Applied Crystallography* cited as:

"García Negrón, V., Oyedele, A. D., Ponce, E., Rios, O., Harper, D. P., & Keffer, D. J. (2018). *Evaluation of nano-and mesoscale structural features in composite materials through hierarchical decomposition of the radial distribution function*. Journal of Applied Crystallography, 51(1), 76–86."

Acknowledgements: This work acknowledges the research at Oak Ridge National Laboratory's Spallation Neutron Source was sponsored by the U.S. Department of Energy, Office of Basic Energy Sciences. Also, part of the research was sponsored by the Critical Materials Institute, an Energy Innovation Hub funded by the U.S. Department of Energy, Office of Energy Efficiency and Renewable Energy.

Abstract: Crystalline and amorphous domains in composite materials, when subjected to x-ray and neutron scattering, generate diffraction patterns that are often difficult to interpret. One approach is to perform atomistic simulations of a proposed structure, from which the analogous diffraction pattern can be obtained for validation. The structure can be iteratively refined until simulation and experiment agree. The practical drawback to this approach is the significant computational resources required for the simulations. An alternative approach based on a hierarchical decomposition of the radial distribution function is used to generate a physics-based model allowing rapid interpretation of scattering data. In order to demonstrate the breadth of this approach, it is applied to lignin carbon composites processed at high temperatures. The model is compared to atomistic simulation results in order to demonstrate that the contributions of the crystalline and amorphous domains, as well as their interfaces, are correctly captured. Because the model is more efficient, additional structural refinement is performed to increase the agreement of the simulation result with the experimental data. In this work the model achieves a reduction in computational effort of six orders of magnitude relative to simulation. The model can be broadly implemented to other composite materials.

2.1 Introduction

As part of the evolution in modern materials science one goal is to develop predictive processing-structure-property-performance (PSPP) relationships, in which the processing procedure determines the structure (at all scales including the atomistic, meso- and macro-scales). The structure in turn dictates the functional and structural properties of the material, which give rise to device or component performance. Without detailed understanding of structure, one has only an empirical processing–performance relationship (practically useful but not the end goal). In purely crystalline materials, well developed computational tools exist to process experimental data from diffraction experiments. Thus, delivering a definitive characterization of the structure of crystalline materials is relatively straightforward, since their structural information in one unit cell can be replicated at any length scale because of the perfect ordering present in their crystal lattice structure. However, for materials with a high degree of disorder, such as glass, organic polymers, nanocomposites, organic-inorganic perovskites, lignin, nanomagnets and memory polymers, the extraction of a definitive structure from experimental scattering data can be extraordinarily difficult, resulting in a crucial gap in the PSPP relationship [43, 113]. Studying these materials are of interest in the scientific community owing to their transformative potential in the field of advanced manufacturing,

pharmaceuticals, energy and defense [91]. One of the common forms in which x-ray scattering (XS) and neutron scattering (NS) reduce structural information is the radial distribution function (RDF), $g(r)$, where r is the separation between atoms. The RDF is the Fourier transform of the scattering signal, $S(Q)$. One can employ the RDF because it is experimentally accessible and it can be directly related to the probability distributions of statistical mechanics for liquids and other noncrystalline materials [106]. The RDF gives the conditional probability distribution of finding an atom at distance r given an arbitrary atom at the origin. The RDF results when the more general pair correlation function, $g(r_1, r_2)$, is applied to spatially homogeneous materials and averaged radially, $r = |r_1, r_2|$. The RDF represents a significant reduction in the degrees of freedom (DOF) used to describe structure. This reduction in DOF corresponds to a loss of information. For a three dimensional crystalline material with N_a atoms per unit cell, there are at most $N_{DOF}^{c,\,max} = 3N_a - 6$. The reduction by 6 accounts for arbitrary translation of and rotation about the center of mass; symmetry constraints may further significantly reduce the DOF. The DOF accounted for by $g(r)$ are at most $N_{DOF}^{g(r),\,max} = R_{max}/\delta r$, where δr is the discretization of the radial dimension and R_{max} is the maximum radial position at which the RDF is measured. A typical value of δr is 0.1 Å and a generous value of R_{max} is 50.0 Å, resulting in $N_{DOF}^{c,\,max} = 500$. Of course, not all of these DOF are independent since adjacent points along the RDF which describe common features (e.g., peaks or valleys) are highly correlated. For crystalline materials, it is often the case that $N_{DOF}^{c,\,max} \leq N_{DOF}^{g(r),\,max}$, which allows for routinely reliable extraction of atomic coordinates from the RDF. Such is not the case for complex or amorphous materials. In the amorphous case, the maximum number of independent atoms may well equal the number of atoms in the sample, resulting in an intractable number of DOF, $N_{DOF}^{a,\,max} \gg N_{DOF}^{g(r),\,max}$. In this case, there is insufficient information in the RDF to extract atomic coordinates from it. Of course, knowledge of the position of every atom is not essential to characterizing the structure of the material. Other, coarser-grained elements of structure may be invoked, which perform two tasks. First, coarse-grained or mesoscale structural elements reduce the DOF required to describe the structure. Second, when methodically implemented and accounted for, coarse-graining can provide materials scientists with the essential structural information required to generate predictive PSPP relationships. It is in this spirit that the pursuit of a hierarchical decomposition of the RDF is justified.

Current approaches to obtain structural information include the application of molecular dynamics simulation to interpret experimental scattering data. The comparison of experimental and simulated scattering data is relatively common for both x-ray and

neutron scattering. Typically, a model is proposed and the comparison is made between experiment and simulation without iterative refinement of the model, for example with x-ray [15, 21, 29, 34, 38, 44, 49, 64, 72, 108, 130, 151, 165] and neutron [8, 40, 41, 50, 63, 67, 92, 102, 104, 122, 123, 125, 128, 172] scattering. In fewer cases, some element of refinement of the structural parameters is included through an iterative refinement of the model, for example with x-ray [33, 78] and neutron [42, 89, 101] scattering. Complex materials with both nanoscale and mesoscale structure may require large systems in order to capture long-range order [102]. In such large-scale systems, molecular dynamics simulations typically require high-performance computing (HPC) resources and iterative refinement may be limited. Ongoing efforts to develop a general approach for extracting the structural information of complex materials via diffraction and scattering exist. *DISCUS* [120, 135], reverse Monte Carlo (RMC) [80, 88, 159, 160] and iterative PDF fitting software [45, 119, 133, 138] are examples of these approaches. The search for broadly applicable tools to extract structure from RDFs of complex materials remains an active research area. Recently, [117] proposed a hierarchical decomposition of the RDF, in which the total RDF was successively decomposed into components until a satisfactory atomistic or mesoscale model existed to generate each component. This hierarchical model was presented as a physics-based model free of arbitrary fitting parameters. However, experimentally, only the total RDF is available, making a decomposition approach susceptible to non-physical fitting optimization. In the initial application of the hierarchical decomposition of the RDF, the approach was applied to a carbon composite, in which both crystalline (graphitic) and amorphous domains were present. Molecular dynamics simulations of this system had been performed [102]. Unlike experiment, the arbitrary decomposition of the RDF is available from simulation. Thus, the hierarchically decomposed model could be successfully validated on a component-by-component basis. In this contribution we extend the hierarchical decomposition approach to a set of three carbon composites. Several structural variables change in these materials, including the volume fraction of the crystalline domain, the size of the graphitic nanocrystallites and the density of the material. These different composites were generated experimentally by changes in the processing conditions [157]. For all composites, both NS experiments at the Spallation Neutron Source (SNS) and molecular dynamics simulations have been performed and can be used for comparison [102]. While this article is limited to carbon composites, the hierarchical decomposition approach is directly applicable to any material in which crystalline nanoparticles are distributed in an amorphous domain or amorphous domains

are distributed in a polycrystalline material. In fact, in the three carbon composite samples upon which we report, the volume fraction of the crystalline domain ranges from 10 to 90%. Nanocomposites have shown interesting properties, including enhanced thermal conductivity, electronic conductivity and high surface area for energy storage applications [170]. The carbon composites in this work have application as anodes in Li-ion batteries [157]. Recent work has shown that the method of lithium-ion storage in these composites occurs via a fundamentally different mechanism than the intercalation in bulk graphite [104, 105]. These composite materials provide a demonstration of the ability of the hierarchical decomposition model to provide the structure that links the changes in processing to the observed electrochemical performance via the PSPP relationship. Before presenting the model, we should note that, given infinite computational resources and time, any coarse-grained model will provide a less accurate characterization of the structure than atomistic simulations. However, it is important to understand the iterative nature of the process of interpretation of experimental RDFs. An initial structure is guessed and the corresponding RDF is generated.

Comparisons of the experimental and simulated RDFs are made. On the basis of any discrepancy between the two RDFs, a refinement of the simulated structure is then proposed. Therefore, whether purely atomistic simulation or a hierarchical model is used, the successful convergence of the approach depends upon the number of iterations performed. If the atomistic simulations are computationally expensive, then perhaps only a single iteration is performed, as done by [102]. However, substantial reductions in the DOF of the hierarchical model can allow numerous iterations. The final accuracy of the simulation or model relative to the experiment is not exclusively a function of the DOF in each iteration, but is also a function of the degree of convergence due to the number of iterations performed. Oyedele et al. report a reduction in computational requirements of a factor of one million when moving from atomistic simulations to the hierarchical decomposition model; thus it is possible, as demonstrated below, for the hierarchical decomposition model to provide a better understanding of the structure than atomistic simulation alone [117].

Finally, from a practical point of view, since HPC resources are not ubiquitous, the hierarchical decomposition model provides a low-cost alternative that can be run on personal computers. In defense of atomistic simulation, we have developed the hierarchical decomposition model with information from simulation available to us. It is our intention that, in the future, such computationally expensive simulations will not always be required.

We accept the likely possibility that some new materials will be engineered with structures that initially require atomistic simulation to give insight into the structure, before the hierarchical decomposition model can be modified to accommodate such features. This approach may not work on all materials. Specifically, if a material does not possess hierarchical structure, then a hierarchical decomposition of the RDF will not be appropriate. In this work, we rapidly obtained the RDF of a lignin-based carbon composite via the hierarchical decomposition of the RDF. The hierarchy present in complex materials like carbon composites allows for the decomposition of their structures into components in which each component can be evaluated by theory. In the case of lignin, there are six components of the RDF, evaluated by either the atomic or the mesoscale [117]. We extend the hierarchical model to lignin pyrolyzed at three different temperatures, 1000, 1500, and 2000 °C. In the remainder of the article, we present the description of the decomposition, followed by the analysis of the decomposition components. In each component, the RDF obtained from the model is compared with that obtained from experiments and simulations for the three different composites processed under different temperature conditions. The characterization of the RDF in experiment, simulation and model is performed at room temperature.

2.2 Model Development and Applications

2.2.1 General Form of the Decomposition

To begin we consider a general, composite material composed of η_ϕ phases, α, β, γ, ...The total RDF of the composite material, $g_{tot}(r)$, a quantity available from XS or NS, can be decomposed into contributions from atom pairs based on the phase in which those atoms are located,

$$g_{tot}(r) = \sum_{\alpha=1}^{\eta_\phi} g^*_{\alpha\alpha}(r) + \sum_{\alpha=1}^{\eta_\phi - 1} \sum_{\beta \gtrsim \alpha}^{\eta_\phi} g^*_{\alpha\beta}(r) \tag{2.1}$$

where $g^*_{\alpha\beta}(r)$ represents the component of the RDF due to pairs of atoms in which one atom resides in phase α and the other in phase β. The asterisk is added to the components because, as will be seen in the specific example below, these component RDFs do not necessarily satisfy the rigorous definition for RDFs, which require that they be normalized such that they approach unity in the limit of infinite separation. The first term in equation 2.3 represents intraphase contributions to the RDF. The second term in equation 2.3 represents interphase contributions. This decomposition according to phases is sensible since theory is better

posed to provide the RDF of a single phase or an interaction between two phases than the total altogether. Several types of subsequent further decomposition are possible. If phase α is distributed in discrete domains, for example nanocrystallites in a continuous matrix of phase β, then $g^*_{\alpha\alpha}(r)$ can be further decomposed into intra-domain and inter-domain contributions.

$$g^*_{\alpha\alpha}(r) = g^*_{\alpha\alpha,intra}(r) + g^*_{\alpha\alpha,inter}(r) \tag{2.2}$$

Alternatively, if a phase contains a molecular component, then the formal decomposition in equation 2.2 may just as well correspond to intramolecular and intermolecular contributions to the RDF. In general, the decomposition must account for differences in scattering length density between different atoms. In the decompositions given above, the respective prefactors are absorbed in the individual components. The components are additive since there is only one type of atom present in the model, that is, carbon, therefore, there is only a single scattering length and no cross-terms. The goal of the decomposition is to render the total RDF in terms of components that can individually be evaluated with a simple, atomistic or mesoscale model or theory. The number of the levels in the hierarchy is chosen to meet this goal. In the carbon composite, there are three levels in the decomposition as shown in Figure 2-1. The first level of decomposition corresponds to equation 2.3 for a material with only two phases, crystalline (C) and amorphous (A), resulting in

$$g_{tot}(r) = g^*_{AA}(r) + g^*_{CC}(r) + g^*_{AC}(r) \tag{2.3}$$

We consider the crystalline phase to be dispersed into distinct nanocrystallites, thus we invoke equation 2.2 as a second decomposition of the CC term, in terms of intra-crystallite and intercrystallite components,

$$g_{CC}(r) = g^*_{CC,intraC}(r) + g^*_{CC,interC}(r) \tag{2.4}$$

Because the material in questions is highly aromatic carbon, the crystallites are graphitic. This is initially an assumption, but can be validated via comparison with experimental data. Thus $g^*_{CC,intraC}(r)$ can be decomposed at a third level into contributions arising from pairs of atoms within the same plane of graphene (intraplanar) and between planes of graphene (interplanar),

$$g^*_{CC,intraC}(r) = g^*_{CC,intraC,intraP}(r) + g^*_{CC,intraC,interP}(r) \tag{2.5}$$

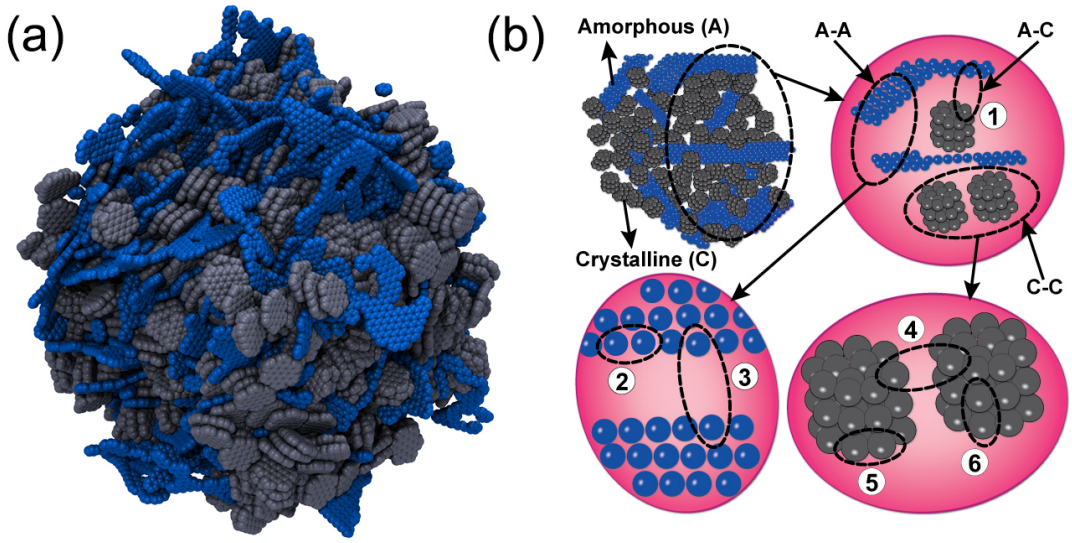


Figure 2-1. Model structure and the general formulation of the hierarchical decomposition of a carbon composite. (a) Structural model of lignin-derived carbon composite used as a battery anode material consisting of crystalline graphitic nanoparticles (in grey) distributed in a matrix of amorphous carbon (in blue). Terminating hydrogen atoms are not shown. (b) Schematic of the six components of the hierarchical decomposition of the structure.

For lithium-ion storage, the intercalation process distorts the graphitic crystal by increasing the planar separation. Decomposing the crystalline phase to a depth of three levels seemed appropriate to understand interactions in the stacked sheets of graphene. In general, the number of levels in the hierarchy of the decomposition depends upon the structure of the material. The amorphous phase is modeled as disordered aromatic carbon, or randomly oriented fragments of graphene. Various models of amorphous carbon exist. If the material is thought to be dominated by sp^2 bond hybridization, one can imagine randomly oriented sheets of graphene of finite size to which various defects have been added. Alternatively, if the sp^3 bond hybridization is dominant in the material, one can imagine amorphous carbon as a disordered diamond structure, in which numerous vacancies are present. In this application, there was experimental evidence for a high degree of aromaticity, which corresponds to the disordered graphene model. Thus the same decomposition used in the third level for the crystalline phase (equation 2.5), namely intraplanar and interplanar components, can be used at the second level for the amorphous domain.

$$g_{AA}(r) = g^*_{AA,intraP}(r) + g^*_{AA,interP}(r) \tag{2.6}$$

Substitution of equations (2.4) to (2.6) into equation 2.3 yields the 6 component decomposition of the total RDF,

$$\begin{aligned} g_{tot}(r) = {} & g^*_{AA,intraP}(r) + g^*_{AA,interP}(r) + g^*_{CC,intraC,intraP}(r) \\ & + g^*_{CC,intraC,interP}(r) + g^*_{AC}(r) \end{aligned} \tag{2.7}$$

2.2.2 Description of Components at the Atomic Level

Sharp peaks in the RDF that correspond to covalent bonds in a molecule or to short-range crystal structure require atomistic detail. In the carbon composite case, terms that describe the interactions between atoms within the same sheet of graphene (intraplanar) will result in sharp peaks that correspond to the rigid crystal structure of graphene. To evaluate terms, the equilibrium crystal structure is used as an input. Because the planes are finite, explicit evaluation of the RDF through pairwise summation is computationally tractable.

$$\begin{aligned} & g_{AA,intra}(r)^* = \\ & \frac{x_A}{\rho_{tot}} \frac{1}{4\pi r^2} \frac{2}{N_{app}} \sum_{i=1}^{N_{app-1}} \sum_{j=i+1}^{N_{app}} \delta(r' - r_{ij}) f_g(r - r'; \mu_g = r_{ij}, \sigma_g = \sigma_{T,intra}\sqrt{r_{ij}}) \end{aligned} \tag{2.8}$$

where N_{app} is the number of atoms per plane. The additional information that is required is a "mesoscopic parameter", the characteristic size and shape of the planes, which determine N_{app}. The size of the crystallites was estimated from peak widths obtained from x-ray scattering. The density, ρ_{tot}, was measured experimentally (see Table 2-1) and was specified for each composite without adjustment in this work. The weighting function for this component, the atom fraction of the amorphous domain, x_A, was determined from knowledge of the total density, the crystallite (graphite) density and the volume fraction of the crystalline domain, ϕ_C, which was measured experimentally in this work and is reported in Table 2-1. The amorphous fraction of the material was estimated based on visual inspection of micrographs, in which the crystalline and amorphous domains were distinguishable. If either ρ_{tot} or x_A is unavailable, they could be fit. The additional function, f_g, is a Gaussian distribution centered on each peak, $\mu_g = r_{ij}$, intended to provide thermal noise. It has associated with it a standard deviation that grows as the square root of the separation between atoms, $\sigma_g = \sigma_{T,intra}\sqrt{r_{ij}}$. The factor $\sigma_{T,intra}$ is the thermal standard deviation (units of Å) at a distance of $r = 1$ Å. This factor is the same for all composites studied here because it represents effect of the temperature at which the scattering experiment was performed, room temperature for all samples. The two components, $g_{AA,intraP}(r)^*$ and $g_{CC,intraC,intraP}(r)^*$, which are treated with atomistic detail, are described below.

2.2.3 Amorphous-amorphous, Intraplanar (AA, intraP)

The amorphous phase is modeled as randomly oriented fragments of graphene. While in both experiment and simulation, there is a distribution of fragment shapes and sizes, in the model only a single fragment with a given shape and size is used. This fragment is chosen to be ellipsoidal in shape. Figure 2-2, shows the results of this model, equation 2.8, compared to the atomistic simulation. For the model, the separation between atoms is taken from a static model of defect-free graphene using a bond length of 1.42 Å. For the atomistic simulation, an interaction potential was used (see [103]). The Gaussian was included for thermal noise in the model only. The atomistic simulations are run at a finite temperature and generate the corresponding thermal distribution. In Table 2-1, we present the values of the major and minor axes of the ellipsoids used to model this system. The comparison of model and simulation is excellent. Note that the radial separation is the same for each composite, but the radial distribution function varies, reflecting the different amorphous content in each composite. In Figure 2-2, every peak position is captured, confirming the presence of graphene fragments in the system.

Table 2-1. System parameters grouped by origin (experiment or model) or scale within the model.

Parameter	**Value**		
Pyrolysis temperature (°C) (experiment)	1000	1500	2000
Radius of crystallites (Å) (experiment)	5	7	17
Volume fraction of crystalline domain ϕ_C (experiment)	0.9	0.5	0.1
Total density (g cm^{-3}) (experiment)	1.94	1.51	1.38
Minor radius of graphene plane in A phase (Å)	2.5	4.0	15.0
Major radius of graphene plane in A phase (Å)	2.5	24.0	15.0
Intraplanar thermal noise $\sigma_{T,intra}$(Å)	0.025	0.025	0.025
Distance between planes in crystallite d_p (Å)	3.0	3.4	3.4
Number of planes per crystallite	3	3	9
Presence of density peak at close-packing	No	No	Yes
Fraction of RDF due to atomic packing step (*CC, interC*)	0.44	0.20	0
Fraction of RDF due to atomic packing step (*AA, interp*)	0.88	0.80	1.0
Interface width (Å) (*AA,interp*)	5	12	17
Initial crystalline fraction (*AA,interp*)	0.4	0.11	0.28
Fraction of RDF due to atomic packing step (*AC*)	0.84	0.70	0.08
Interface width (Å) (*AC*)	5	7	10
Initial crystalline fraction (*AC*)	0.4	0.1	1.0

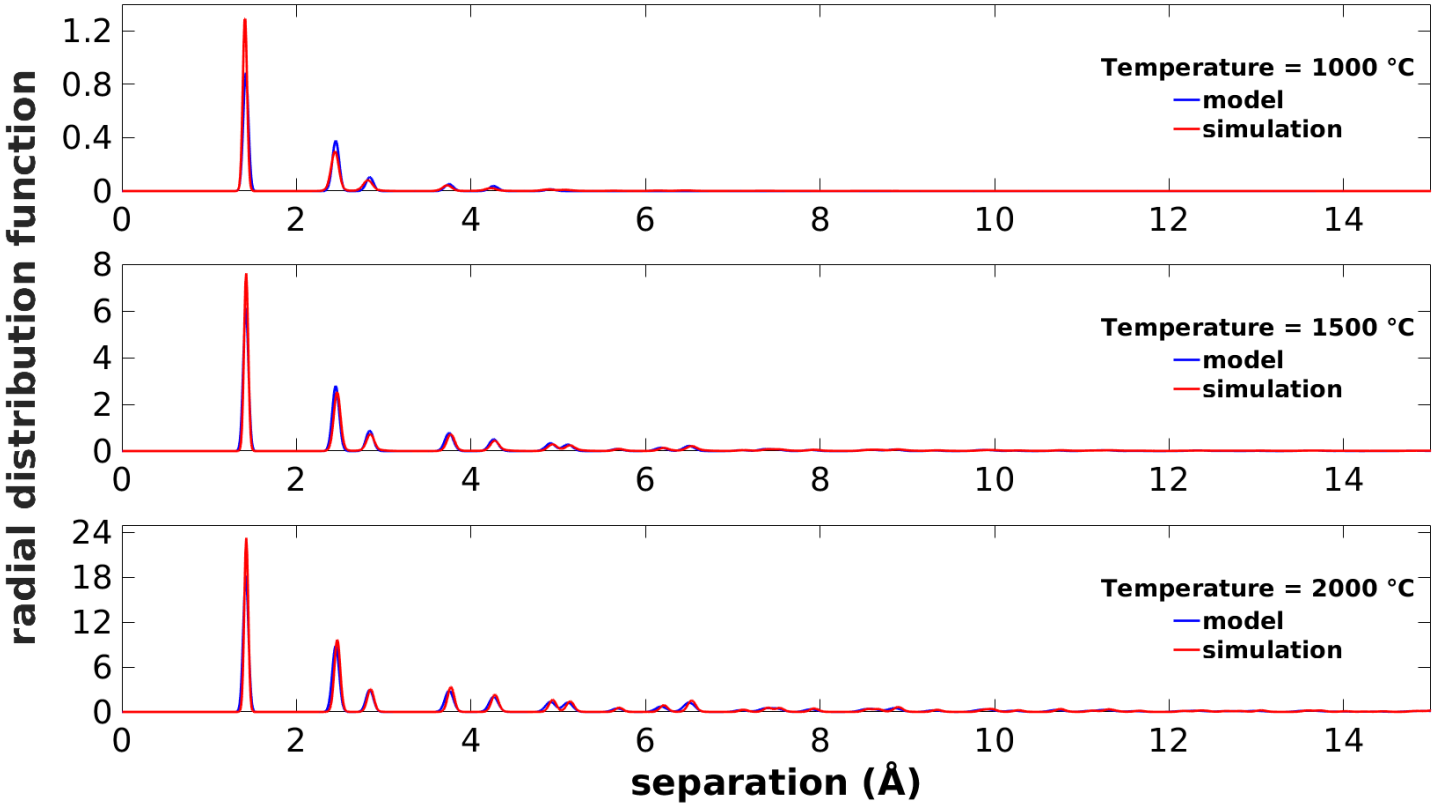


Figure 2-2. Comparison of the model and simulation RDF for the amorphous-amorphous intraplanar (*AA intraP*) in the three different composites. Note that the reported temperature corresponds to processing conditions. All RDFs were measured at room temperature.

If the amorphous carbon possessed sp^3 bond hybridization, the peak positions would be different. The relative magnitude of the peaks is also captured well. One notes that the size of the amorphous plane increases with increasing processing temperature. One can also note that the shape of the fragments is circular at the low and high temperatures. A circular fragment was the initial assumption for all models. Only at the intermediate temperature was it necessary to adjust the minor and major axes independently in order to capture the relative peak heights of the peaks at small and large separation. At high crystalline volume fractions, the amorphous fragments are small and can be modeled as small circles. At low crystalline volume fractions, the fragments of graphene in the amorphous domain are much larger, but their aspect ratio remains close to unity. Only at intermediate values of ϕ_C, where the fragments remain large but the shape of the amorphous domain is significantly impacted by the presence of the crystalline domain, is it necessary to introduce non-circular particles to accurately reproduce the component RDF.

2.2.4 Crystalline-crystalline, Intracrystallite, Intraplanar (CC, intraC,intraP)

The intraplanar component has the same form in the amorphous and crystalline phases. The only difference is that if a particular shape of nanoparticle is assumed, then there is a distribution of planes in the nanocrystallite. For example, in this work, we assumed spherical nanocrystallites, a choice that results in larger sheets of graphene (with the radius of the nanoparticle) near the center of the nanocrystallite and increasingly smaller sheets located further from the midplane. Thus a direct pairwise summation is performed over a distribution of plane sizes.

The parameters, which determine the number of planes, are the radius of the crystallite, r_c, (determined experimentally in this work and reported in Table 2-1) and the distance between planes, d_p. As shown in Figure 2-3, the agreement between model and simulation for the crystalline-crystalline, intracrystallite, intraplanar component is excellent. They are evaluated using equation 2.8. The magnitude of the peaks decreases as the processing temperature increases because the volume fraction of the crystalline domain decreases. The peaks extend to greater separations as the processing temperature increases because the size of the crystallites increases. As reported in Table 2-1, the optimal value of the distance between planes is smaller for the composite processed at the lower temperature, an observation which is attributed to the higher density of the material, which packed the nanoparticles in tighter and limited the breathing modes of motion observed for isolated nanocrystallites [103].

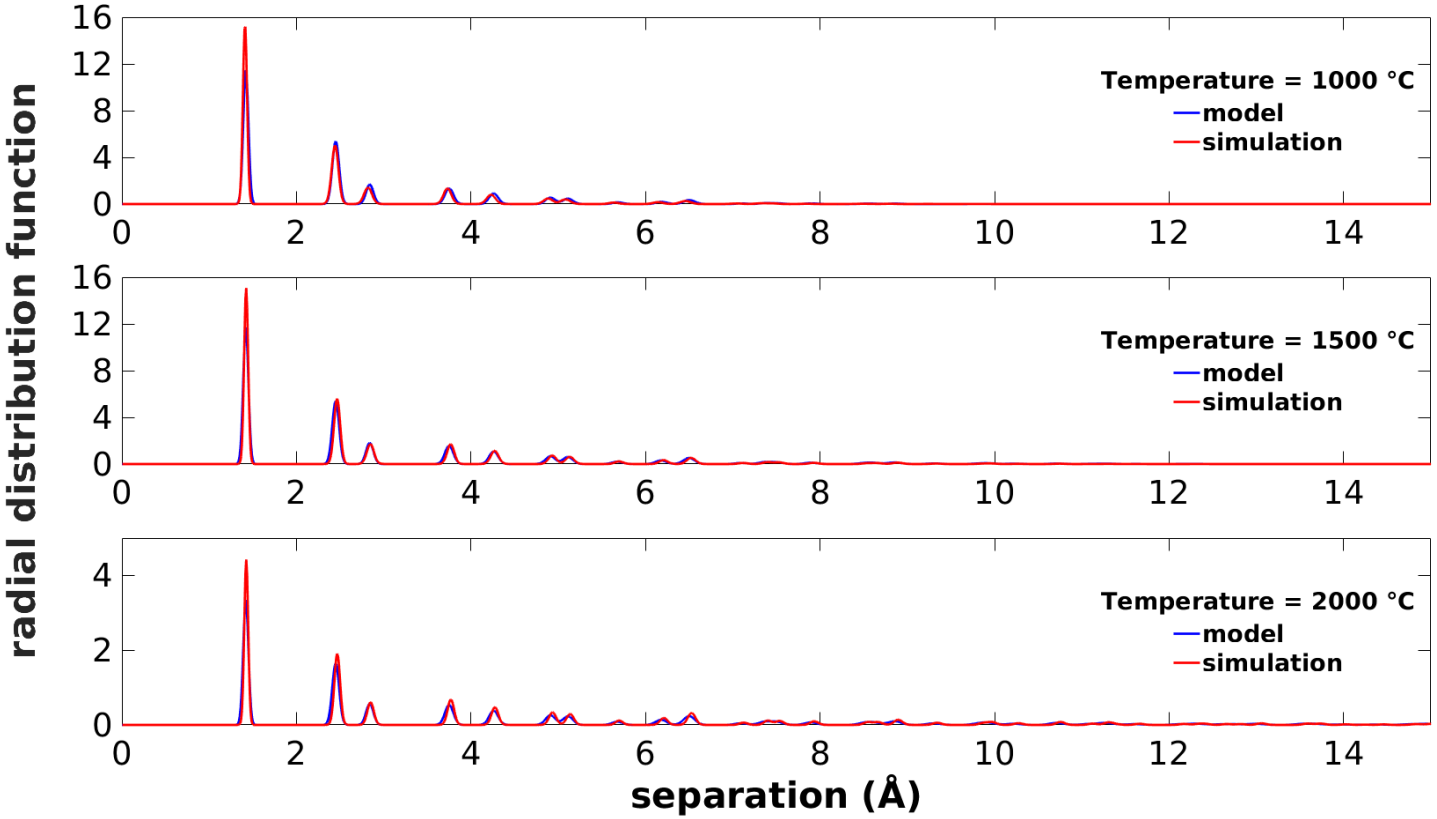


Figure 2-3. Comparison of the model and simulation RDF for the crystalline-crystalline intracrystallite intraplanar (*CC intraC intraP*) in the three different composites. Note that the reported temperature corresponds to processing conditions. All RDFs were measured at room temperature.

2.2.5 Description of Components at the Mesoscale

Some components to the RDF need not be represented at the atomic scale. Components that represent structures in which significant disorder exists will present a broad feature rather than the sharp peaks of Figures 2-2 and 2-3. These broad features can be captured well with a mesoscale model in which the atomic resolution has been discarded in favor of a continuous distribution of atom density. The essence of this approach requires the definition of two-dimensional and three-dimensional structural objects. A mesoscale distribution function, $g^*_{meso}(r)$, between objects is defined. The functional form of the contribution to the RDF due to a single pair of objects, $g^*_{meso,1-pair}(r)$, is determined as a function of their separation. This function is convoluted with $g^*_{meso}(r)$ in order to generate the full contribution to the component RDF A general, four-step procedure is employed to generate the mesoscale, single-pair RDF, $g^*_{meso,1-pair}(r)$. In the first step, a joint probability distribution is formulated in terms of the independent coordinates over which the RDF is to be averaged. These coordinates correspond to the 2D or 3D mesoscale objects. Since the coordinates are independent, the joint probability distribution is the product of the single variable probability distributions. In the second step, the argument r of $g^*_{meso,1-pair}(r)$ is defined as a function of the independent coordinates in the system. In the third step, integration over all the independent variables is performed, which generates a cumulative distribution function in the single variable of interest, r. In the fourth and final step, the cumulative distribution is differentiated with respect to r in order to obtain the probability distribution function, which is directly related to the component RDF, $g(r)$. Once $g^*_{meso,1-pair}(r)$ is known, it is convoluted with $g^*_{meso}(r)$ to obtain the component RDF. The two components, $g^*_{CC,intraC,interP}(r)$ and $g^*_{CC,interC}(r)$, which are treated with mesoscale detail, are described below.

2.2.5.1 Crystalline-crystalline, Intracrystallite, Interplanar (CC, intraC, interP)

The interaction between atoms arranged in adjacent planes of a single crystallite can be modeled by the interaction of a pair of two-dimensional discs, in which the atomic density is distributed uniformly over each disc. For circular discs, the interaction between one pair of discs, $g^*_{meso,1-pair}(r)$, can be analytically evaluated following the four step procedure described above. The planes defining these two discs are assumed to be parallel. The discs have centers located on a common normal vector. The inputs to this process are the radius of plane 1, $r_{p,1}$, the radius of plane 2,$r_{p,2}$, and the separation between center points, d_p.

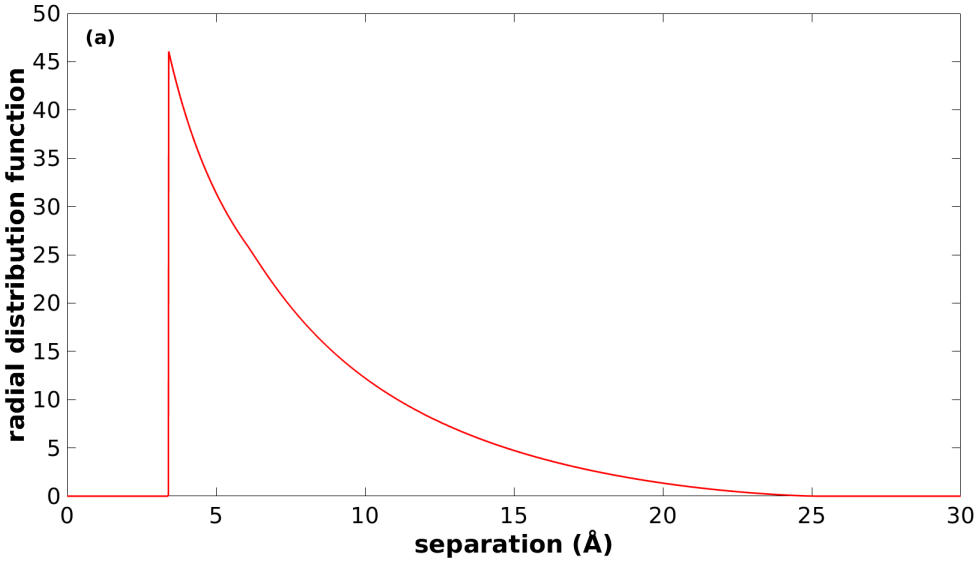
The derivation of the analytical formula describing the resulting contribution to the RDF from one pair of discs is provided in Appendix A. A characteristic plot for $g^*_{meso,1-pair}(r)$

is shown in Figure 2-4a. The mesoscopic distribution, $g^*_{meso}(r)$, of discs corresponds to a spherical crystallite. A graphitic nanocrystallite is modeled as a series of such discs, oriented parallel to each other and spaced at intervals of d_p. The individual radius of each disc corresponds to their position within the sphere, refer to Figure 2-4b [103]. The number of discs in a crystallite in this study is small, ranging from 3 to 9. The values are reported in Table 2-1. Thus, the contribution from all combinations of pairs can be explicitly summed with minimal computational expense. The crystalline-crystalline intracrystallite interplanar component of the RDF is plotted in Figure 2-5, where the bottom curve represents a crystallite with nine discs and corresponds to Figure 2-4b. The composites processed at 1000 and 1500 °C contain three discs (not shown). As shown in Figure 2-5, the *CCintraCinterP* component displays peaks corresponding to the separation between planes and is located at integer intervals of d_p. The peaks are broadened by the same Gaussian distribution used in the previous components to account for the thermal noise. From Figure 2-5, it is evident that the model agrees very well with the simulation.

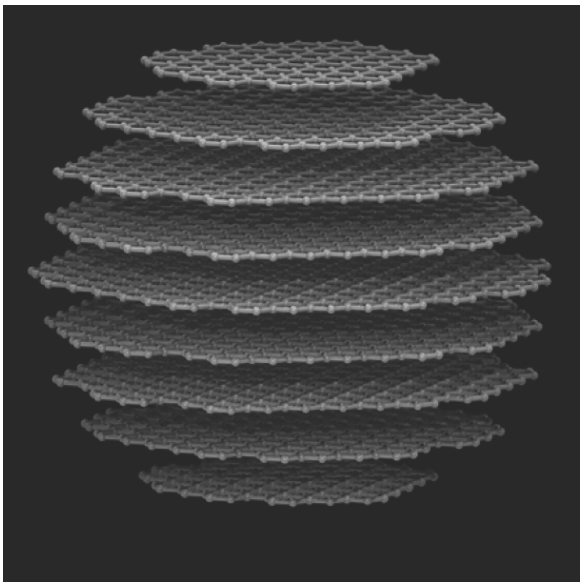
2.2.5.2 Crystalline-crystalline, Intercrystallite (CC, interC)

The interaction between atoms arranged in distinct crystallites can be modeled by the interaction of two three-dimensional spheres, in which the atomic density is distributed uniformly over each sphere. For spherical particles, the interaction between one pair of spheres, $g^*_{meso,1-pair}(r)$, can be analytically evaluated following the four step procedure described above. The inputs to this process are the radius of crystallite 1, $r_{c,1}$, the radius of crystallite 2, $r_{c,2}$, and the separation between center points, d_c. The derivation of the analytical formula describing the resulting contribution to the RDF from one pair of spheres is provided in the Appendix A. A characteristic plot for $g^*_{meso,1-pair}(r)$ is shown in Figure 2-4a.

It has been shown that shape of a nanoparticle influences the resulting RDF [115]. In this work, we limit ourselves to spherical particles. In future work, we intend to remove this restriction though we will be forced to replace the analytical result with numerical integration for non-spherical particles. The mesoscopic distribution, $g^*_{meso}(r)$, of spheres must be chosen to correspond to a given model. In this model, we assume a distribution of crystallites with three features. At short separations, there is a region of excluded volume preventing overlap of spheres. At the nearest possible distance, there is a delta function corresponding to close-packing. Beyond that there is a uniform distribution chosen to correspond to the bulk density of crystallites. A schematic of this mesoscale distribution of crystallites is shown in Figure 2-6(b).



(a) RDF of single pair of planes



(b) Graphene crystallite

Figure 2-4. (a) A typical example of an RDF due to a single pair of planes, with $r_{p,1} = 10.0$ Å, $r_{p,2} = 15.0$ Å and $d_p = 3.4$ Å. (b) Schematic of single crystallite displaying model mesoscale distribution of discs.

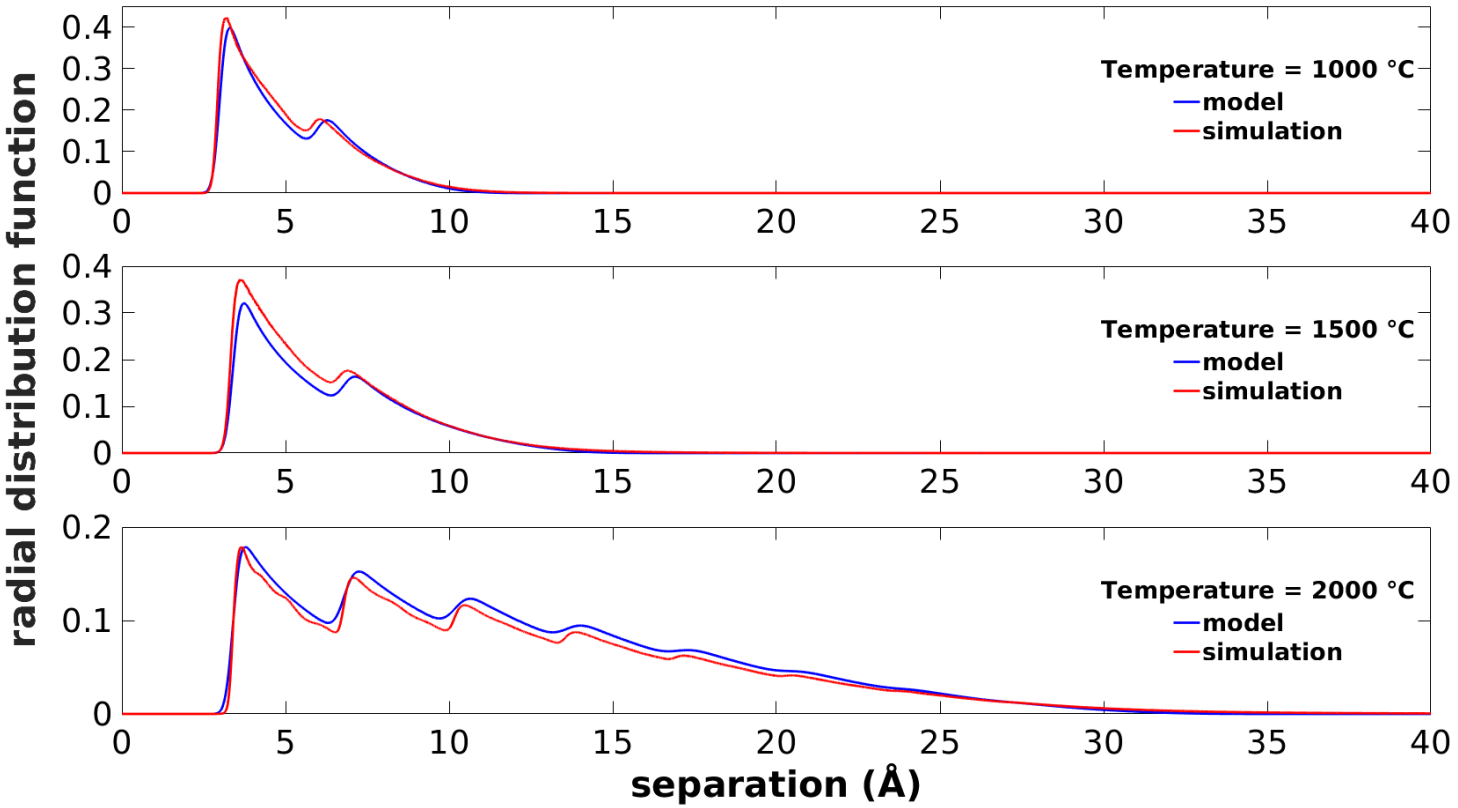


Figure 2-5. Comparison of the model and simulation RDF for the crystalline-crystalline intracrystallite interplanar (*CC intraC interP*) in the three different composites. Note that the reported temperature corresponds to processing conditions. All RDFs were measured at room temperature. The composite processed at 2000 °C corresponds to the schematic of Figure 2-4b.

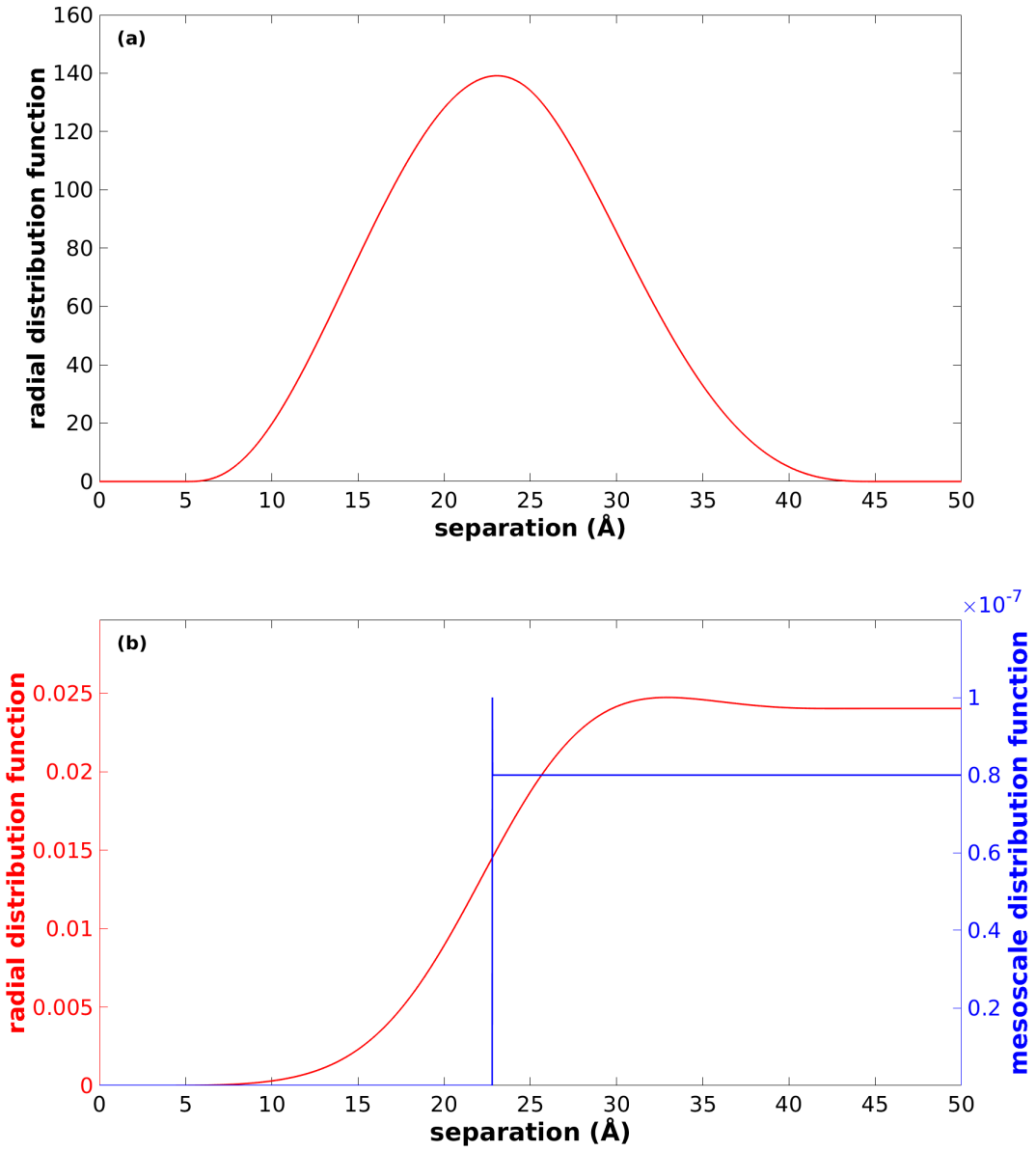


Figure 2-6. (a) A typical example of an RDF due to a single pair of spheres, with $r_{c,1} = 10.0$ Å, $r_{c,2} = 10.0$ Å, and $d_c = 25.0$ Å. (b) A typical mesoscale distribution of spheres and the convolution of the single pair RDF in (a) with the mesoscale distribution.

The close-packing peak was required only for the largest crystallite with a low crystallite volume fraction, as reported in Table 2-1. In contrast to the mesoscopic distribution of planes within a crystallite, which was discrete, the mesoscopic distribution of crystallite is continuous. Therefore, a simple explicit evaluation of the convolution of $g^*_{meso,1-pair}(r)$ (Figure 2-6(a)) and $g^*_{meso}(r)$ (Figure 2-6(b)) is not possible. In this case, we numerically convoluted the functions. Although this is not essential, in some but not all cases, the curve can be fit well by a complementary error function, see Figure 2-6(a). In a previous work, we note there is substantial disorder within the nanocrystallite due to "sliding", "rocking" and "breathing" modes of graphene planes with respect to each other [103]. There is also an additional element of disorder in the random orientation of the crystallites. The former elements of disorder effectively smear out atomic detail. Averaging the RDF over all pairs of crystallites presents a smooth component.

We determined that this mesoscopic distribution of the model only describes the system well at low crystallite volume fraction. At high crystallite volume fraction, there is an initial step-like feature located at a separation corresponding to the diameter of a carbon atom. This feature in the contribution is due to the deformation of crystallites that pack tightly against each other. This abrupt atomic scale feature is distinguished from the much more gradual contribution due to the mesoscopic spacing of the crystallites. Ultimately, we chose to capture this behavior with two erfc functions, the first representing atomic packing and the second representing the mesoscale distribution. The height of the step in the component RDF due to the atomic packing as a fraction of the asymptotic value is reported in Table 2-1. The crystalline-crystalline intracrystallite interplanar component of the RDF is plotted in Figure 2-7. As can be seen this model agrees well with simulation for all three composites.

2.2.6 Contributions Described with Perturbations to a Mean Field

The two remaining components in the RDF decomposition include the amorphous-amorphous interplanar component (*AA, interP*) and amorphous-crystalline component (*AC*). In these cases, we cannot resort to atomistic detail as was done in the first two components, nor is the geometry of the interacting domains sufficiently clear to allow for a reasonable mesoscale approximation as was done in the second two components. In these cases, we build a model featuring four assumptions: (i) excluded volume up to the size of the atoms (AEV), (ii) mean-field (MF) approach, in which we assume that the atoms contributing to this component are the result of a uniform distribution of atoms distributed over the volume, (iii) a perturbation to the mean-field based on excluded volume due to the mesoscale crystalline phase (MEV), and (iv) the presence of partially crystalline elements

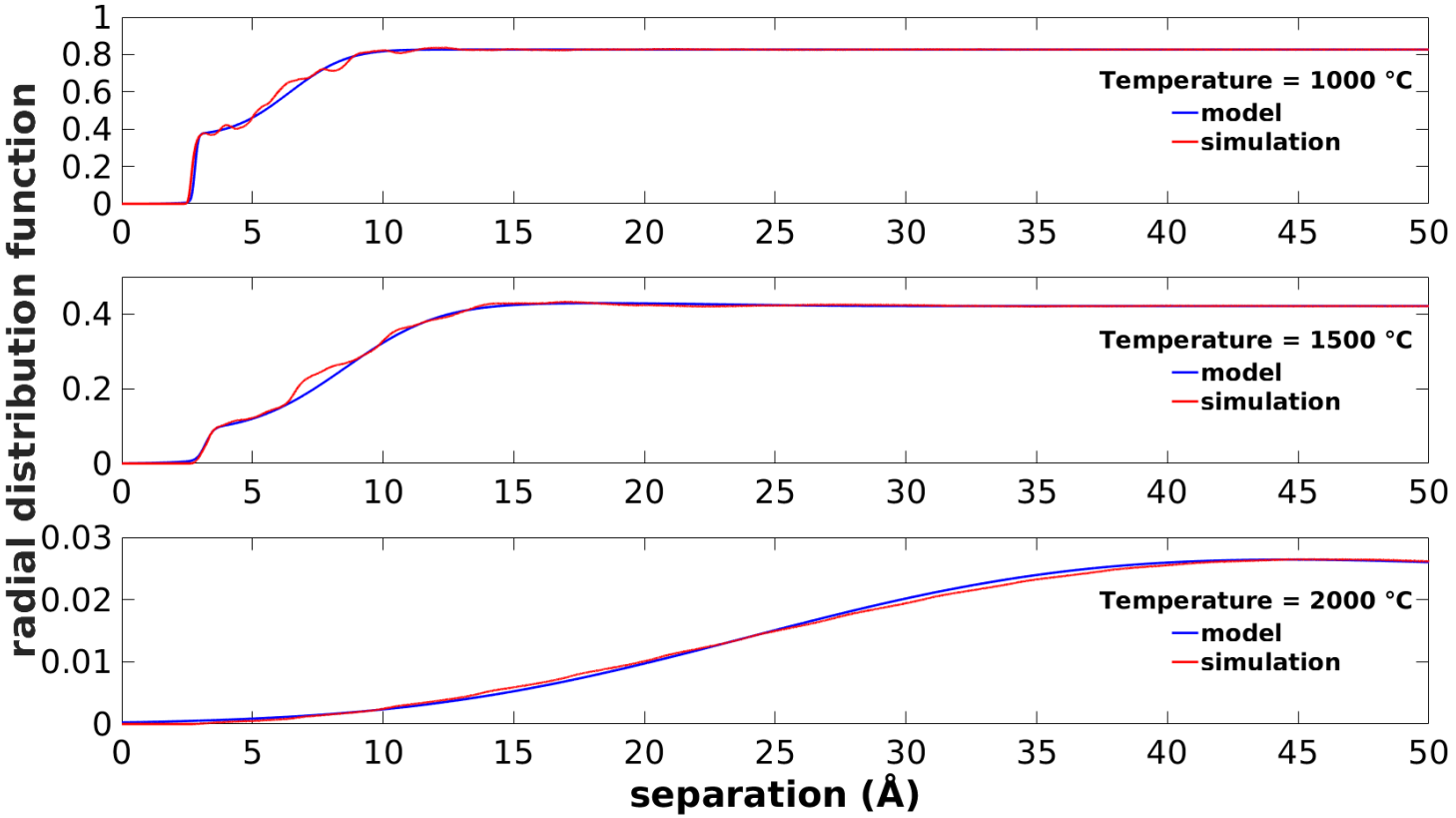


Figure 2-7. Comparison of the model and simulation RDF for the crystalline-crystalline inter-crystallite (*CC interC*) in the three different composites. Note that the reported temperature corresponds to processing conditions. All RDFs were measured at room temperature.

within the amorphous domain. To this we add the same thermal noise applied to other intermolecular components. In Figure 2-8(a), the effects of the atomic excluded volume and mesoscale excluded volume are graphically illustrated. The presence of partially crystalline elements can be readily accommodated since we have already described the crystalline-crystalline, interplanar components as shown in Figure 2-5. Thus a signature that corresponds to a diffuse interface in which both amorphous and crystalline elements are present can be obtained by combining these two components. In Figure 2-8(b), a linear weighting function is used to combine the *AA, interP* with MF+AEV+MEV effects, as shown in Figure 2-8(a), with a *C-C,interP* signature, from Figure 2-5, to generate an RDF component for a phase that shows both amorphous and crystalline elements in a diffuse interface that spans, in this example, 20 Å.

2.2.6.1 Amorphous-amorphous, Interplanar (AA, interP)

The interaction between pairs of atoms, in which both atoms are located in the amorphous domain but in distinct planes, comprises the amorphous-amorphous, interplanar component. For all three composites, the partially crystalline nature of the phase is described by a linear weighting between an amorphous signature and a crystalline subcomponent. The crystalline subcomponent is taken directly from the crystalline-crystalline, intracrystallite, interplanar contribution as shown in Figure 2-5(a). The amorphous subcomponent is modeled, as described above, with a mean field including perturbations from AEV and/or MEV effects. The distinct contribution due to the crystalline subcomponent is short-ranged; at longer distanced it is indistinguishable from the amorphous contribution. The parameters of the weighting function are described in Table 2-1. These parameters include the maximum fraction of crystallinity (the y-intercept of the weighting function) in Figure 2-8(b) and the interface width (the x-intercept of the weighting function) in Figure 2-8(b). The resulting comparison of the model and simulation is shown in Figure 2-9. As can be seen, the agreement between the model and simulation is quite good. The top plot in Figure 2-9 looks poor but the y-axis is on the order of 10^{-3}, so this error is on the order of noise in the experimental signal. This simple approach demonstrates the capability of describing a partially crystalline phase. The choice of a linear weighting function was made strictly with the intent of minimizing the number of parameters. A more sophisticated weighting function could certainly be used, though it was not justified for these materials.

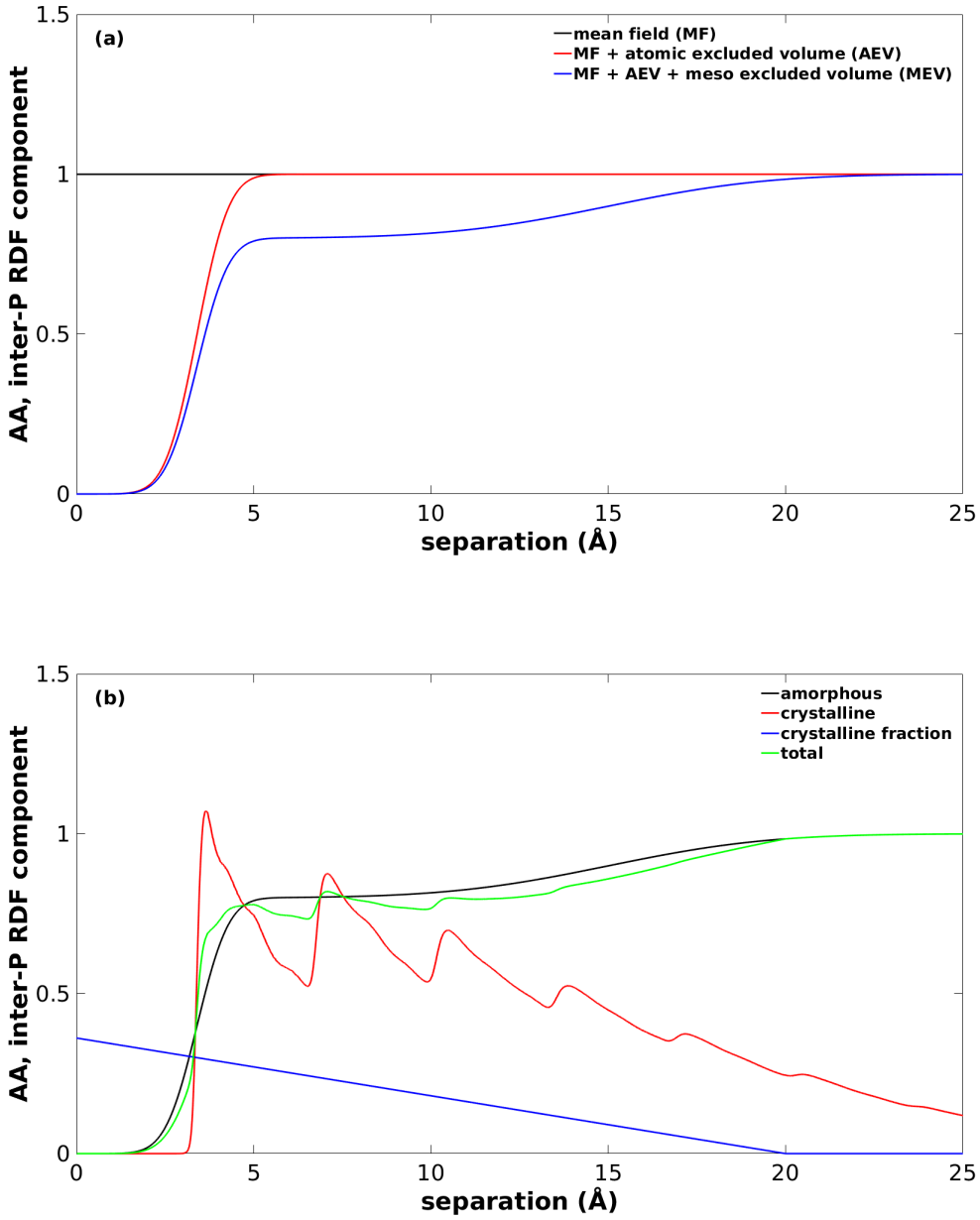


Figure 2-8. Schematic of amorphous-amorphous, interplanar modeling approach. (a) The impact of atomic excluded volume (AEV) and mesoscale excluded volume (MEV) on the mean field approximation. (b) A typical diffuse interface modeled as a linear weighting of the amorphous contribution from Figure 2-8(a) and the crystalline contribution from Figure 2-5 (2000 °C).

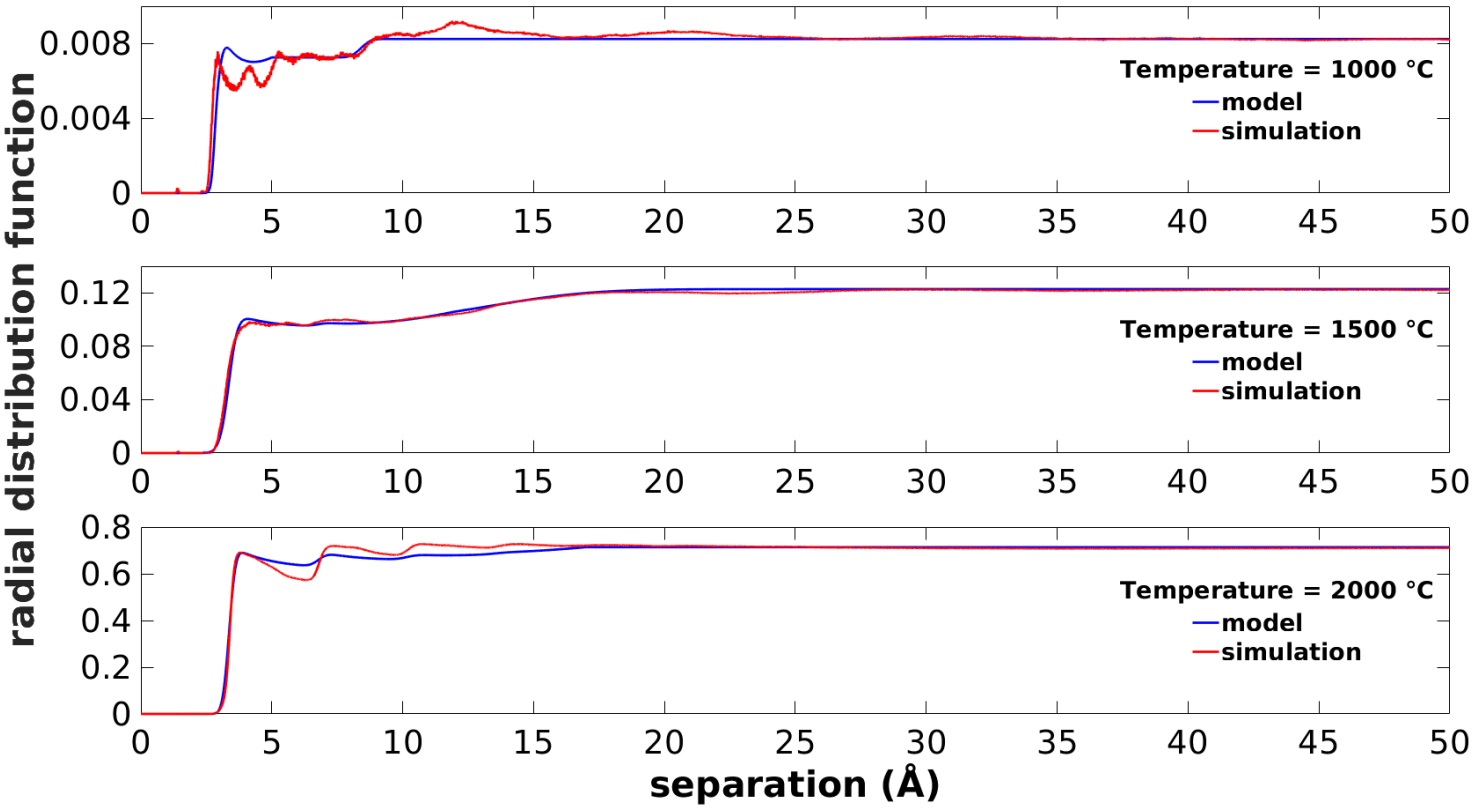


Figure 2-9. Comparison of the model and simulation RDF for the amorphous-amorphous interplanar (*AA, interP*) in the three different composites. Note that the reported temperature corresponds to processing conditions. All RDFs were measured at room temperature.

2.2.6.2 Amorphous-crystalline (AC)

The interaction between pairs of atoms, in which one atom is in the amorphous domain and the other in the crystalline domain is captured in the *AC* contribution to the RDF. This contribution in general involves integration over a complex geometry.

Therefore, a mean field approach with perturbations was again invoked. In an approach identical to that taken for the *AA, interP* contribution, the diffuse interface is described by a linear weighting between an amorphous signature and a crystalline subcomponent. As before, the crystalline subcomponent is taken directly from the crystalline-crystalline, intracrystallite, interplanar contribution as shown in Figure 2-5. The amorphous subcomponent is again modeled with a mean field including perturbations from AEV and/or MEV effects. The resulting comparison of the model and simulation is shown in Figure 2-10. As can be seen, the agreement between the model and simulation is quite good. This simple approach demonstrates the capability of describing a diffuse interface between a crystalline and amorphous domain. Of course, the limitation of this approach is obvious; if the interface demonstrates a different crystal structure than the "bulk", then this approach will obvious not capture the interfacial structure. For materials where this limitation is not present, this model should suffice. Again, the choice of a linear weighting function was made strictly with the intent of minimizing the number of parameters. The agreement in Figure 2-10 can be improved by using a nonlinear profile to describe the crystalline component of a diffuse interface. However, we chose not to do this because ultimately we hope that this tool will be used to interpret experimental data. In the experiment, only the total RDF and not the components of the RDF are available. As we shall see below, where the total RDF is shown, the shortcomings of Figures 2-9 and 2-10 are not apparent. So, while it is possible to correct them where a decomposition is available, the need to include nonlinear profiles of the diffuse interface is not immediately clear, at least for these materials.

2.2.7 Total RDF

Sumation of the six individual component RDFs results into the total RDF of the system. For the three cases being examined, Figure 2-11 shows the comparison of the total RDF for the model, simulation, and experiment. The parameters used in the model are those obtained from fitting the model to the simulation data. As noted in Table 2-1, some parameters were not fit at all, but were simply transferred from the simulation. Thus, the model and simulation are almost indistinguishable. The ability of the simulation (and equivalently model) to describe the data is excellent.

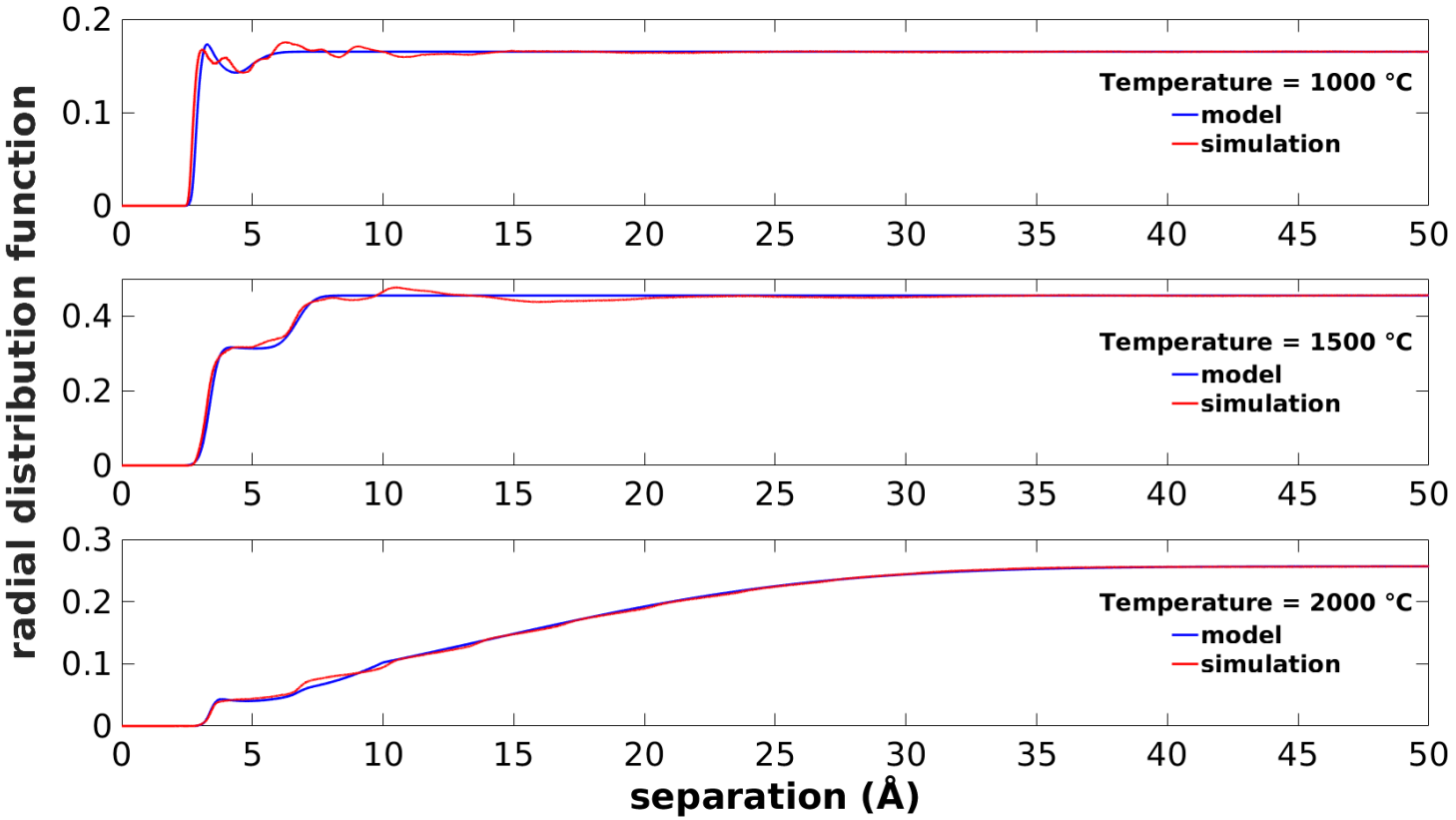


Figure 2-10. Comparison of the model and simulation RDF for the amorphous-crystalline (*AC*) in the three different composites. Note that the reported temperature corresponds to processing conditions. All RDFs were measured at room temperature.

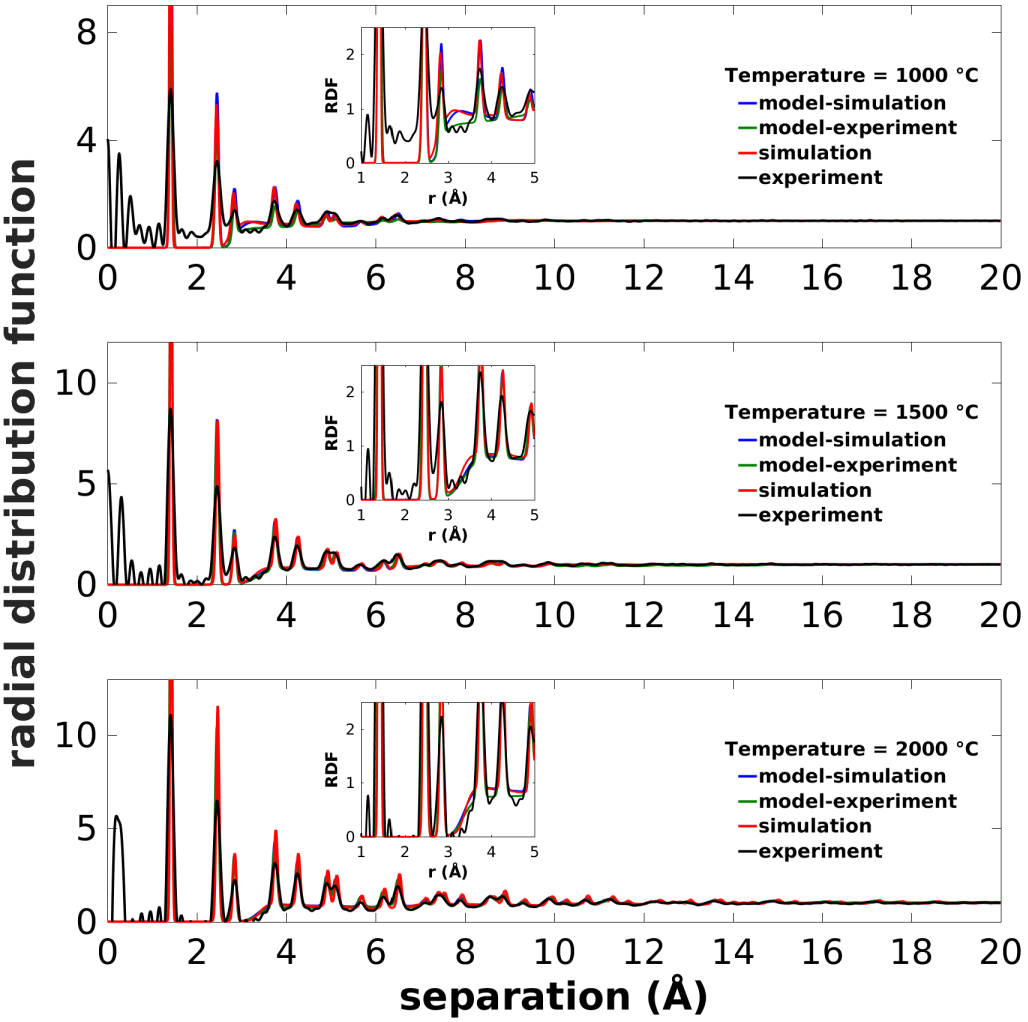


Figure 2-11. Comparison of the total RDF from the model to results from MD simulation and NS experiments in the three different composites. Note that the reported temperature corresponds to processing conditions. All RDFs were measured at room temperature. Two model RDFs are shown. The first model, denoted "model-simulation" is parameterized to simulation and is the sum of components shown in Figures 2-2, 2-3, 2-5, 2-7, 2-9 and 2-10. The second model, denoted "model-experiment", otherwise functionally identical, is further optimized to the experimental data.

All peaks are accounted for because all peaks originated with an intraplanar contribution either in the crystalline or amorphous phase. The relative magnitude of a peak based on processing temperature as observed in the experimental system is also reproduced in both simulation and experiment. However, the agreement between simulation and experiment is not flawless. There are discrepancies, particularly in the important range between 3.0 and 4.0 Å, where the interplanar spacing is located. Refer to the inset in Figure 2-11. Regardless of whether one uses simulation or a model to interpret the scattering data, it is an iterative process.

In the work invoking simulations, the interpretation was ended after a single iteration, largely because of the HPC resources required to perform a second iteration. The reduction in the computational requirement from the simulation to the model is significant, approximately in at least six orders of magnitude [117]. Since the model is computationally tractable, no such limit on the number of iterations exists. Therefore, we further optimize the model, beginning with the current parameter set, to the experimental data. This fit is shown in Figure 2-11. The largest discrepancy between the simulation and the experiment lies in the region between 3.0 and 4.0 Å for the 1000 °C composite. For the type of material, the improvement in the agreement between the model and experiment was achieved through a reduction in the volume fraction of the crystalline domain. We note that the hierarchically decomposition of the RDF provides a tractable, physically-meaningful and tractable approach to the interpretation of scattering data of complex materials, especially for the routine users without access to HPC resources. These approach provide reasonable guesses of parameter values, such as volume fraction of the crystalline domain, crystallite radius and diffuse interface width, that can be used in the construction of atomistic models, thus reducing the total number of simulation iterations required. In this demonstration of the model, some parameters were taken from the simulation, in order to emphasize that this is not purely an optimization process, in which the parameters have no physical meaning. By holding certain parameters constant at the values used in the simulation, we are removing variables from the optimization that could improve the fit. Our good comparison is consequence of this "physics based" model and not an exercise in curve fitting. Of course, in the absence of simulation data, good initial guesses for all parameters will be optimized.

2.2.8 Conclusion

Neutron scattering signature of a series of carbon composites was successfully interpreted via the hierarchical decomposition of the RDF using a computationally

tractable model. The model achieves a reduction in computational effort of up to six orders of magnitude relative to molecular dynamics simulation, making this approach available as a routine tool for interpretation of the scattering patterns of complex materials. The model's efficiency, relative to simulation, allows performing additional structural refinement to improve the agreement of the model result with the experimental data. Use of the model provides both quantitative and qualitative insight into the structure of the composite, providing parameters that correspond to the volume fraction of crystalline and amorphous phases and crystallite sizes. Experimental information from small angle scattering techniques, Guinier analysis, and temperature effects on particle size might be used in future developments to refine the model considering material dispersity. Furthermore, the model provides parameters not directly generated from the simulation including the interface width for diffuse interfaces. The model can be generally extended to other composite materials making it suitable for MD simulation that requires high performance computation.

CHAPTER 3

ELUCIDATING NANO- AND MESO- STRUCTURE IN LIGNIN-BASED CARBON COMPOSITES: A COMPREHENSIVE STUDY OF FEEDSTOCK AND TEMPERATURE

Chapter 3 includes an unpublished draft version of the of latest published article. The chapter includes introduction, experimental procedure, results and discussion, and conclusion. The latest version can be found in *Carbon* cited as:

"García Negrón, V., Kizzire, D. G., Rios, O., Keffer, D. J., & Harper, D. P. (2020). *Elucidating nano and meso-structures of lignin carbon composites: A comprehensive study of feedstock and temperature dependence*. Carbon, 161, 856–869."

Acknowledgements: The authors would like to acknowledge Dr. K. Chapman who assisted with data collection at APS beamline 11-ID-B at Argonne National Laboratory through research proposal 2017-GUP54614. Use of the Advancement Photon Source, an Office of Science User Facility operated by the U.S. Department of Energy (DOE) Office of Science by Argonne National Laboratory, was supported by the U.S. DOE under Contract No. DE-AC02-06CH11357. Experimental design on KSW to specific carbonization test was performed by students from MSE department at UT-Knoxville: J. Sutton, D. San Roman, A. Thomas, D. Kitsmiller, A. Affolter, and Dr. C. Wetteland. Thanks to Ms. L. Yu, CRC UT-Knoxville, for reproducing KSW material. Thanks to Dr. N. M. Cantillo and Dr. G. A. Goenaga, CBE department UT- Knoxville, for BET experiments. Lastly, special thanks to Dr. J. Dunlap and Dr. G. Duscher from the Joint Institute for Advanced Materials facilities for the operation and support of TEM. This research was supported by a grant from the U.S. Department of Agriculture National Institute of Food and Agriculture Nanotechnology Program award number 2017-67021-26599. D. P. Harper acknowledges support from the USDA National Institute of Food and Agriculture, Hatch Project 1012359.

Abstract: The production of carbon materials from renewable biofeedstocks is rapidly expanding with commercial applications in the areas of advanced materials, energy storage, and biochemicals. Present-day challenges exist in understanding how the distribution of monomeric units in lignin feedstocks impacts the structure and properties of carbon composites as a function of processing. This research investigates the effect of lignin feedstock and processing conditions on the structure of carbon composites. X-ray data was collected at a synchrotron source for lignin from hardwood, softwood, and grass feedstocks, processed under varying temperature and environmental conditions. The relative abundance of the principal monomeric units—guaiacyl, *p*-hydroxyphenyl, and syringyl—varies with feedstock and result in reproducible variations in the x-ray data. Statistical analyses for over fifty carbon materials were performed to determine the influence of feedstock, reduction temperature, and furnace humidity. The changes in the pair distribution function correspond to changes in material structure. Taken together, the analyses support the observation that graphitic structures form and grow in size with increasing reduction temperature. The characteristic size of the graphitic crystallites varies with feedstock, with kraft softwood and organosolv switchgrass leading to carbon composites with larger graphitic domains.

3.1 Introduction

Understanding state-of-the-art processing methods of biorenewable sources has become a major focus for obtaining low-cost bioproducts suitable for high-end applications. Moreover, the production of carbon materials from renewable biofeedstocks is rapidly expanding with commercial applications in the areas of advanced materials, energy storage, and biochemicals. One such example in the wood industry is manufacturing carbon-based products from lignin feedstocks due to its rich carbon content. Demystifying lignin structure has proven to be a challenge, particularly due to its seemingly random and complex network arrangement of organic groups and its variants across wood species [16, 24, 26, 69, 70, 166]. The principal monomeric units present in lignin species are coniferyl, sinapyl, and *p*-coumaryl alcohols. These are phenolic precursors to *p*-hydroxyphenyl (H), guaiacyl (G), and syringyl (S) [53, 69]. The variety of monomeric units drives the selection and processing of the raw material source toward specific. Previous studies have measured chemical composition, purity, and ratios of the monomeric units found in lignin [16, 23, 69, 70, 97, 154, 166]. Valorizing lignin remains one of the top challenges towards commercial production of many plant derived fuels and chemicals [2]. Valorization controls include native biocrop manipulation, biosynthesis, and chemical modification [22, 35, 143]. In addition, understanding the physicochemical

impact of isolating lignin from the cell wall is important as it impacts the purity, yield, and ability to convert the raw source to new products.

In this work, lignin feedstocks were extracted from hardwoods, softwoods, and grasses. These organic materials were thermochemically decomposed and reduced at high temperatures resulting in nanostructured composites, composed of graphitic crystallites and amorphous carbon domains. Previous work examined graphite structure at high temperature where crystallographic changes are present and surface chemistry is improved as result of heat treatments [51]. The conversion of renewable feedstocks to lignin-based carbons is used to establish relationships between structural features as a function of feedstock source, extraction method, and carbonization stages. The carbon product contains both disordered amorphous and ordered crystalline carbon domains. A goal of this work is to produce low-cost graphitic materials which, as an example, have been investigated for energy storage applications [53, 175]. Characterization of the interaction of lignin carbons in electrode systems can provide support to engineered carbon products used in electrochemical applications.

In this chapter, we investigate the pair distribution function (PDF), which correlates atomic positions by measuring the probability of an atom being located at specific distance from other atoms. A PDF serves as a standard characteristic of the atomic structure of a material [11]. The PDF, $G(r)$, was analyzed for processed carbonized material to help describe the local atomic structure in lignin carbon at the nano- and mesoscales [112, 118, 132–134, 136].

$$G(r) = 4\pi r[\rho(r) - \rho_0] \tag{3.1}$$

$G(r)$ depends on the local (ρ) and average ρ_0 atomic densities, and the radial distance (r) [11]. In a carbon-rich material, the radial distance primarily corresponds to carbon-carbon pairs. An approach for computing $G(r)$ consists of using the normalized and corrected total structure function, $S(Q)$, obtained from x-ray powder diffraction data. Once the experimental x-ray data is collected and processed to obtain scattering vectors (Q), corrections are methodically performed for background, Compton, and multiple scattering as well as geometric effects and absorption [43]. The normalized total structure factor is calculated as

$$S(Q) = 1 + \left[\frac{I^{coherent}Q - \sum c_i |f_i Q|^2}{|\sum c_i f_i Q^2|}\right] \tag{3.2}$$

The coherent scattering intensity per atom is $I^{coherent}$ in electron units, and for atom type i, the atomic concentration is c_i and the scattering form factor is f_i [28]. The PDF is obtained

from the total structure factor via Fourier transform,

$$G(r) = \frac{2}{\pi} \int_0^\infty Q\,[S(Q) - 1]\, sin(Qr) dQ \tag{3.3}$$

In crystalline materials, PDFs tend to exhibit defined and narrow peak intensities whereas amorphous materials have characteristically broader peaks. Commercial software packages, such as PDFgetX3, GSAS-II, xPDFsuite, and Fit2D, are commonly used to process x-ray scattering and obtain $G(r)$. A non-iterative partial least square principal component analysis (PCA) was applied to the PDFs of carbon composites. PCA can be interpreted as an orthogonal linear transformation where the coordinates of the new projection correspond to a score based on the variance of the data, ordered from largest to lowest, thus it is a common approach for dimensionality reduction of large data sets [57, 86]. A complementary statistical analysis used to relate the effects of temperature in lignin carbon structure is the correlation coefficient which identifies linear relationships between two variables, X and Y. The correlation coefficient is defined as

$$\rho_{XY} = \frac{\sigma_{XY}}{\sqrt{\sigma_X^2}\sqrt{\sigma_Y^2}} \tag{3.4}$$

and provides a measure of the covariance of two variables. The coefficient is normalized by the standard deviations and is bounded by $[-1, 1]$. If $X = Y$, then $\rho_{XY} = 1$ and if $X = -Y$, then $\rho_{XY} = -1$. A high positive correlation coefficient means that, from a statistical point of view, as X increases, Y also increases, and viceversa. A high negative correlation coefficient means that changes in X have an opposite effect on Y. A recent study applied a multivariate statistical analysis using x-ray data collected from cellulose material to investigate the degree of crystallinity. Correlation calculations for various diffraction angles and pretreatments were compared to the original data set. Furthermore, statistical methods have helped identify the most efficient pretreatment method and understand crystallinity changes and degree of polymerization in materials [82]. In our work, correlations were used to investigate relationships between PDFs obtained from x-ray data and the controlled variables such as lignin feedstock, reduction temperature, and humidity. This systematic approach achieves a complete study of lignin carbon structure that enables tuning and tailoring for application-specific carbon products. Using high-resolution transmission electron microscopy (HR-TEM), atomic structure of the amorphous and crystal in the synthetic carbon product can be investigated. In a recent study, HR-TEM and diffraction patterns were collected when processing a fibrous lignin carbon mat at

1000 and 2000 °C [157]. The diffraction patterns exhibited components similar to graphite and disordered nanocrystal structures with larger crystals formed at 2000 °C compared to 1000 °C. In our experiments, HR-TEM and diffraction patterns were collected for lignin feedstocks reduced at 1050 and 2000 °C. The TEM work provides complementary and corroborative data to the PDF analyses.

In this work we present the relationship of carbon composite structures as a function of lignin feedstock, processing conditions, and heat treatments. In the remainder of the manuscript, , we present the techniques used for lignin extraction, carbonization, and materials characterization. Results include x-ray data, elemental analysis, and HR-TEM. In addition, statistical analyses from PDFs are used to distinguish structural features between lignin feedstocks.

3.2 Experimental Section

3.2.1 Processing

3.2.1.1 Feedstock Extraction

Lignin was extracted from Alamo switchgrass (*Panicum virgatum*), hardwood yellow poplar (*Liriodendron tulipifera*), and softwood pine (*Pinus taeda*). The lignin extraction methods consisted of kraft pulping and organosolv fractionation. Kraft softwood was obtained from lignin precipitated Indulin AT, from MeadWestvaco. Organosolv fractionation followed the recipe from Hosseinaei's and Bozell's methods [16, 69]. For the organosolv fractionation, a solvent mixture was conducted in-house consisting of 16:34:50 wt.% of methyl isobutyl ketone (MIBK), ethanol, water, and 0.05 M of sulfuric acid (H_2SO_4). The solvent mixture and wood chips were placed in a flow-through reactor to 160 °C and 145 psi. Once the reaction reached the set temperature and pressure, these conditions were held for 90 min. Sodium chloride (NaCl) was added to black liquor collected (50% v/v of black liquor times 0.15) in a separatory funnel to induce a phase separation organic and aqueous soluble fractions. Once the phase separation occurred, the organic material was collected. A water wash was performed by adding 30% v/v deionized water to the organic liquor. This removed any presence of residual sugars and ethanol that may be present after salt separation. Then, the lignin-rich organic material was isolated by rotary evaporation and diethyl ether washed until material was completely dried. To remove impurities of sugars and extractives, the sample was placed in a flask with magnetic stir bar at speed of 175 revolutions per minute (rpm) and water washed at room

temperature until a homogeneous mixing was achieved. The content of the organic lignin and water were filtered, and the solid content was collected and dried for approximately 12 h under vacuum at 80 °C.

3.2.1.2 Carbonization

The carbonization process followed the method used in [53]. Lignin was loaded in alumina crucibles and placed inside a tube furnace, then pyrolysis was performed in a nitrogen gas environment with 18 $g\,m^{-3}$ of water content at a flow rate of 3 $L\,min^{-1}$. The furnace was set to 1000 °C at 10 $°C\,min^{-1}$ and held for 1 h at 1000 °C. After pyrolysis, the carbon material is ball milled at 350 rpm for 3 h to reduce particle sizes. The reduction step was conducted at 1050 °C with a mixed gas of 96% argon-4% hydrogen environment where the content of oxygen is reduced. A second graphite furnace was used to reduce samples at 1500 and 2000 °C with a mixed gas of 95% argon-5% hydrogen environment. Samples were reduced at three different temperatures, though no sample was exposed to more than one reduction temperature.

3.2.2 Material Characterization

3.2.2.1 APS X-ray Data

The 11-ID-B station at the Advanced Photon Source (APS) facility at Argonne National Laboratory was used for data collection of x-ray powder diffraction and pair distribution functions. The capabilities of high-energy electrons from this synchrotron source enable results of high-quality and high-resolution data gathered in a short time (5 minutes per sample). Lignin powder samples were prepared in Kapton capillary tubes (Cole-Palmer)for triplicates of 51 samples of the material. The capillary tubes were placed in a sample holder provided at beamline. The tubing sizes are: 1.105 mm OD and 1.02 mm ID. The instrument was operated with an energy of 58.69 keV and wavelength (λ) of 0.2113 Å. The detector was placed 20 cm for PDF collection and 95 cm for powder diffraction collection. The shutter was left open to 0.5 seconds per frame. For PDF data, 600 frames were collected at 300 seconds per sample, and for powder diffraction data, 60 frames were collected at 30 seconds per sample. The radial distances of PDF data range from 0 to 50 Å, with a spatial resolution of 0.01 Å. Powder diffraction of each experimental condition was collected in triplicate to validate homogeneity of the carbon composites and attain reproducibility. Figure 3-1 overlays one set of triplicates to confirm that reproducible PDF patterns are generated for a given combination of feedstock and processing condition.

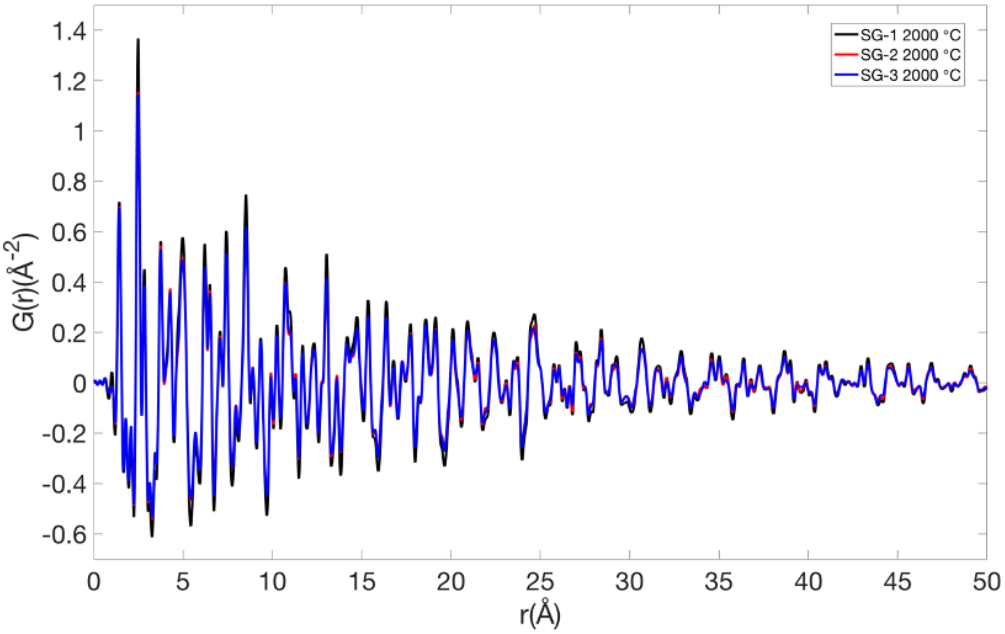


Figure 3-1. Pair distribution functions of three samples of switchgrass carbon composites reduced at 2000 °C.

The minor variations in intensity reflects the packing differences of carbon powder when capillary tubes were prepared. Reproducibility comparable to that shown in Figure 3-1 were generated for all samples.

3.2.2.2 Lignin NMR Spectroscopy

In general, lignin possesses three principle monomers, guaiacyl (G), *p*-hydroxyphenyl (H) and syringyl (S), formed from the precursor alcohols, coniferyl, *p*-coumaryl and sinapyl, respectively. In order to determine the presence of G, H, and S units in a given feedstock, 2D-NMR was performed. All 2D-NMR data acquisition was performed with a Varian 400-MR spectrometer at a 400 MHz operating frequency. First, samples were prepared by dissolving 60 mg of lignin in 0.6 mL deuterated-DMSO (99% dimethyl sulfoxide d6). Then, samples were examined at 25 °C using a (HC)bsgHSQCAD pulse program with an acquisition time of 0.16 s and a relaxation delay of 1.5 s. The acquisition in ^{13}C consisted of 256 time increments with a resolution of 79 Hz. The collected spectra were processed with MestReNova (version 14.0.1, Mestrelab Research). Qualitative analysis was performed to determine the relative abundance of aromatic units G, H, and S in each lignin feedstock.

3.2.2.3 Transmission Electron Microscopy

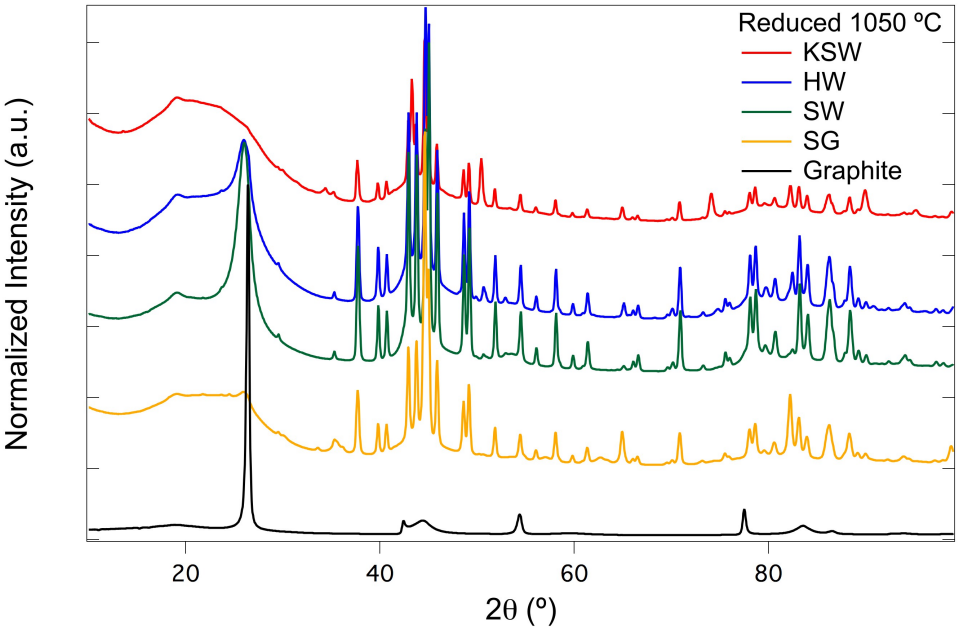
Transmission electron microscopy (TEM) was performed to provide independent evidence of local structure to corroborate observations from x-ray scattering. Carbon composite powder was mixed with methanol, 0.2:99.8) wt.% respectively, and sonicated for 20 min to allow separation of particles. A drop of the solution was suspended in the surface of a lacey carbon 200 mesh copper grid that is specific for TEM from EMS (Cat. # LC200-CU). The sample holder was inserted in the chamber of the Libra 200 MC, where the column vacuum pressure was lower than 2.0×10^{-6} mbar with an accelerating voltage of 200 kV. Diffraction patterns of carbon composites were analyzed using custom Python code. The images were imported, then centered and aligned to one of the rings. Diffraction data was converted to polar coordinates and plotted to obtain an intensity profile. A peak fit was performed to determine Bragg's peaks, structure factors were calculated, and ring patterns were modeled with graphite in order to index the peaks. Experimental data in Cartesian coordinates was overlaid with the rings.

3.3 Results and Discussion

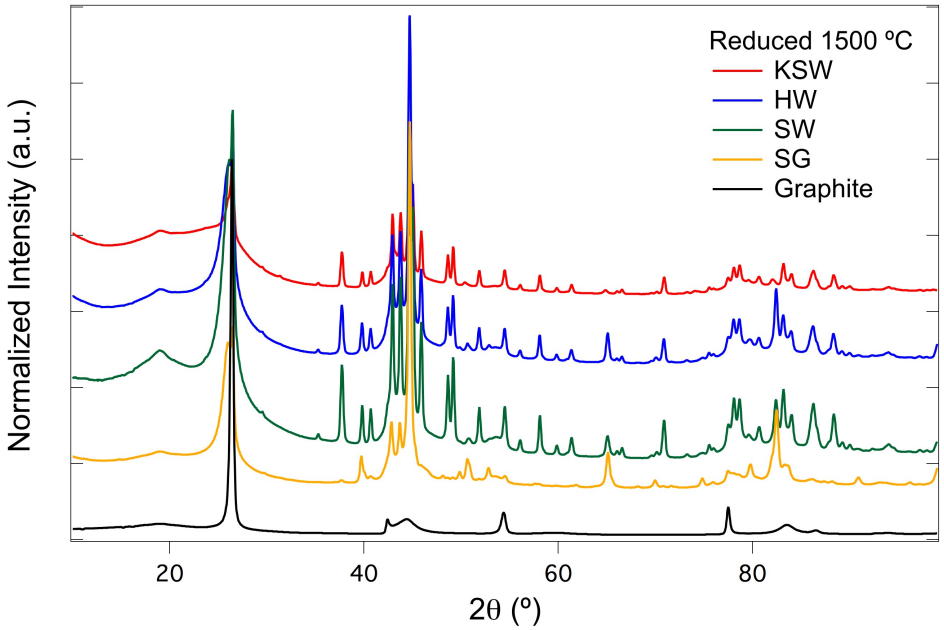
Characterization of lignin feedstocks was conducted using a high-resolution x-ray diffractogram from a synchrotron source. The experiments produced both x-ray diffraction patterns as a function of 2θ as well as PDFs. Both the diffraction patterns and the PDFs are useful given that they emphasize features from different regions of the pattern and thus provide different insights. The diffraction patterns show the positions of scattering planes and can be used to visualize the extent of graphitization in the material as a function of processing condition. The PDFs provide direct insight into the atomic structure of the carbon composites.

The normalized intensity against 2θ position was evaluated for kraft softwood (KSW), organosolv hardwood (HW), organosolv softwood (SW), and organosolv switchgrass (SG) for reduction temperatures 1050, 1500, and 2000 °C (Figure 3-2). The carbon composites were compared to a graphite standard that contains peaks at crystallographic planes: (002), (010), (011), (004), (013), (110), (112), (021), and (022) with corresponding 2θ positions of 26.5°, 42.4°, 44.6°, 54.7°, 59.8°, 77.5°, 83.5°, 93.9°, and 98.5°. The most general characteristic of Figure 3-2 is that carbon composites from all lignin feedstocks show a variety of peaks. Some of the most prominent peaks correspond to graphite peaks. The peaks are sharper for the lignin carbon reduced at high temperatures. In Figure 3-2, the first sharp peak at 26.5° has the highest intensity for all carbon composites and is associated with the (002) lattice plane in graphite, which corresponds to the d-spacing of approximately 3.35 Å between the graphene sheets. The intensity of this peak ordered from highest to lowest corresponds to SW, HW, SG, and KSW composites. At 2000 °C the peak is similar in shape and intensity for all composites, indicative of crystalline domains in the material. Other peaks in the scattering pattern do not correspond to graphite peaks. In general, the non-graphite peaks are common to all feedstocks, though the magnitude varies from sample to sample. The non-graphite peaks are attributed to the presence of iron content (e.g., Fe_3C, γ-Fe, and Fe) introduced from the ball-milling process as detected by composition analysis [53, 144]. The ball-milling is performed after the pyrolysis step, which explains the absence of Fe in the raw lignin or in the pyrolyzed material. These impurities are labeled in Figure 3-3, and are also present in Figure 3-2.

Figure 3-3 presents x-ray data for all lignin feedstocks as a function of their extent of processing (raw, pyrolyzed, and reduced). The raw lignin shows the characteristic broad features of amorphous materials. KSW, in particular, presents few small peaks due to residual sulfur impurities from kraft pulping [3, 39].

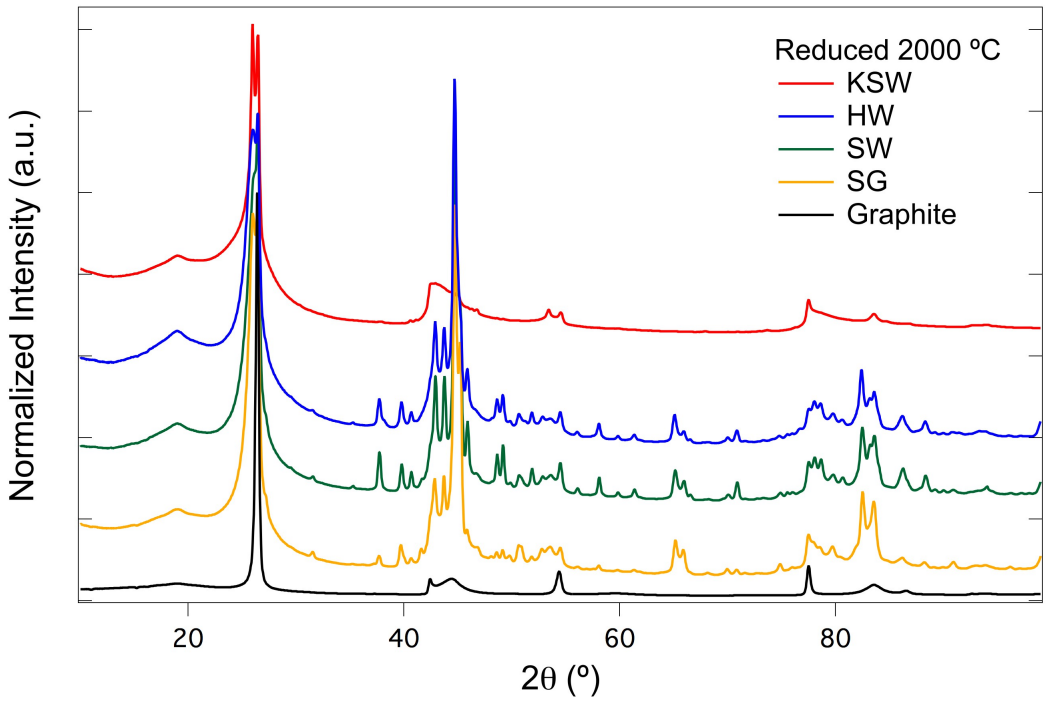


(a) Reduced at 1050 °C



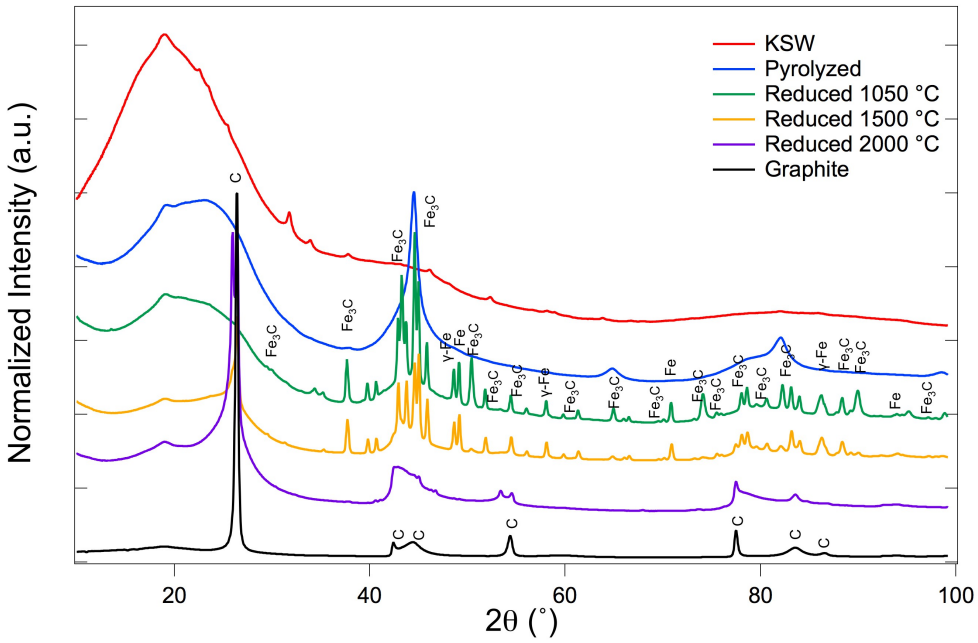
(b) Reduced at 1500 °C

Figure 3-2. Comparison of reduced lignin carbon composites.

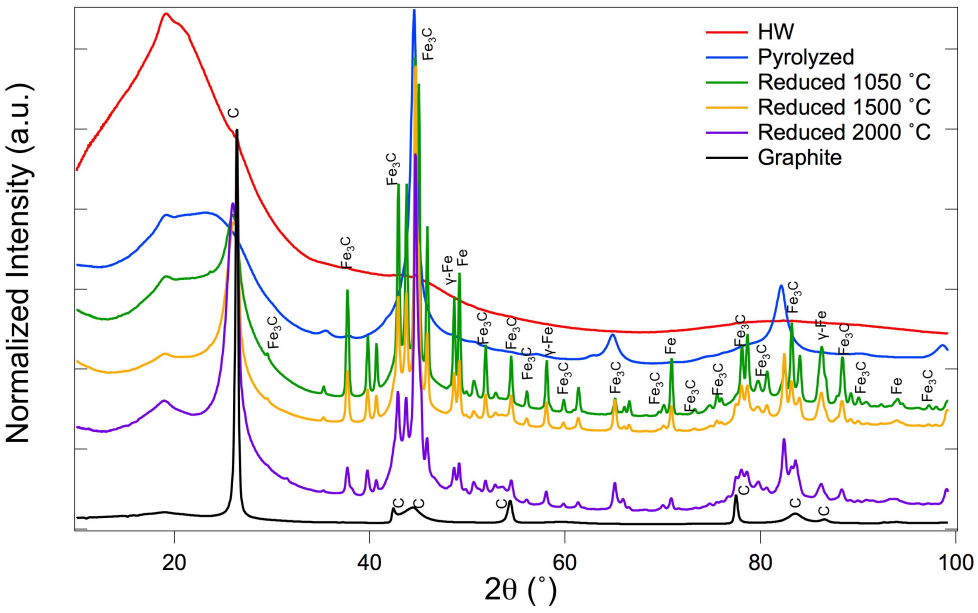


(c) Reduced at 2000 °C

Figure 3-2. (continued)

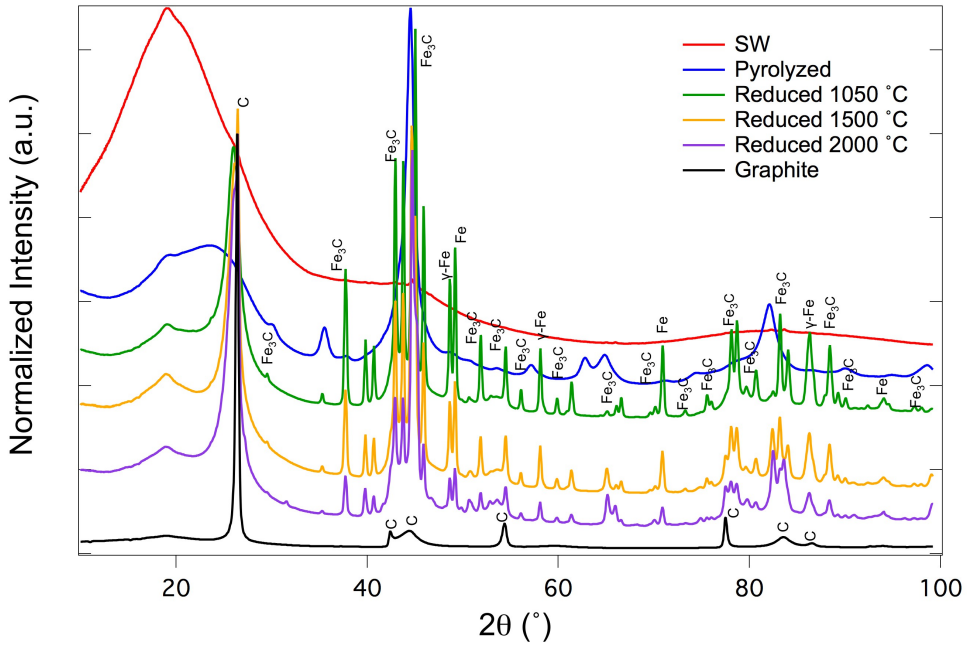


(a) Kraft softwood

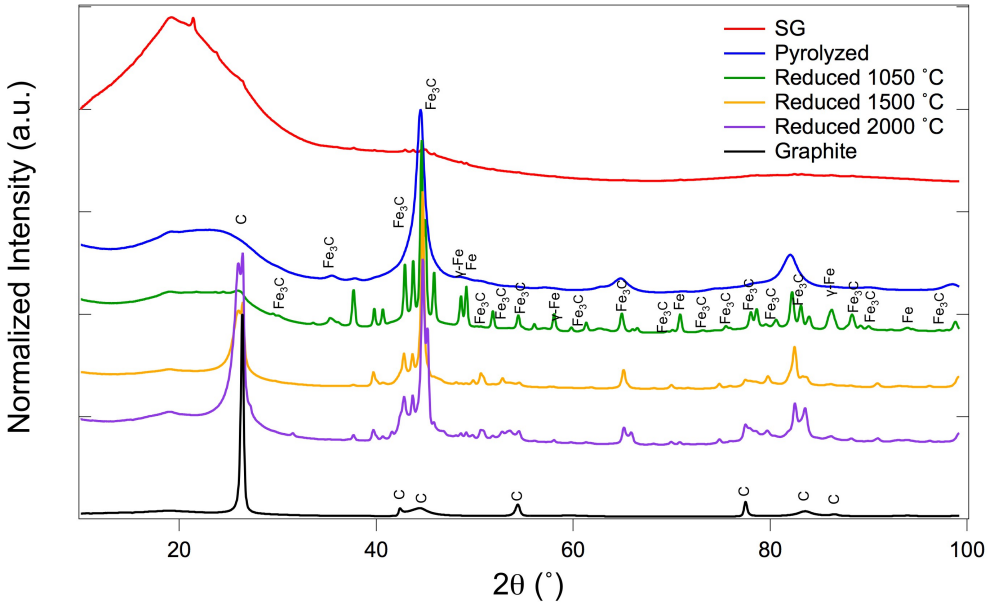


(b) Organosolv hardwood

Figure 3-3. Processed lignin carbons as a function of carbonization stages.



(c) Organosolv softwood



(d) Organosolv switchgrass

Figure 3-3. (continued)

The first processing stage, pyrolysis, decomposes the organic matter by breaking the backbone structure of the raw lignin under an inert gas environment. Specifically, H_2O, CO_2, H_2, and CO are released from the hydroxyl, carboxyl, aliphatic and methoxy, and aldehydes groups [19, 53]. Consequently, as temperature increases a rearrangement of compounds gives rise to an evolution of strongly bound aromatic structures that includes phenols, ethers, and C-C linkages. This step produces hard-carbons which are responsible for the formation of carbon structures [53, 98, 164]. For all lignin feedstocks, pyrolysis gives rise to four broad peaks centered at 2θ values of 42°, 63°, 81°, and 98°. These peaks correspond to the initial evolution of the amorphous carbon into ordered structures and as carbonization continues, they become sharp and aligned to graphite peaks, or, in the case of the peak at 63°, disappear. The peaks at 42°, 81°, and 98° are close to the (010), (112), and (022) peaks of graphite. Figure 3-2 shows, for all species, reduction at 1050, 1500, and 2000 °C results in the growth of graphite peaks with the trend that graphitic structures are preferentially formed at higher temperatures. It is evident in Figure 3-3 that the kraft softwood sample has the most graphite-like x-ray pattern followed by switchgrass sample, and both show a markedly lower presence of iron. Also, we note that there exist variations of iron contamination between samples as observed by the presence of different non-graphitic peaks.

3.3.1 Control of Crystallite Size

Gaussian peak fits and the Scherrer equation were used to measure crystallite sizes of the carbon composites from the x-ray data by identifying the full peak width at the half maxima and peak position. In Table 3-1 the crystal sizes corresponding to the largest peak at (002) lattice plane range from 4.49 to 5.55 nm for 1050 °C, 6.90 to 24.08 nm for 1500 °C, and 22.37 to 34.88 nm for 2000 °C. The increase in reduction temperature reveals larger crystal sizes in the graphitic structure. KSW and SG composites have crystallite sizes similar to graphite after reduction of 2000 °C. However, SW and HW produced the largest crystallite size, over 30 nm. It is important to note that Scherrer model and peak fits are mainly used for crystalline systems and have limitations when dealing with disordered materials containing amorphous domains [12, 31]. Previous reports of carbon composites from hardwood lignin reported graphitic crystallite sizes as much as an order of magnitude smaller in size. However, the trend of increasing crystallite size with increasing reduction temperature was observed [157].

Table 3-1. Crystallite size based on (002) plane for lignin carbons at processed reduction temperatures.

Property	Carbon composite	Reduction temperature °C		
		1000	**1500**	**2000**
***d*-spacing (nm)**	KSW	0.39	0.30	0.30
	HW	0.31	0.30	0.30
	SW	0.31	0.31	0.30
	SG	0.31	0.30	0.30
	Graphite		0.30	
Crystallite size (nm)	KSW	4.49	6.90	22.37
	HW	4.54	8.68	30.23
	SW	4.66	14.09	34.88
	SG	5.55	24.08	24.74
	Graphite		23.13	

3.3.2 Effect of Reduction Temperature

The pair distribution function reveals information of local structural properties such as average interatomic distances (peak position), structural disorder (peak width), atomic coordination number (peak area), and particle size (peak cut-off). Although the PDFs are not independent, being Fourier transforms of the scattering patterns shown in Figures 3-2 and 3-3, they are able to provide insight that is not as immediately clear when the data is plotted as a function of 2θ. Local structural details are not readily available in x-ray diffraction data which deals with average structural properties. Traditional XRD techniques are insufficient for localized nanocrystalline materials and non-crystalline materials [12, 127, 169].

In Figure 3-4, the PDF is shown for KSW at various stages in the processing. The raw lignin possesses only short-range structure. After carbonization, the short-range peaks become sharper and long-range features appear as a consequence of converting aliphatic carbon to aromatic carbon and growth of aromatic structures. These effects are more pronounced as reduction temperature is increased. Previous modeling work has shown that the peaks that arise from scattering of these materials is due to carbon pairs within the same plane of graphene. In these models [54, 105, 117], the crystalline domain was assumed to be composed of nanocrystallites of graphite. The amorphous domain was modeled as randomly oriented fragments of graphene. Therefore, both the crystalline and amorphous domains give rise to the same intraplanar peaks. The range of the peaks is therefore a combination of the size of the crystallites and the size of the fragments in the amorphous domain. The intensity of the peaks depends upon the relative volume fraction of the two domains. What is clear in Figure 3-4 is the generation and growth of graphene sheets, some of which are stacked in crystallites, with increased processing. As the sheets become sufficiently large with increased temperature, some degree of layering occurs, resulting in diffuse interfaces between the amorphous and crystalline domains, as shown by García-Negrón et al. [54]. In Figure 3-5, the PDFs for the four feedstocks reduced at three temperatures are shown. At 1050 °C (Figure 3-5a), SG exhibits the sharpest peaks over all ranges of the PDF, followed by SW, HW, and KSW. For samples reduced at 1500 °C (Figure 3-5b), SG continues to have more distinguishable peaks and, particularly, has a broader peak at 5 Å compared to the other feedstocks. On the other hand, the PDFs of HW and SW remain consistent and similar as function of temperature. Nevertheless, when samples were reduced at 2000 °C (Figure 3-5c), and in short-range distances, KSW appears the most similar to graphite having well-defined and independent peaks at 3.7–4.2 and 6.1–6.5 Å. These peaks are present in other feedstocks but seem spread out and overlap.

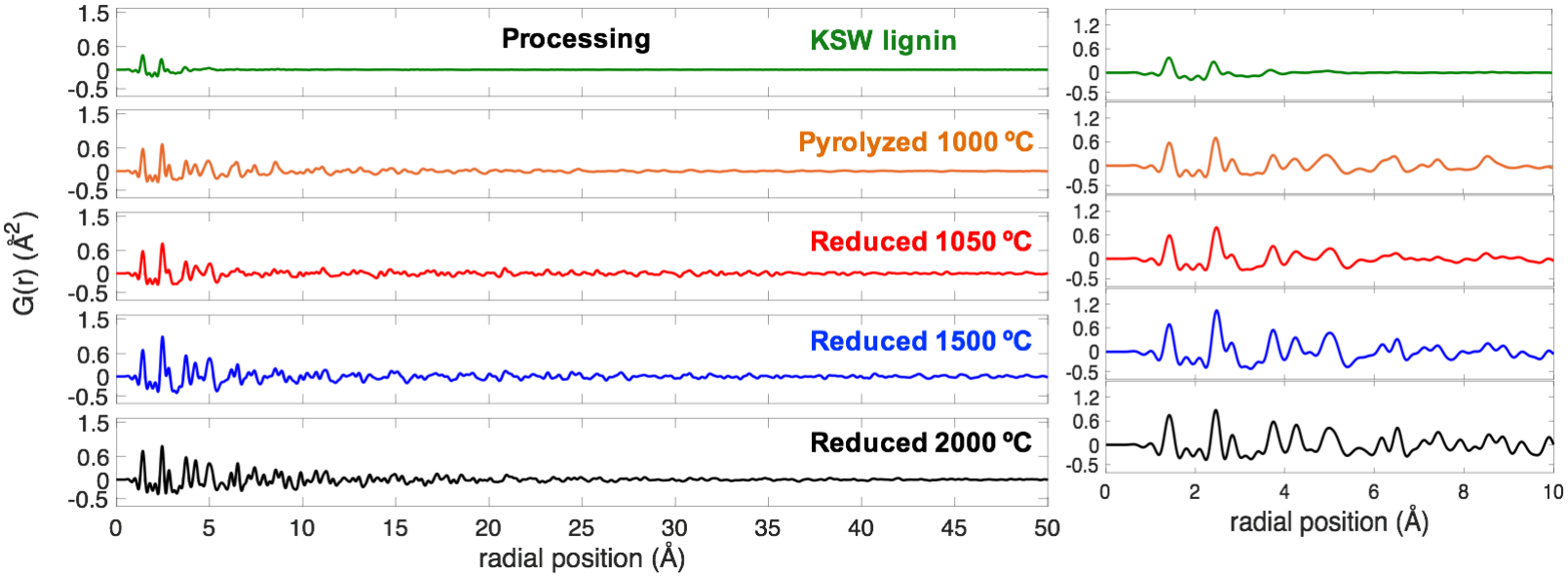
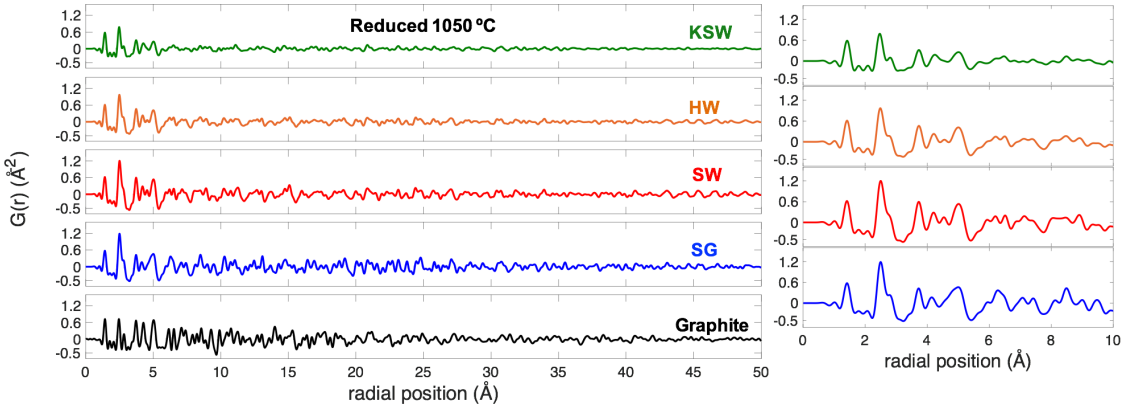
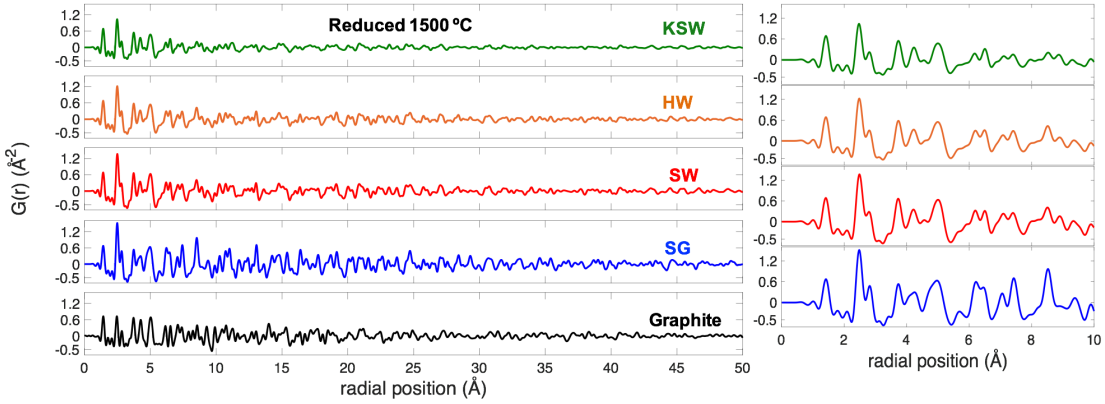


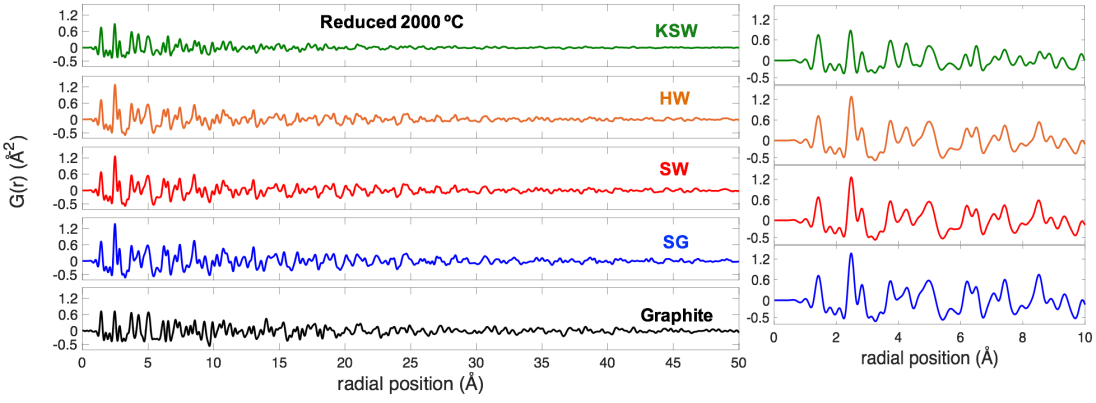
Figure 3-4. Example of KSW lignin during carbonization at reduction temperatures of 1050, 1500, and 2000 °C.



(a) Reduced at 1050 °C



(b) Reduced at 1500 °C

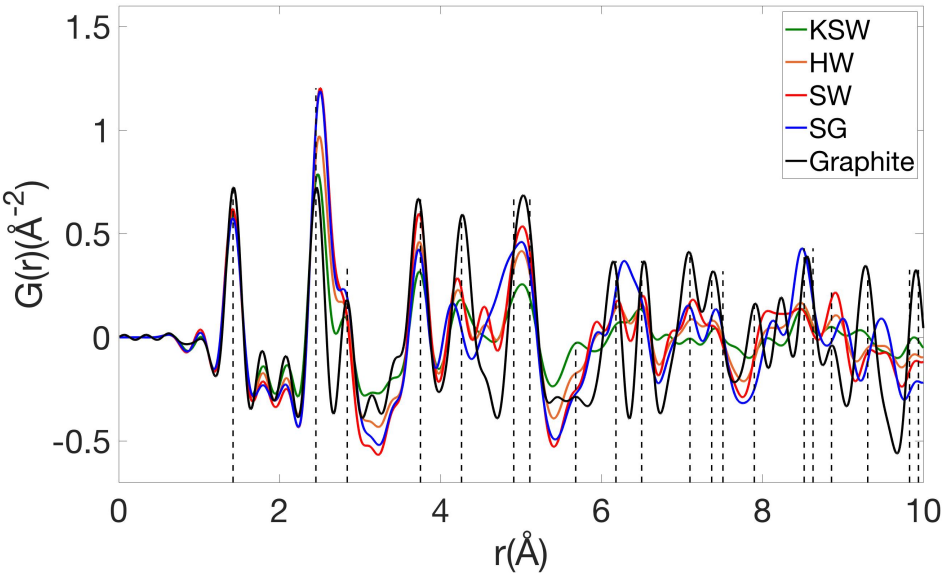


(c) Reduced at 2000 °C

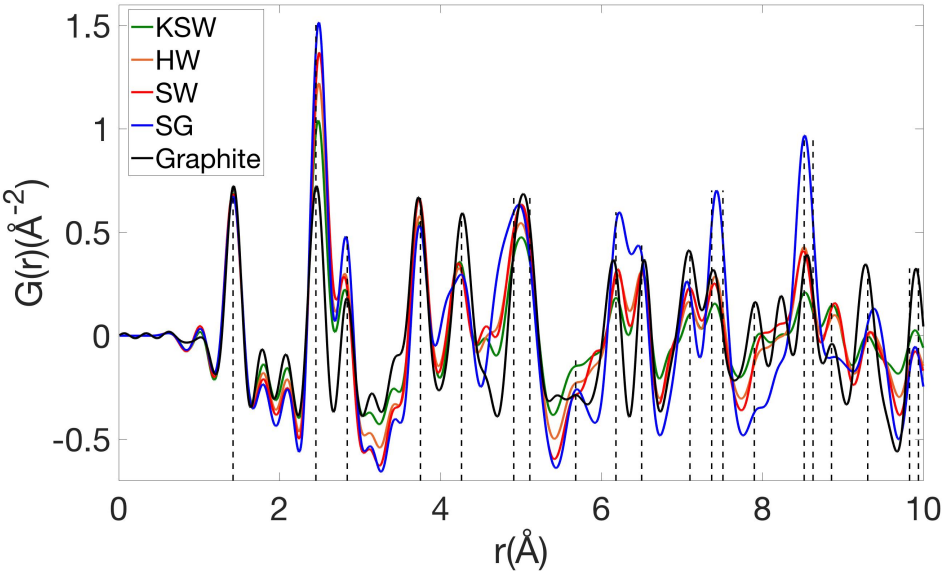
Figure 3-5. Pair distribution functions of reduced carbon composites.

The elevated temperature produces similar PDFs for SG, HW, and SW, but higher peak intensities for SG. To the eye, the differences in the PDFs are difficult to extract. However, the sample repetitions (Figure 3-1) demonstrated the reproducibility of each scattering pattern. The differences between patterns arising from different feedstocks and processing conditions is well beyond any statistical uncertainty. Therefore, in order to more clearly observe differences due to changes in feedstock and processing temperature, the short-range components of the PDFs can be analyzed, and statistical tools can be brought to bear.

To enable visual comparisons of short-range carbon pair distances between experimental and reference data, PDFs are shown from 0 to 10 Å in Figures 3-6a to 3-6c. A graphite hexagonal plane is shown in Figure 3-6d with the carbon atoms that create unique C-C neighbor distances with respect to C1 [56]. The PDF graphs present graphite and the carbon composites at all reduced temperatures, and compares the peak positions to the C-C distances obtained from an intracrystalline-intraplanar model (dashed lines) [54]. The experimental data is consistent with the atomistic model and respective peaks can be associated with an intraplanar C-C distance. This observation provides support for the model of amorphous carbon as disordered fragments of graphene. The peaks at 1.42, 2.42, and 2.84 Å correspond to the shortest C-C distances on the hexagonal rings of sp^2-sp^2 bonds [126, 155]. Values of C-C distances from reference and experimental data are included in the Appendix B. Small peaks in the PDFs appear before the first C-C neighbor peak, between the first and second neighbor peak, and between the third and fourth neighbor peak are artifacts of the Fourier transform. This was confirmed by changing the upper limit of the integration in the transform (Q_{max}) and demonstrating that the ripples changed position, while the neighbor peaks did not. From Figures 3-6a to 3-6c, the short-range structure appears relatively independent of lignin feedstock. The conceptual picture is of a carbon material possessing two compositionally similar domains, one crystalline and one amorphous, both composed of graphene fragments, though ordered differently. In the crystalline domain, the fragments are stacked into graphitic nanocrystallites, while in the amorphous phase, they remain disordered. The variability in structure as a function of feedstock tends to diminish with increasing reduction temperature. To further investigate the feature differences that arise in the PDFs as a function of reduction temperature and lignin feedstock, visual comparisons of the envelope shapes for $r^2G(r)$ are performed using Figure 3-7. Left arrows of varying sizes are used to represent the envelope shapes and due to their symmetry, they can be described with a point pair ($E_t \pm E_w$), where E_t is the tip span and E_w the shaft width. E_t provides an estimate of correlation length scale [13, 134].

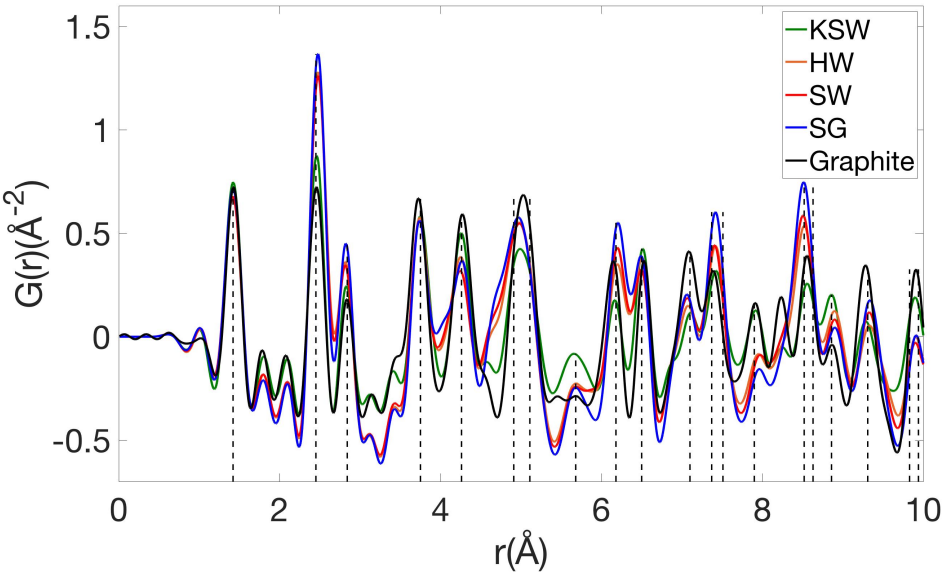


(a) Reduced at 1050 °C

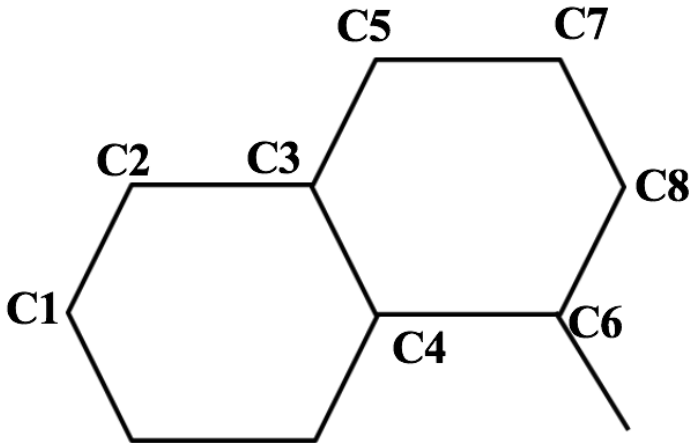


(b) Reduced at 1500 °C

Figure 3-6. PDFs of reduced carbon composites 0 to 10 Å and carbon-carbon neighbors in hexagonal plane of graphite [56]. C-C distance pairs from an intracrystalline-intraplanar model (dashed lines) are overlaid with the PDFs [54].



(c) Reduced at 2000 °C



(d) C-C neighbors in hexagonal plane of graphite.

Figure 3-6. (continued)

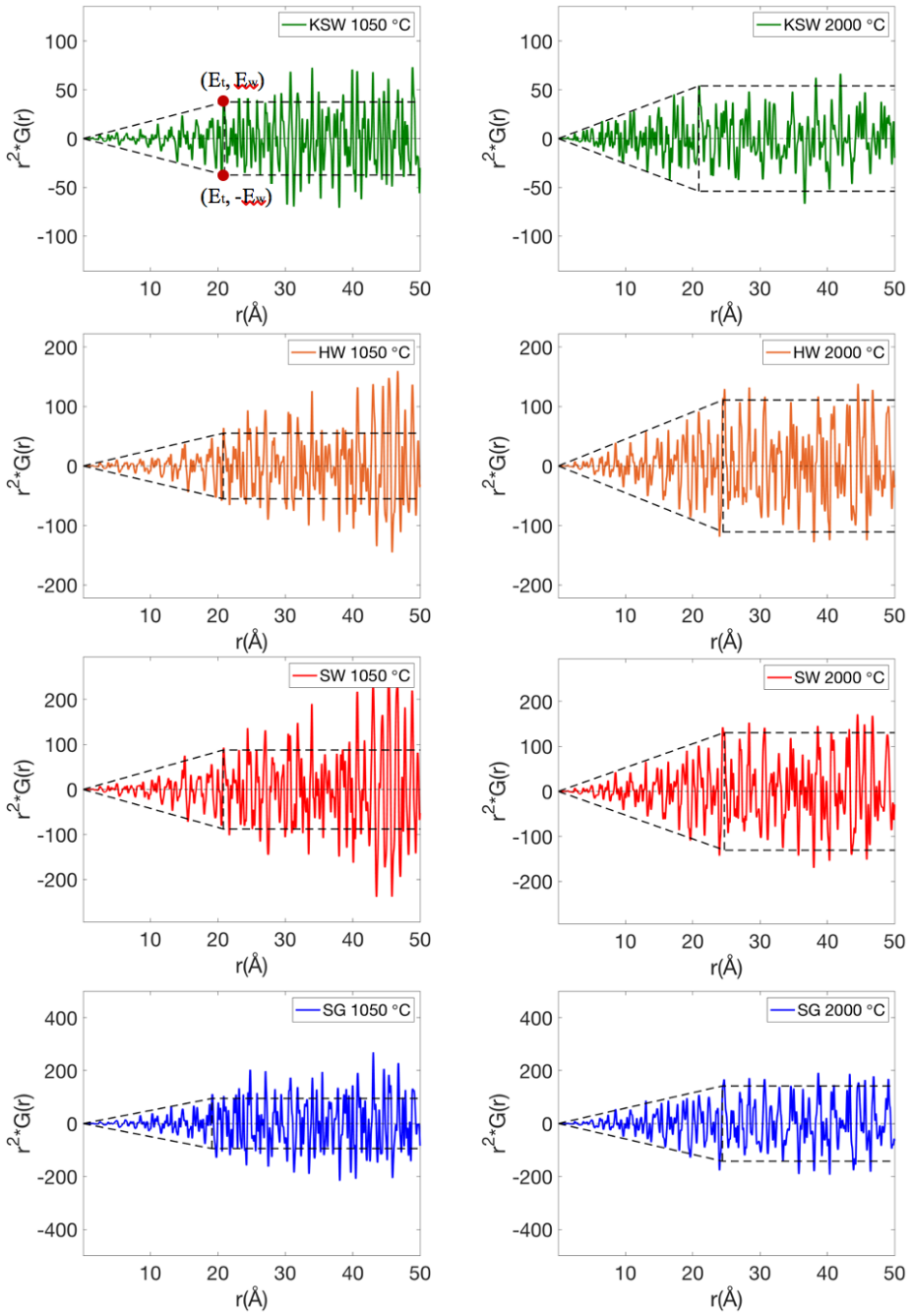


Figure 3-7. Envelope shapes of $r^2G(r)$ for lignin carbons reduced at 1050 (left column) and 2000 °C (right column). A left arrow (dotted line) outlines the general trends of PDF data and is used to gain insights on structural coherence at respective radial distances. Appendix B includes plots for graphite and carbon composite reduced at 1500 °C.

In general, the arrowhead's incremental development from $r = 0$ up to $r = E_t$ represents short and mid-range structural coherence, and a good fit in the shaft's constant span for $r > E_t$ suggests there is some structural coherence at corresponding radial distances [93, 167]. Lignin carbon composites reduced at 1050 and 2000 °C have $E_t \approx 21$ and 24.5 Å, respectively. If we associate E_t with particle radius, then for the composites reduced at 1050 °C, we have reasonable correspondence between the particle diameter from the envelope analysis (4.2 nm) and the values from the Scherrer equation in Table 3-1. The Scherrer analysis was performed on the (002) plane peak and thus estimates crystallite size normal to the planes in graphite. The application of the envelope analysis to the carbon composites reduced at 2000 °C is complicated by the fact that both the Scherrer analysis and the TEM results show crystallites larger than 50 Å, which is the maximum separation investigated in the PDF. Thus, while the PDF captures the atomic structure below 50 Å, it is not capable of providing insight regarding structure at larger length scales. The arrow widths vary with respect to reduction temperature and lignin feedstock. At 2000 °C, the envelope shapes exhibit higher magnitudes and the $r^2G(r)$ fit is tighter, supporting more coherence in long-range structures at higher reduction temperature. KSW and SG appear to have the most coherent structures given that the $r^2G(r)$ intensities vary less, and peak fluctuations are fewer.

Elemental analysis performed for each lignin feedstock during carbonization is presented in Table 3-2. As expected, carbon content increases as a function of carbonization, reaching over 90%. The largest increase of carbon content (14–18%) occurs after pyrolysis because volatile organic components containing oxygen and hydrogen are decomposed. Kraft softwood lignin achieves a higher content of carbon (99%) compared to extracted organosolv lignins (90–92%). The iron impurities from ball milling remain even at high temperatures limiting the carbon content. The KSW reaches above 99% presumably only because it did not contain by chance iron impurities. After reduction at 1500 °C, there is no notable trace of hydrogen, nitrogen, nor sulfur.

The aromatic constituents in lignin were identified using heteronuclear single quantum coherence (HSQC) spectroscopy and mapped to functional groups based on reference data found in literature [17, 69, 139, 150]. A qualitative analysis was used to characterize lignin feedstocks by integrating and normalizing over the highest peak (i.e., methoxy) from the collected spectra (see Table 3-3). All lignin feedstocks possess guaiacyl (G) units at some level. All feedstocks, with the exception of hardwood, also contain *p*-hydroxyphenyl (H) units. Hardwood and switchgrass additionally contain syringyl (S) units.

Table 3-2. Elemental analysis of lignin carbon composite at each processing condition.

Sample name[a]	**Carbon (%)**[b]	**Hydrogen (%)**[b]	**Nitrogen (%)**[b]	**Sulfur (%)**[b]	**Other (%)**[b,c]
KSW-1	62.065(0.092)	5.640(0)	0.440(0.028)	1.655(0.049)	30.200(0.170)
KSW-2	80.965(0.092)	0.800(0.127)	0.690(0)	1.165(0.007)	16.380(0.212)
KSW-3	82.185(0.078)	0.520(0.099)	0.830(0.014)	1.180(0.042)	15.285(0.233)
KSW-4	94.265(0.163)	0	0	0	5.735(0.163)
KSW-5	99.590(0.014)	0	0	0	0.410(0.014)
HW-1	64.185(0.049)	5.695(0.078)	0.260(0)	0	29.860(0.028)
HW-2	85.695(0.106)	0.615(0.021)	0.355(0.007)	0	13.335(0.134)
HW-3	89.605(0.120)	0.165(0.021)	0.305(0.035)	0	9.925(0.106)
HW-4	91.600(0.085)	0	0	0	8.400(0.085)
HW-5	91.055(0.064)	0	0	0	8.945(0.064)
SW-1	67.855(0.049)	6.625(0.007)	0	0	25.520(0.057)
SW-2	81.800(0.113)	0.575(0.035)	0.270(0.057)	0	17.355(0.205)
SW-3	87.560(0.170)	0.115(0.021)	0	0	12.325(0.191)
SW-4	88.690(0.141)	0	0.165(0.07)	0	11.145(0.148)
SW-5	90.660(0.184)	0	0	0	9.340(0.184)
SG-1	65.785(0.134)	6.280(0.014)	0.550(0)	0	27.385(0.120)
SG-2	79.685(0.021)	0.740(0.113)	0.510(0.042)	0	19.065(0.049)
SG-3	83.135(0.163)	0.395(0.106)	0.525(0.035)	0	15.945(0.021)
SG-4	88.460(0.071)	0	0	0	11.540(0.071)
SG-5	92.850(0.099)	0	0	0	7.150(0.099)

[a] The sample name is identified as follows: (1) raw lignin, (2) pyrolyzed, (3) reduced at 1050 °C, (4) reduced at 1500 °C, and (5) reduced at 2000 °C.

[b] Weight percentage

[c] **Other** represents oxygen and iron impurities

Table 3-3. Aromatic constituents in lignin characterized via 2D-HSQC spectroscopy.

Lignin feedstock	**H (%)**[a]	**G (%)**[a]	**S (%)**[a]	**S:G ratio**
KSW	1.33	26.99	-	∽ 0
SW	3.67	18.35	-	∽ 0
SG	19.67	11.48	5.74	0.50
HW	-	3.21	11.77	3.67

[a] Relative abundance w.r.t. to methoxy (Appendix B includes detailed characteristics of interunit linkages in lignin).

Guaiacyl is the dominant monomer in kraft softwood and switchgrass. *P*-hydroxyphenyl is most abundant in switchgrass and syringyl is present in the greatest amount in hardwood. Carbon composites produced from kraft lignin and with high content of G (i.e., KSW) exhibit more content of graphitic domains as established by the structural analyses from x-ray data. Relatively high graphitization is also observed for carbon composites produced from organosolv lignin and with high content of both G and H (i.e., SG). Although these observations are not strictly quantitative, they may indicate how lignin chemistry drives short-range order.

3.3.3 Correlated Effects

The PCA method was used to reduce multiple sets of 5000 PDF data points to 5 principal components. PDF data sets consist of duplicate carbon composites for each lignin feedstock, carbonization step, and humidity level. Only the first two principal components were used to visualize and cluster PDF data (Figure 3-8) because they accounted for over 90% of the variability for cases that correspond to a single carbonization temperature (i.e., pyrolysis, 1050 °C, or 2000 °C). Data points for two water contents during carbonization (18 and 105 $\mathrm{g\,m^{-3}}$) are included for each feedstock and do not disrupt the clustering observed based on feedstock. After pyrolysis (Figure 3-8a) and reduction temperature of 1050 °C (Figure 3-8b), feedstock-specific clusters are clearly segregated along with their corresponding duplicate samples. For reduction temperature of 2000 °C (Figure 3-8c), organosolv lignin clusters overlap while KSW cluster does not. This supports the general observation that the differences in carbon composite structure due to feedstock diminish as the processing temperature is increased. Note that there exists a component score in the first principal component (PC-1) that fully separates the kraft and organosolv lignin clusters. Nevertheless, when applying PCA considering all the reduction temperatures (Figure 3-8d), all clusters overlap, but KSW data is the only closely packed cluster. We attribute this difference to organosolv lignin having more OH groups and a less condensed structure making it more hydrophilic and thermally liable, while KSW contains more polysaccharide contaminants. Results support that there are inherent atomic structural properties dependent on feedstock and wood extraction method, but the influence of moisture as it relates to the atomic structure seems insignificant. We report correlation coefficients between reduction temperature and each of the 5000 data points making up the PDF, that is, $X = temperature$ and $Y = G(r = r_i)$, as was done in [7]. In Figure 3-9, linear correlations between $G(r)$ and reduction temperatures are presented. The purpose of these plots is to map PDF data to temperature effects at specific interatomic positions.

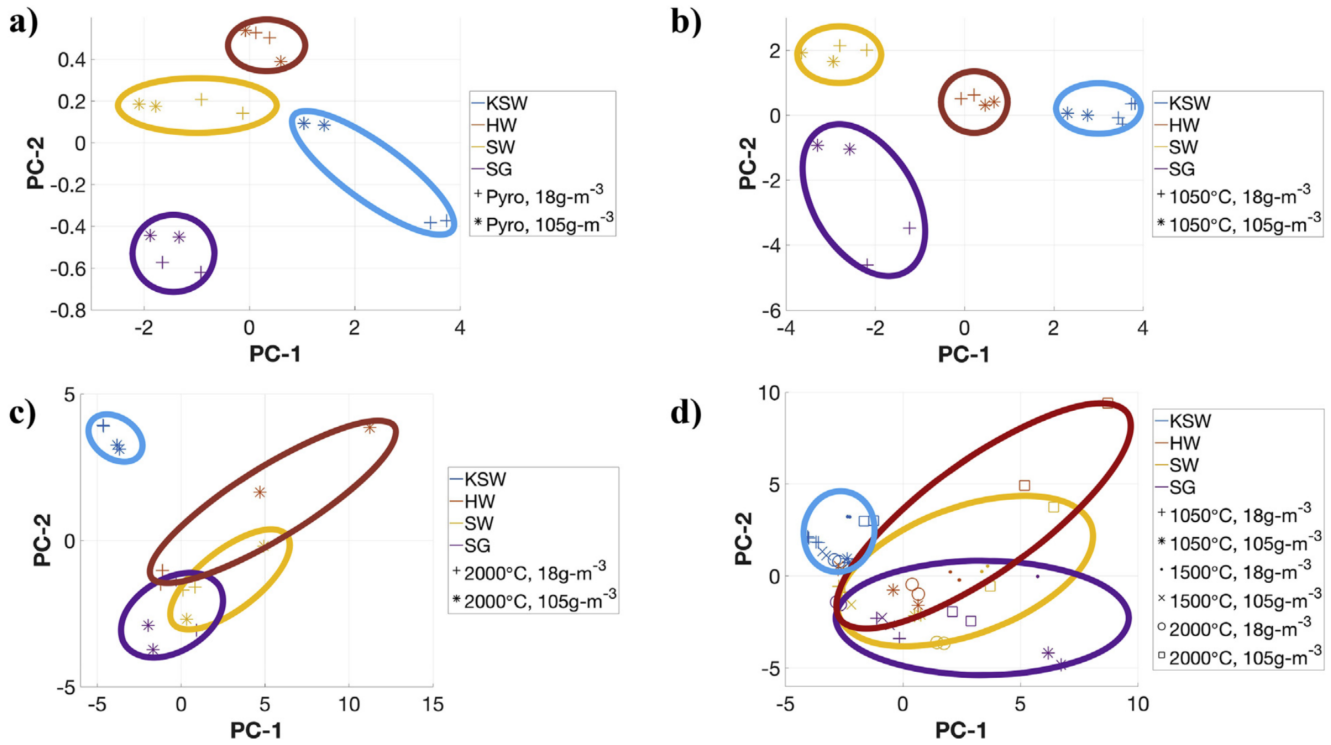


Figure 3-8. PDF carbon composites projected on first pair of principal components: a) pyrolysis, b) reduced temperature of 1050 °C, c) reduction temperatures of 1050, 1500, and 2000 °C, and d) reduced temperature of 2000 °C. Duplicate symbols represent processed samples that were repeated. RT refers to a water content of 18 g m^{-3} and HT to 105 g m^{-3}. Variance explained by each principal component: a) PC-1 (80%), PC-2 (12%), b) PC-1 (66%), PC-2 (27%), c) PC-1 (64%) , PC-2 (30%), and d) PC-1 (43%), PC-2 (26%).

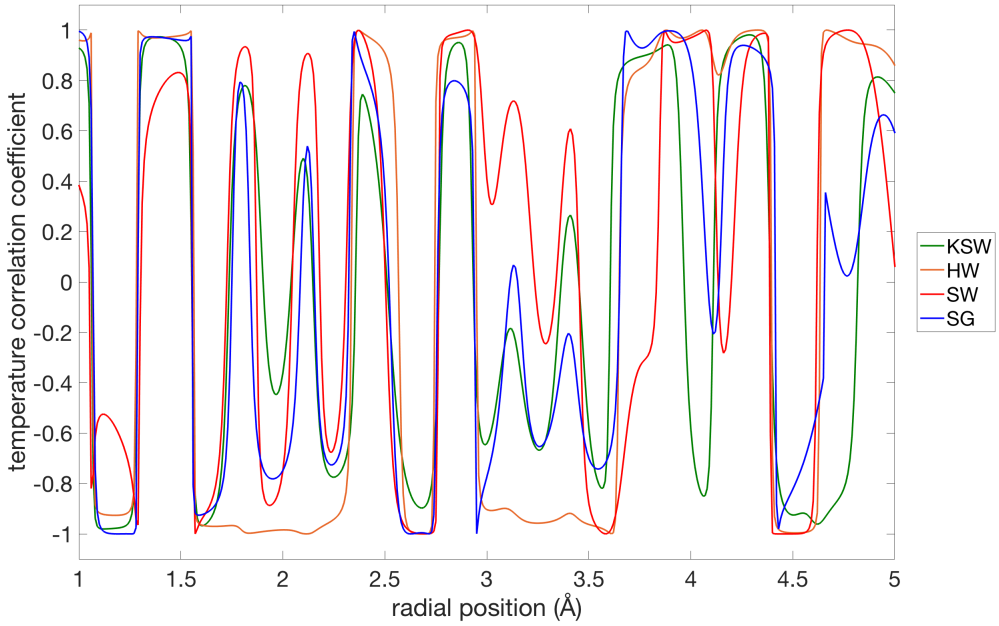


Figure 3-9. Correlations of $G(r)$ for lignin feedstock with respect to reduction temperatures. The coefficients correspond to a Pearson (linear) correlation for each radial position.

Regions of high positive correlation (i.e., greater than 0.8) are present which correspond to the graphene C-C distances and demonstrate that a higher reduction temperature correlates with an increase in peak height (structural ordering). Regions of high negative correlation (i.e., less than -0.8) are present which correspond to the valleys between C-C distances becoming less occupied with increasing order. The most notable differences based on lignin feedstock are observed at radial ranges 1.5–2.3 Å and 3.0–3.5 Å, especially for HW that has a high negative correlation. However, these regions do not include C-C distances, but rather correspond to Fourier ripples. This statistical analysis confirms the growth of distinct peaks with increasing temperature, as observed in the PDFs shown in Figures 3-5 and 3-6.

3.3.4 Atomic Structure in Carbon Composite

For a better understanding of the structure of lignin carbon materials two reduced specimens (1050 and 2000 °C) were chosen for TEM from all feedstocks. In Figure 3-10, collected HR-TEM images and diffraction patterns for carbon composites are presented. Both crystal and amorphous structures are observed on the surface of the materials, along with stacked layers. At 1050 °C all samples reveal amorphous domains with many small nanocrystal domains; and at 2000 °C exhibit significant nanocrystal domains with few amorphous features. Specifically, KSW and SG samples reduced at 2000 °C form large and thick ordered domains that are recognized by elongated onion-like, polygonized sheets and areas with dark contrast. The large uniformly oriented sheets with dark regions are distinctive of graphitic materials. Amorphous fragments are visible in HW and SW, and possibly are included in the crystallite size calculation which yielded larger crystallite sizes in Table 3-1. Overall, the morphology of the lignin carbons is consistent with the x-ray and PDF data where the development of large crystallites occurs in carbon composites reduced at the higher temperatures with KSW and SG being the most graphitic.

Figure 3-11 shows the diffraction patterns depicted in Figure 3-10 with peaks fitted and indexed based on graphite material. Diffraction pattern analysis applies image processing techniques that require tuning of parameters (e.g., resolution, b/w contrast) that affect the rings indexed. The indexed peaks present in lignin carbon lattice planes are: (002), (011), (010), (112), (122), (220), (210), (222), and (120). However, not all the peaks are present in all samples and at all reduction temperatures. The diffraction patterns in samples reduced at 1050 °C show fewer number of rings associated to graphite. KSW and SG generated similar ring patterns at 1050 °C, corresponding to the lattice planes (002), (011), and (122). HW and SW ring patterns are identical and includes (002), (011), (112), (122), and (220) lattice planes.

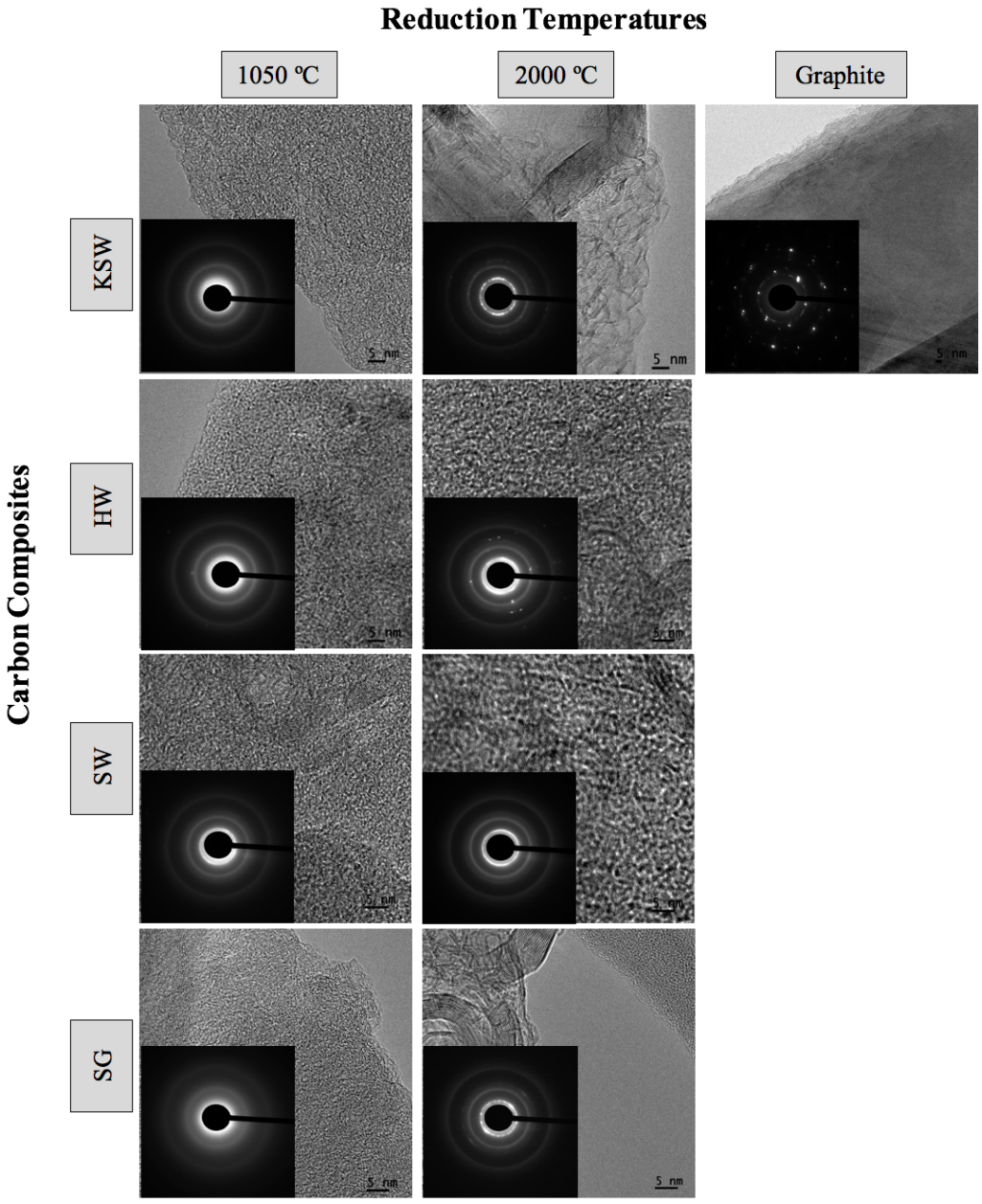


Figure 3-10. HR-TEM images and diffraction patterns of carbon composites reduced at 1050 and 2000 ℃.

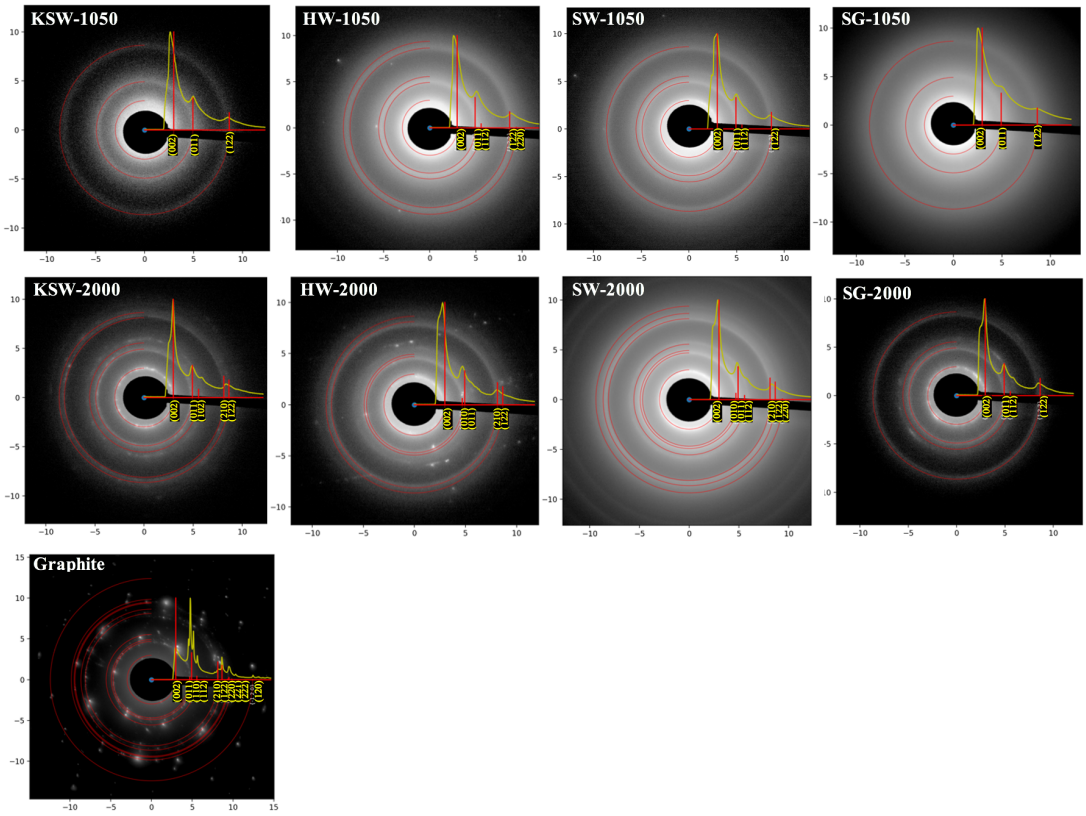


Figure 3-11. Diffracted patterns with indexed Bragg peaks of carbon composites reduced at 1050 and 2000 °C. Lines in red represent the graphite model fitted to the diffract patterns of carbon composites. The yellow line represents the actual data converted to Cartesian coordinates.

Additional graphitic peaks arise in the 2000 °C diffraction patterns for all the carbon composites. For KSW two additional planes, (102) and (210), are indexed while in SG only (112) is new. In contrast, HW planes vary between reduction temperatures 1050 and 2000 °C, but the number of planes remains the same. Lastly, in SW three additional crystal planes emerge.

3.3.5 Effect of Moisture Content

During pyrolysis we explored the effects of water content and its impact on the structure of the carbon composites. A dew point transmitter and a mass flow controller were used to measure the content of wet nitrogen entering the furnace. For KSW, five moisture contents from 0 to 105 $g\,m^{-3}$ of water were investigated at pyrolysis temperature of 1000 °C. X-ray diffraction data in Figure 3-12 shows similar peak broadening at the (002) plane for all water densities and is consistent with the crystallite sizes shown in Table 3-4. The trend of crystallite sizes is to increase monotonically as a function of higher temperature processing, see Table 3-1. These results indicate that moisture content had a modest influence at the atomic level of the structure. Corresponding PDFs included in the Appendix B also confirm minor impact at the atomic level. However, at the microstructural scale, the moisture had a more significant role. We suspect that the moisture acted as a plasticizer, changing the morphology of the carbon composite. The porosity and surface area of these materials are included in Table 3-4. These carbon materials exhibit an increase in pore volume and surface area when water content is present. In general, the surface area increases as humidity increases water molecules diffuse into the material surface and increases pore sizes as temperature rises. Study of steam and gasification processing on porosity of activated carbons exhibit similar effects [59, 140]. Pore size distribution can be observed in the scanning electron micrographs presented in Figure 3-13 for KSW, where water effects are evident in the microstructure of the hard carbon material. As humidity is increased pore density decreases and pore size increases from 100 to 300 μm. The yield is reduced with the presence of water, but it remains rather constant with respect to varying humidity. Figure 3-11 in Appendix B shows the sorption isotherms of KSW and these are representative of mesoporous materials because of its shape and hysteresis loop and, moreover, are associated with multilayer pore condensation. Also, the gradual step denotes pore heterogeneity in the material as supported by the micrographs.

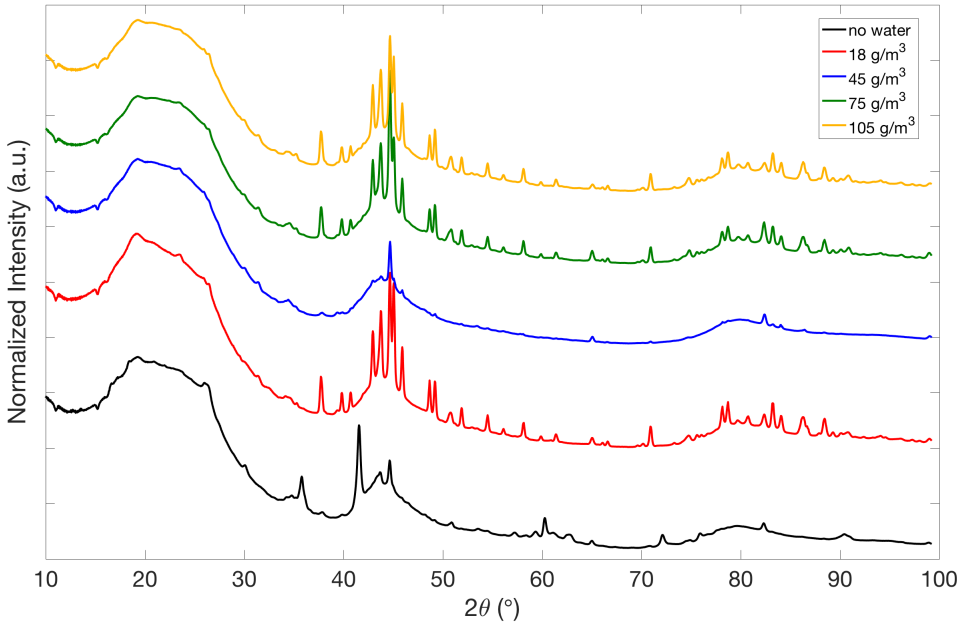


Figure 3-12. X-ray diffraction of kraft softwood at increasing water densities: 0, 18, 45, 75, and 105 g m^{-3} during pyrolysis collected at a synchrotron source.

Table 3-4. Pore volume and surface area in pyrolyzed kraft softwood with different water content.

Water density ($g\,m^{-3}$)	**Crystallite size (nm)**	**Pore volume ($cm\,m^{-3}$)**	**Surface area ($m^2\,g^{-1}$)**	**Yield after pyrolysis (%)**	**Total yield (%)**
0	2.12	0.051	31.76	42.8	29.8
18	2.12	0.140	54.20	33.4	26.3
45	2.12	0.116	78.96	33.3	26.4
75	2.12	0.658	112	37.3	27.4
105	2.12	0.082	105.0	33.5	25.7

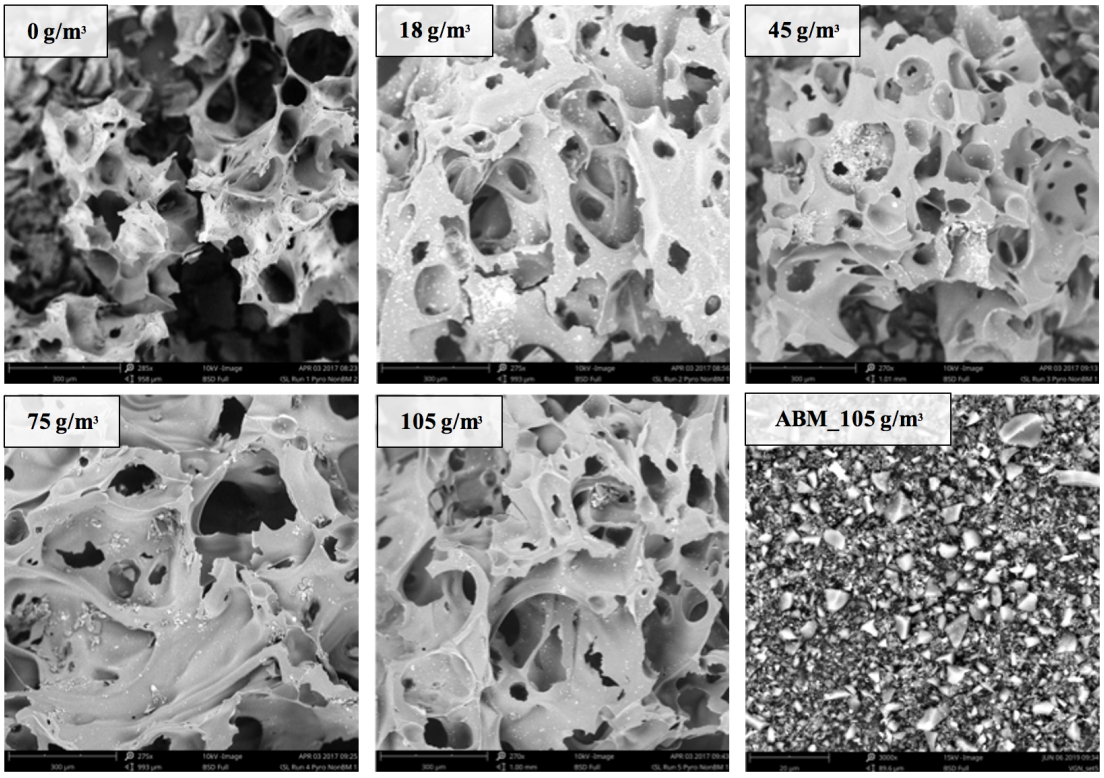


Figure 3-13. SEM micrographs show structural morphology of kraft softwood under pyrolysis at increasing water densities: 0, 18, 45, 75, and 105 g m^{-3}. A micrograph after ball milled (ABM 105 g m^{-3}) confirms particle size distribution.

3.3.6 Conclusion

Understanding the atomic and microstructural properties of renewable materials that can serve as graphite substitutes is an essential step toward low-cost and high-availability carbon-based products. Combining multiple materials characterization techniques, such as XRD, PDF, TEM, 2D-HSQC, and elemental analysis, structural relationships of lignin carbon composites were identified as a function of feedstock, carbonization temperatures, and environment conditions. Lignin samples evaluated included kraft softwood, organosolv hardwood, organosolv softwood, and organosolv switchgrass. The carbonization process consisted of pyrolysis with humidity control and reduction at high temperatures (i.e., 1050, 1500, and 2000 °C). The resulting carbon composites had a characteristic hybrid nanostructure, composed of graphitic nanocrystallites and amorphous carbon domains. X-ray diffractograms identified a broad distribution of graphitic and non-graphitic peaks for carbon composites from all lignin feedstocks. The non-graphite peaks are attributed to the presence of iron content introduced from the ball-milling process. After pyrolysis, peaks become sharper due to the formation of graphitic structures, and only particular non-graphitic species remain. This trend is further observed at high reduction temperatures (2000 °C) where significant peaks that remain correspond to graphite and reveal larger crystal sizes. In particular, KSW and SG had a lower presence of iron peaks and crystal sizes similar to graphite.

PDF analysis showed short-range features increased in intensity and long-range features appear after carbonization. This confirms the growth of graphene sheets as occupancy increases in C-C distances and assemble in the carbon material as both crystalline (stacked graphitic nanocrystallites) and amorphous (disordered graphene fragments) domains. Layering occurs as the graphene sheets become sufficiently large resulting in diffuse interfaces between the amorphous and crystalline domains. Elemental analysis supported the increase in carbon content during carbonization reaching 99% for KSW and 90–92% for extracted organosolv lignins. We note that KSW and SG carbon composites contain the most graphitic structures and were produced from either kraft lignin with high G content or organosolv lignin with high G and H content, as measured via qualitative analysis.

Statistical analyses of PDFs were used to investigate the relationship between composite structure and controlled variables such as lignin feedstock, humidity, and reduction temperature. PCA suggests that there are intrinsic structural properties dependent on feedstock and wood extraction method, and independent from humidity.

Additionally, linear correlations applied to PDFs validate the evolution of graphene sheets in response to increasing reduction temperature. These conclusions are clearly visible in HR-TEM micrographs where all lignin carbon composites exhibit significant nanocrystallites at 2000 °C, and specifically, KSW and SG being the most graphitic. The investigation of moisture effects during pyrolysis on KSW composites indicate that moisture did not change the atomic structure but rather had a more significant impact on the microstructure. For example, water diffused through multiple layers in the material surface increasing pore sizes from 100 to 300 μm at water density of 105 $g\,m^{-3}$, thus forming a mesoporous surface with pore heterogeneity as supported by sorption isotherms. Characterization of nano and mesostructures of lignin carbon composites propose KSW and SG as more favorable sources for graphite substitutes, relative to HW and SW. These processing techniques provide a means for converting renewable sources, made in-house, to an accessible carbon product.

CHAPTER 4

STRUCTURAL ANALYSIS OF CARBONIZED LIGNIN USING SMALL AND WIDE ANGLE X-RAY SCATTERING

Chapter 4 is an article in preparation for submission. The chapter contains introduction, experimental procedure, results and discussion, and conclusion.

Acknowledgements: This research was supported by a grant from the U.S. Department of Agriculture National Institute of Food and Agriculture Nanotechnology Program award number 2017-67021-26599. We acknowledge the support from the USDA National Institute of Food and Agriculture, Hatch Project 1012359. The authors thank Dr. Lin Yang who assisted with data collection during the access research proposal number 302870 and RA-301707. This research used resources from the LiX (16-ID) beamline of the National Synchrotron Light Source II, a U.S. Department of Energy (DOE) Office of Science User Facility operated for the DOE Office of Science by Brookhaven National Laboratory under Contract No. DE-SC0012704. The Center for BioMolecular Structure is primarily supported by the National Institutes of Health, National Institute of General Medical Sciences through a Center Core P30 Grant (P30GM133893), and by the DOE Office of Biological and Environmental Research (KP1605010). Also, the authors thank Eduardo Ponce for assisting with the processing of scattering data.

Abstract: Carbon composites are attractive to a variety of high-impact applications, such as carbon fibers, batteries, and vehicle parts, due to their multifunctional properties. The increase in demand for sustainable carbon sources motivates interest in understanding synthesis parameters of lignin value-added products. In this work, the thermochemical conversion of lignin powders from different feedstocks was evaluated via small and wide angle x-ray scattering techniques to resolve the amorphous, disordered, and crystalline domains present in the lignin carbons. Scattering analyses indicated an evolution of hierarchical structures along with an increase in ordered domains as a function of carbonization temperature. Qualitative and quantitative methods were used to describe isotropic scattering intensity profiles at multiple length scales. The use of power law models in the mesoscopic region served as the basis to describe morphological changes related to structural features, for example, graphene stacking, degree of roughness, and surface fractals. Kraft softwood and switchgrass produced carbon composites materials with the most crystalline domains and the least surface roughness. Softwoods reached the highest degree of crystallinity followed by switchgrass samples and attained less variability in particle sizes. Interpretation of x-ray scattering data from lignin carbon powders elucidates feedstock- and processing-dependent morphological features across multiple length scales providing a straightforward framework to evaluate the feasibility of leveraging lignin carbons for producing tunable application-specific materials.

4.1 Introduction

Lignin biopolymer is an abundant carbon source found in woody plants' cell walls that is formed from oxidative polymerization of monolignols. The highly branched polymer has a complex structure tightly bound to other wood components, such as cellulose and hemicellulose. Principal uses of lignocellulosic biomass are lignin depolymerized products and biofuels for sugar to fuel conversion [37, 60, 71, 87, 94]. An estimated 55 billion tonnes per year of lignin can be obtained from the paper and pulp industry in US and 150 billion tonnes per year globally [84]. Common extraction methods to isolate lignin are kraft, soda, and lignosulfonates, where greater than 90% percent of pulp is generated from the kraft process. This process uses NaOH and Na_2S to isolate lignin [1, 97]. However, impurities, molecular weight, and chemical properties of lignin can vary substantially based on the extraction method, plant source, plant growth region, and other factors [97, 99]. It is important to note that the pulping method also greatly changes the structure of the lignin. For example, there is a more condensed structure in kraft lignin than in organosolv lignin. The vast amount of lignin available in raw form and as a byproduct, in addition to

its sustainability, makes the biomaterial desirable for paper products, carbon fibers, resins, adhesives, batteries, chemicals, polymers, and polyurethane foams [60, 85, 97, 156].

Several research initiatives have explored the relationship between the structure of lignin and comparable carbon products containing a range of graphitic and non-graphitic structures. Graphite is composed of a parallel stacking of planar carbon layers formed by carbons with sp^2 hybrid bonding in aromatic rings. In García-Negrón et al. lignin's wood-dependent variations in lignin structure were studied at the atomic level to understand the processing-structure-property relationships of lignin carbon powders [55]. Characterization indicated that processing conditions of the residual lignin impact the crystalline volume fraction and size of the carbon product. Pyrolysis temperature (and rate) control the breaking of C-C bonds between aromatic rings to become saturated alkyls. Carbonization converts carbon structures to hard-graphitized materials and reduces thermolabile elements. Moreover, at high reduction temperatures changes in d-spacing for plane (002) and the appearance of plane (101) are influenced by translational stacking faults [53]. Morphological features of lignin-derived carbons are also dependent on both feedstock and processing, with particle sizes and porosity being the mainly affected ones [52, 152, 168]. Lignin carbons can also contain hierarchical pore structures with relatively small graphitic crystals but possess a high degree of crystallinity [137]. Adding moisture to pyrolysis step, produces porous lignin carbon materials where pore volume and surface area increase proportional to moisture content [55]. Control of pore size distribution has also been investigated in the context of lignin carbon supercapacitors [79, 111]. Lignin fibers have been produced via melt and electro-spinning methods, then thermostabilized at different rates, and carbonized to produce carbon fibers of varying tensile strengths [32, 69, 70, 107]. Hosseinaei et al. established relationships between the severity and impurities in organosolv lignin where higher carbon yield resulted from low impurity, high aromatic structures, and high severity. The observed notable differences in mesoscale structure that depended on feedstock and processing used which serves as a motivation for this study. In particular, Kraft lignin carbon fibers has exhibited graphitic formations of the (101) peak plane during heat treatment which was attributed to sulfate content from kraft pulping [61]. These studies demonstrate the degree of variability in the structure of lignin-derived carbon products. Such knowledge incites the use of state-of-the-art characterization techniques to help transform lignin into a versatile carbon source with industrial implications.

Scattering techniques provide valuable information to understand complex lignin systems at different length scales, these include, interatomic distances, precipitates, porosity, polydispersity, and morphology. The principle of scattering techniques is based on a light, x-ray, or neutron source that irradiates a sample for a given time duration. As a result of the emitted beam's wavelength (λ), incidence angle (2θ), and other parameters, the beam interacts with the sample's structural features at varying length scales, producing a series of multi-oriented scattered beams. In principle electromagnetic radiation interacts with periodic structures whose periodicity that match the wavelength of the beam. Knowing that the energy of a beam is inversely proportional to its wavelength, high energy beams penetrate smaller scale structures. Interactions between the radiation source and material structure can produce either elastic (pure constructive-interference interaction) or inelastic (destructive interference) scattering. The scattered signals are measured at a 2D detection system, integrated over time, radially averaged, and normalized to counts per unit time per pixel, to produce a 2D scattering image with distinctive ring patterns of electron densities. Rings correspond to wave vectors with a significant number of reflections. These are then correlated to structural properties of the sample material. Fourier transformations are used to convert the scattering image to a 1D intensity versus angular wavenumber profile ($I \ vs. \ q$). The wavenumber, q, corresponds to a scattering wave vector and a characteristic length, d. The relationships between emitted beam, wavenumber, and length scale are the following,

$$q = \frac{4\pi \sin\theta}{\lambda} \tag{4.1}$$

$$d = \frac{2\pi}{q} \tag{4.2}$$

Although scattering data suffers from the phase problem, that is, given that only amplitude of diffraction is measured, the phase information from incident beam is lost affecting intensity measurements due to aggregation and cancellation effects, scattering intensity profiles still provide valuable information in a wide range of scales [30, 149]. In some cases, mixed signals are captured at same length scales adding a level of ambiguity and one has to be careful when interpreting the scattering intensity profile. For this reason, scattering analysis is used to complement other structural analyses such as microscopy and diffraction. Scattering experiments are classified based on the radiation source and its distance from the sample. Small angle x-ray scattering (SAXS) is generally used to measure aggregates, average pore size, and pore size distribution as it operates in the mesoscopic regime

governed by 1–100 nm features [147]. Wide-angle x-ray scattering (WAXS) resolves the atomic scale, that is, inter-layer distance, average crystal size, and percent of crystallinity. The main difference between SAXS and WAXS is the distance between the beam source and the sample which controls the diffraction maxima detected. SAXS is positioned at a farther distance where larger structural features scatter beams at lower angles (lower q). WAXS is positioned at a closer distance where smaller structural features scatter beams at wider angles (higher q). In general, processing of scattering data consists of data reduction and data analysis. Reductions depend on the instrument's design and setup while the analysis and modeling of the scattering data are independent of the instrument setup [74, 131]. Several post-processing methods are applied to improve the signal-to-noise ratio such as background subtraction and data reduction. Popular software packages (e.g., Irena [74] and Nika [73] in Igor Pro) provide data manipulation capabilities for processing and analyzing scattering data.

Scattering intensity profiles can be analyzed via different relationships, commonly, power laws, each applicable to a range of wave vectors and corresponding to particular structural features. A Guinier analysis is generally applied at low and intermediate q to describe the size-scale associated with particle interactions such as dispersity, interference, and aggregations [96, 153]. The Guinier approximation can be used to find the radius of gyration, maximum particle diameter, and molecular weight [96]. Another scattering analysis is the Porod fit, used to describe interface properties and applies to low and intermediate q but not reaching atomic distances, typically $q < 1$ nm^{-1}. Average interface and boundary correlations across surfaces with measurable contrast scattering follow a q^{-n} relation,

$$I(q) \propto Sq^{-n} \tag{4.3}$$

where n is the Porod exponent and S is a surface-related factor. A value of $n = 4$ is representative of sharp interfaces and smooth surfaces. Sharp interfaces refer to abrupt variations in electron density along the domain length. Another scenario is when surface fractals are present, that is, dense structures with surface areas scale depending on length-scale [10]. The general form of the Porod law for fractal structures is

$$I(q) \propto S'q^{-(6-n)} = S'q^{-d_f} \tag{4.4}$$

This form can be used to determine the surface fractal dimensionality as $d_f = 6 - n$ where $2 \leq d_f \leq 3$. $n = 4$, or equivalently $d_f = 2$, corresponds to smooth surfaces and as n approaches a value of 2, the surfaces change from crumpled to eventually bent [9, 147].

Object surfaces are very rough when $d_f = 3$. Depending on the scattering curve there could be multiple sections that approximate independent Porod fits.

Fully characterizing lignin's complex structure is a challenging task, nonetheless, the use of x-ray scattering techniques has been fundamental to uncover its processing-structure relationships as a function of carbonization [53, 55]. X-ray scattering and diffraction techniques allow measuring materials properties at multiple length scales and support different domain types (amorphous and crystalline). In our case we complemented previous x-ray diffraction and microscopy work with SAXS and WAXS in order to characterize the mesoscopic regime and improve measurements of raw lignin. We have previously developed physics-based models of lignin carbon composites to validate scattering data and simulate carbonization effects [54]. X-ray scattering techniques have been used to comprehensively characterize the morphology of lignin particles [161]. In a recent study the use of thermosetting polyurethanes and lignin demonstrated distinctions between the material processing and mechanical properties; and with the aid of SAXS, controllable performance during synthesis was shown [146]. A SAXS analysis for cellulose microfibril identified the orientation of angles in the primary cell walls and the mechanical behavior related to cell growth [148]. Another study includes SAXS and WAXS diffractograms presenting the (100) plane of a hexagonal symmetry, providing pore structure information of phloroglucinol and organosolv lignin synthesized with ratios of glyoxal [66]. Saurel et al. studied ordered and disordered carbonaceous materials with SAXS providing models of atomic and pore structures for different carbons such as synthetic graphite, petroleum coke, sugar-based, carbide-derived, glassy, and active carbon [147]. Badaczewski et al. presents carbon models and WAXS experimental data to describe the inter- and intra-layer scattering of these materials [4]. They also studied the microstructural evolution of glass-like carbons and quantitatively characterized inaccessible micropores within the carbon phase via small angle neutron scattering (SANS). Li et al. describes the differences between the concepts of fractal and hierarchical aggregates in nanoparticle systems [96]. Jurkiewicz et al. converted tannin via low hydrothermal condition and made graphene-like carbon structures at 900 °C. WAXS coherent scattering domains were exhibited at sizes of 20 Å. Moreover, the study provides intrinsic carbon characteristics useful for model reconstruction, such as topological defects due to carbon, oxygen, and hydrogen bonds [83]. Jafta et al. used x-ray scattering to study microporous carbon structures via contrast matching with a fluid to readily detect pores [77]. Also, they evaluated the lateral disorder contribution described by Perret and Ruland, pore analysis, total surface and shape, and degree of disorder to correlate with electrochemical performance. Another work studies micro and atomic structures of hard

carbons and sodium storage at various heat treatments to evaluate the reversible capacity in these systems [110]. Petzold et al. presented a comprehensive SAXS characterization of sulfur distribution in carbon and lithium-sulfur batteries. SAXS analysis showed the gradual filling of pores and mesopores at high sulfur loading [129].

In our work, lignin powders from different plant species with variations in monomeric units were evaluated, specifically, softwood, hardwood, and switchgrass. The biomass materials were obtained from industrial residual that resulted from kraft pulping extraction and lignin isolated from organosolv fractionation. This work focuses on SAXS and WAXS analyses of lignin powders as a function of carbonization with the aim of determining microstructural evolution and morphological characteristics, that is, resolve the amorphous, disordered, and crystalline domains present in the lignin carbons. Qualitative methods were used to describe isotropic scattering intensity profiles at multiple length scales associated with a hierarchical structure of the lignin powders. A comprehensive description of Porod fits in the mesoscopic regime uncovers interface and boundary properties of these materials. Moreover, comparisons of crystallite sizes and crystallographic distances at varying heat treatments were used to identify the lignin materials with higher graphitization and their response to temperature changes. These results pave way to further understand synthesis parameters for lignin-derived carbons and their effects on morphological characteristics during thermal treatment.

4.2 Experimental Methods

SAXS and WAXS experiments were performed in the National Synchrotron Light Source II (NSLS-II) at Brookhaven National Laboratory (BNL). The advantage of SAXS via a synchrotron light source is its high energy beams that provide higher resolution at short times for data collection. The 16-ID beamline of the Life Science X-ray scattering instrument (LiX) was equipped with an undulator source and a Si (111) monochromator. Isotropic SAXS and WAXS were collected simultaneously on three Pilatus detectors in a continuous q-range of 0.005–3.2 Å^{-1} for lignin powders and graphite. Scanning measurements used an x-ray energy of 7.69 keV (0.61995 Å^{-1}) for SAXS and 19.09 keV (1.54 Å^{-1}) for WAXS with a vertical beam size of approximately 5 µm. Python-based software, *py4xs* [171] and custom scripts, were used for data processing such as conversion from 2D scattering images to intensity profiles, averaging triplicate measurements, background subtraction, and curve fitting. Each sample was carbonized by pyrolysis at 1000 °C to 10 °C/ min and held for 1 h in nitrogen, followed by ball milling. A subsequent reduction step using argon-hydrogen was performed for each powder sample

at three temperatures: 1050, 1500, and 2000 °C. Then, powder samples were packed in kapton capillary tubes as described in García-Negrón et al. [55]. Tubes were sealed with commercial Gorilla glue epoxy.

4.3 Results and Discussion

In this study x-ray scattering data is evaluated to resolve the structural variations of lignin powders obtained from different feedstocks and extraction methods as a function of carbonization, namely, kraft softwood (KSW), organoslv softwood (SW), organosolv hardwood (HW), and organosolv switchgrass (SG). We present both a feedstock-dependent and processing-dependent analysis considering raw lignin and heat-treated lignin after pyrolysis and reduction temperatures of 1050, 1500, and 2000 °C. X-ray scattering data was processed using standard SAXS and WAXS procedures in order to extract morphological features from the lignin powders. Given that powder samples are isotropic scatterers, the spherical averages of the scattering intensity profile are generated from the detection system.

A log-log plot of the scattered intensity (I) as a function of the scattering vector (q) can be divided into three principal regions of interest, each associated with particular length scales, refer to Figure 4-1. The first regime corresponds to $q \lesssim 0.01$ Å^{-1}, in which, generally, a Guinier fit helps describe properties of particle interactions. In the Guinier region, all lignin intensity profiles, irrespective of processing treatment, exhibit a concave curvature, generally ascribed to particle aggregation [20, 76]. As an example, Figure 4-2 presents Guinier fits for KSW lignin at each carbonization stage. After ball milling the carbon materials, aggregates and agglomerates are visible in micrographs (example in Figure 4-1) where particle size distribution ranges from 64 to 178 nm [53]. We denote the second region as the mesoscopic regime located at $0.01 \lesssim q \leq 0.26$ Å^{-1} which is analyzed using power law dependences based on equation 4.3. We refer to these Porod fits as levels and associate them with hierarchical structures measured at distinct length scales and forming fractal structures. We refer the reader to Figure 4-1 to visually associate structural features in microscopy images with scattering data and see how the hierarchy is constructed. The hierarchical structure of lignin carbons is described as stacked graphene sheets forming crystallites which are the constituents of discrete particles. Particle aggregates are represented by clusters of particles closely packed, and groups of these are called agglomerates. The Guinier and mesoscopic regimes include low to intermediate scattering vectors measured with SAXS where the intensity profile can be interpreted as correlations due to a continuous electron density between the matrix and scattering centers [116].

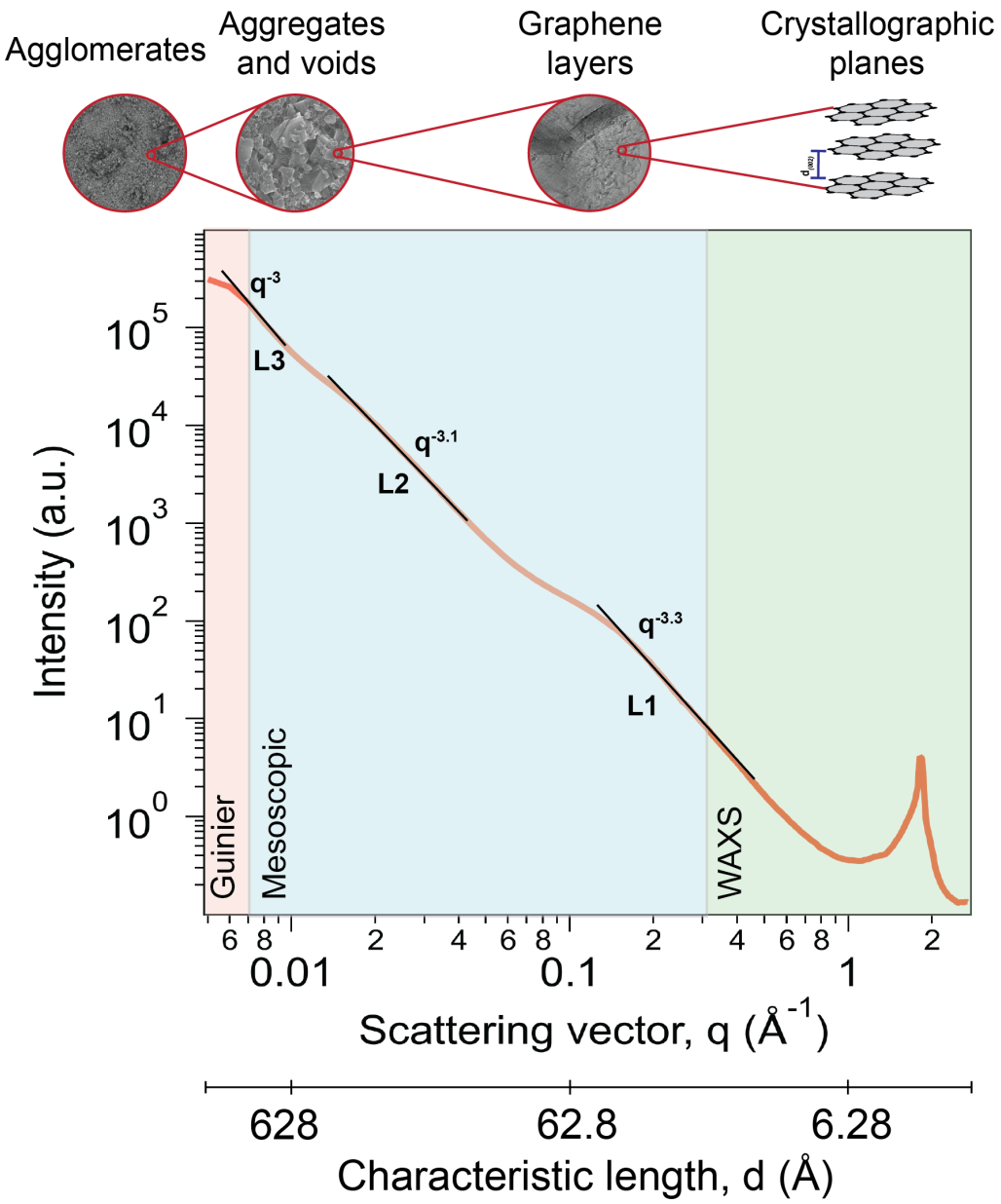


Figure 4-1. Representative SAXS and WAXS log-log intensity profile of lignin powder carbons reduced at 1500–2000 °C for the range of 0.005 ≤ q ≤ 2.68 Å. Hierarchichal structures are associated with different characteristic lengths. SAXS region describes graphene stacking in the mesoscopic regime. The mesoscopic region is further subdivided into three levels (L1–L3) where Porod fits show power law dependences. At high q, the WAXS region clearly presents the graphitic peak of plane (002).

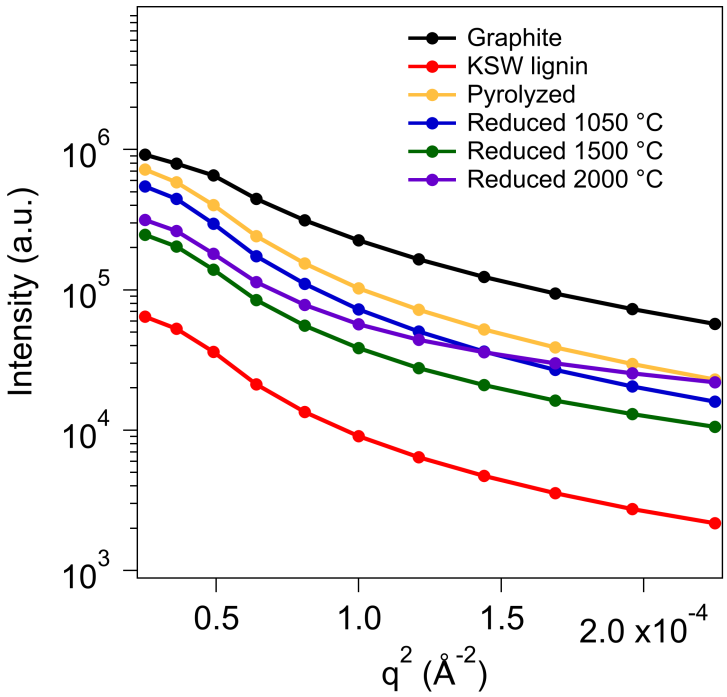


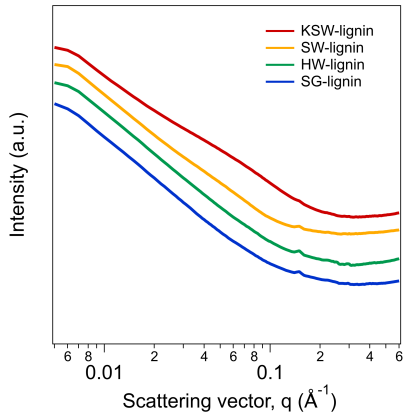
Figure 4-2. Guinier plots at $0.005 \leq q \leq 0.01$ Å^{-1} for KSW lignin powder sample presenting particle aggregation characteristics. The intensity profile of graphite is included as reference.

The third region describes atomic structures and crystallographic distances of the material, measured via WAXS at $q \geq 0.3$ Å^{-1}. Particularly, we compared d-spacing and crystallite sizes for all lignin carbons. In the following sections we discuss the scattering regions for the lignin powder samples with respect to feedstock type and carbonization.

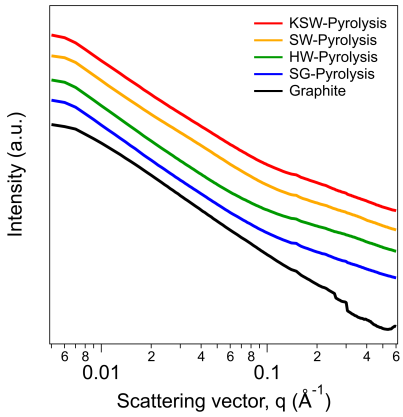
4.3.1 Analysis of Lignin as Function of Feedstock

Figure 4-3 presents SAXS profiles for comparing the lignin samples at each heat treatment and graphite. Scattering intensities of raw lignins extracted via organosolv fractionation do not exhibit significant differences, but raw kraft lignin has a mild broad feature in intensity near $q = 0.1$ Å^{-1}. The nature of KSW's unique feature is currently unknown to us but based on previous chemical analysis we associate it with the existence of extraction impurities that produce intraparticle interfaces, given that after pyrolysis KSW yields over 82% carbon content and the broad perturbation disappears [55]. On the other hand, the pyrolyzed powders have similar scattering profiles suggesting that the degree of amorphous, disordered, and ordered carbons is consistent across lignin feedstocks at this processing stage. Similarities among feedstock-based scattering profiles continue to be apparent in the reduced samples. Nevertheless, KSW presents a broad feature that increases in length scale at higher reduction temperatures indicative of emerging interfaces due to larger graphene sheets and turbostratic structures. X-ray scattering discerns variations in the structural development of lignin carbons depending on how the raw lignin was extracted. Previous clustering analysis of pair distribution functions shown in Figure 3-8 reveal the existence of structural differences between kraft lignin carbon and organosolv lignin carbons at reduction temperature of 2000 °C. Note that additional modest features appear at reduction of 2000 °C for all lignin powders and such features are more pronounced in KSW and SG supporting that these feedstocks produce carbons with more ordering and graphitic structures than SW and HW. Graphite produces a straight scattering profile in the mesoscopic regime that is associated with flat, disk-like structures having sharp scattering contrast in interfaces and smooth surfaces. These observations are in accordance with TEM and pair distribution functions discussed in García-Negrón et al. [55].

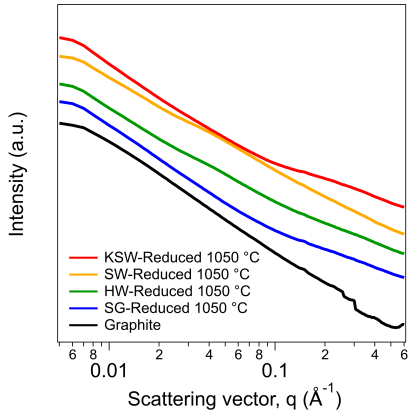
Log-log SAXS intensity profiles in Figure 4-3 exhibit multiple broad features for the lignin carbon powders, each with a subsequent power law dependence, q^{-n}, for which Porod fits were performed. For Porod fits in Table 4-1, the number of levels, identified by the distinct slopes observed in the mesoscopic region, vary among the scattering profiles. Graphite, raw lignin, and pyrolyzed lignin contain only one Porod level, whereas reduced lignin carbons have up to three Porod levels.



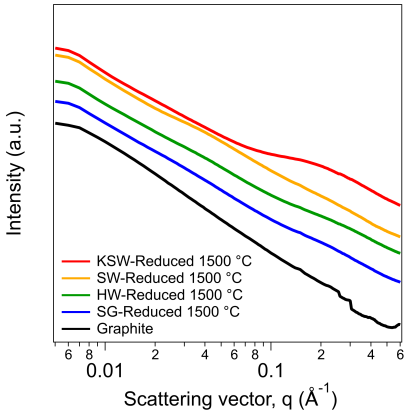
(a) Raw lignin



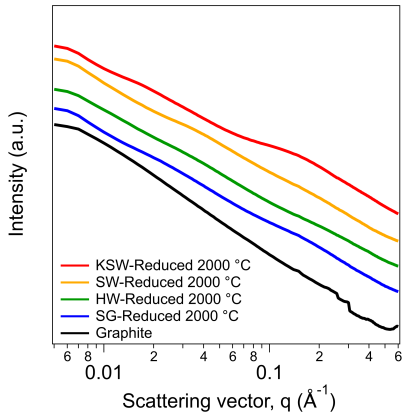
(b) Pyrolyzed lignin



(c) Carbon reduced at 1050 °C



(d) Carbon reduced at 1500 °C



(e) Carbon reduced at 2000 °C

Figure 4-3. Log-log intensity profile of SAXS for raw and carbonized lignin powders. The intensity profile of graphite is included as reference.

Table 4-1. Porod fits, $I \propto q^{-n}$, for intensity profile in SAXS for lignin carbon composite.

Property	Sample name	Lignin[a]	Pyrolysis[a]	Reduction temperature °C[a]		
				1050	1500	2000
L3 exponent	KSW	3.47	3.69	3.61	2.95	2.93
	SW	4.00	3.70	3.20	3.23	3.12
	HW	4.05	3.86	3.37	3.01	3.05
	SG	3.99	3.81	3.66	3.13	2.87
	Graphite			3.53		
L2 exponent	KSW	-	-	-	-	2.98
	SW	-	-	-	3.15	3.13
	HW	-	-	3.07	3.19	3.26
	SG	-	-	-	3.34	3.26
L1 exponent	KSW	-	-	2.04	3.00	3.36
	SW	-	-	3.11	2.45	3.18
	HW	-	-	2.19	2.80	2.85
	SG	-	-	1.98	2.94	3.30
L1 surface fractal dimension	KSW	-	-	-	-	2.64
	SW	-	-	-	-	2.82
	HW	-	-	-	-	3.15
	SG	-	-	-	-	2.70
	Graphite			2.47		

[a] Empty values exist because not all features associated with a Porod level were present in the scattering profiles of all samples.

The hierarchical components in this regime are described from larger-to-smaller structural features (in increasing q values). For these lignin materials, we labeled the region of $0.01 \leq q \leq 0.035$ Å^{-1} as level 3 (L3) and associate it with individual particles and aggregates. L3 was limited to $q = 0.02$ Å^{-1} for the carbonized lignins due to the appearance of an intermediate scattering feature. Particularly for reduced KSW and SG, L3 was extended to $q = 0.045$ Å^{-1} because they exhibit a higher degree of ordered structures at multiple length scales as indicated by previous work [55]. Most raw lignin samples have an L3 Porod exponent, $n_{L3} \approx 4$ attributed to smooth, small particles observed as a fine powder in micrographs. KSW is the exception with $n_{L3} = 3.47$. For pyrolyzed and carbonized powders, the value of $L3$ is similar between lignin feedstocks at each processing stage due to regularity in particle sizes and shapes in aggregates.

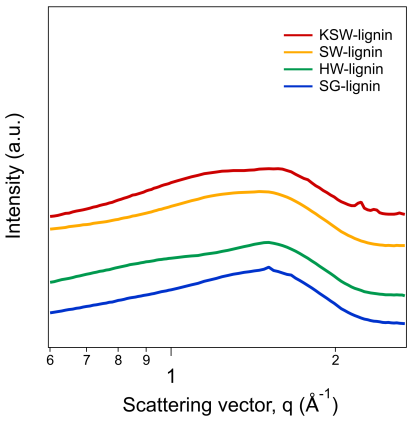
Level 2 (L2) is represented by scattering vectors $0.04 \leq q \leq 0.1$ Å^{-1} and associated with the formation of elongated graphene structures and hypothesized nanometer void spaces as observed in SEM and TEM micrographs [53, 55]. Porod analysis and evaluation of the L2 exponent did not yield convincing conclusions with respect to interface structures. Note that for all the raw lignin, pyrolyzed, and reduced carbon to 1050 °C we do not readily measure the L2 feature. Rather only for HW reduced at 1050 °C this feature exists. Also, all the reduced samples 1500 and 2000 °C exhibit these features that are attributed to the development of larger clusters of graphene stacking, refer to [55].

Surface scattering of the lignin powders is attributed to level 1 (L1), the region at $0.2 \leq q \leq 0.3$ Å^{-1} with the exception of carbon reduced at 1500 °C where L1 was taken as $0.3 \leq q \leq 0.5$ Å^{-1} due to a right-shifted scattering signal. A broad peak is characteristic of KSW and as temperature increases the peak shifts to the left. These shifts in electron density are correlated to the incident beam encountering more ordered graphene sheets in the surface boundary of the samples. For this analysis, surface roughness can be correlated to size, alignment, and order of crystalline domains. Collection of large crystalline domains parallel to a particle's surface will result in a smoother surface compared to having more disorder structures. $L1$ values between 3 and 4 suggest fractally rough surfaces of the sub-particle assembly [27]. KSW and SG have the least roughness which is the common claim that follows from evaluating these materials with complementary microscopy techniques. The TEM images in Figure 3-10 show a visual example of KSW surface with large and thick crystal sheets. We state that the lignin carbons have surface fractals at high reduction temperatures as these are visible in SEM micrograph. Table 4-1 presents the surface fractals calculated via equation 4.4. Ruland and Smarsly state that surface fractal analysis in

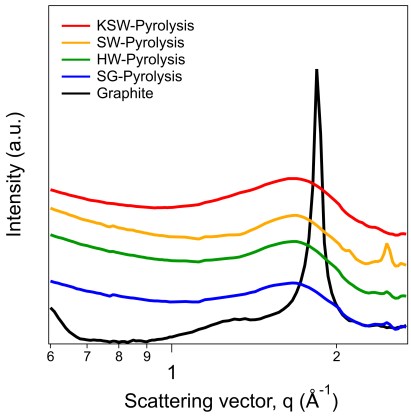
disordered carbon are incorrectly measured because the scattering contribution of imperfect graphene stacking are obtained due to the fluctuations of the interlayer spacing. Our lignin carbon powders are not fully disordered, they have a crystalline volume fraction with interlayer spacings that decrease at higher heat treatments and approximate graphite's value [142]. Interpretation of surface fractal is valid when a Porod exponent is between 3 and 4, which is the case for powder samples reduced at 2000 °C [114, 145]. The values of $L1$ surface fractal dimensionality range from 2.64 in KSW to 3.15 in HW denoting rough surfaces for all the lignin carbons.

Figure 4-4 shows the scattering profile for WAXS in the range $0.6 \leq q \leq 2.68$ Å^{-1} where evolution of the graphitic peak positioned at $q = 1.84$ Å^{-1} and corresponding to crystallographic plane (002) is distinguished. Note that raw lignin samples have a broad peak which is characteristic of amorphous domains. Although the pyrolyzed powders also have the broad peak (Figure 4-4b), discernible convex shapes appear at both sides, a sign of hybrid structures composed of crystalline and amorphous phases. By visually inspecting the graphitic peak, note how KSW and SG carbons have smoother curves compared to their lignin counterparts. Moreover, when scattering profiles are overlayed without offsets, SG has the lowest reach in intensity at $q < 1.6$ Å^{-1} while KSW has it at $q > 2$ Å^{-1}. These observations of the scattering profiles relate to higher degree of graphitic structures as evident by comparison to graphite's profile. Note that additional small non-graphitic peaks appear at $q > 2$ Å^{-1} for all feedstocks at all processing conditions and varying in number and size. These peaks correspond to iron contaminants from the ball-milling process and have been identified in García-Negrón et al. [55]. The variability of these peaks for each feedstock exists because different samples contained different amounts of iron.

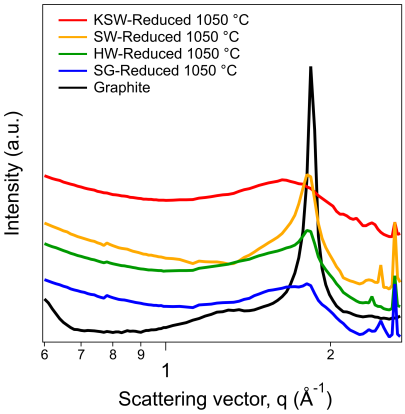
Average crystallite sizes were calculated with the Scherrer relationship (see Table 4-2) and compared to references [55, 102]. For current WAXS measurements we used Gaussian peak fits for the (002) plane peaks for calculating the interatomic distance of graphene layers and average crystallite size. García-Negrón et al. used Lorentzian peak fits instead, and McNutt et al. performed simulations of the radial distribution function for a lignin carbon composite. Table 4-2 summarizes d-spacing and crystallite size measurements for carbonized lignin samples and graphite. The estimated interatomic distances vary from 0.32 to 0.39 nm. d-spacings are very similar for each lignin carbon powder at each reduction temperature, including graphite, with KSW having the largest d-spacing in all cases. The d-spacings from WAXS data are slightly larger than those from previous studies. In terms of average crystallite sizes, SW and KSW have the largest sizes at each reduction temperature.



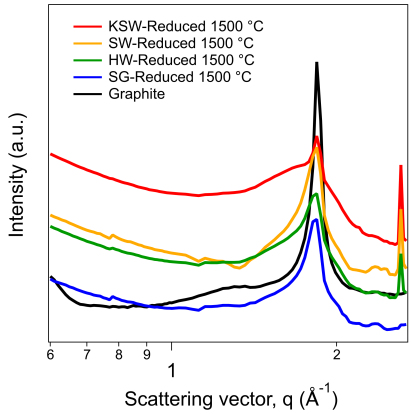
(a) Raw



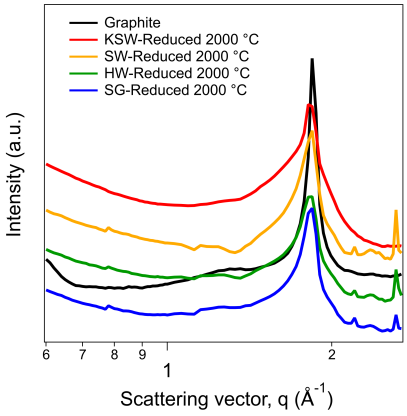
(b) Pyrolyzed



(c) Reduced 1050 °C



(d) Reduced 1500 °C



(e) Reduced 2000 °C

Figure 4-4. Log-log intensity profile of WAXS for raw and carbonized lignin powders. The intensity profile of graphite is included as reference.

Table 4-2. Characterization of the crystal plane as a function of heat treatment in the (002) plane positioned at $q = 1.84$ Å^{-1} in graphite that is observed in the WAXS region [121]. Current results are compared with measurements from two references.

Property	Reference	Sample name	Reduction temperature °C		
			1050	1500	2000
d-spacing (nm)	WAXS	KSW	0.39	0.34	0.35
		SW	0.35	0.32	0.34
		HW	0.35	0.34	0.34
		SG	0.35	0.34	0.34
		Graphite		0.34	
	García-Negrón et al. [55]	KSW	0.39	0.30	0.30
		SW	0.31	0.31	0.30
		HW	0.31	0.30	0.30
		SG	0.31	0.30	0.30
		Graphite		0.30	
	McNutt et al. [102]	HW	0.30	0.34	0.34
Crystallite size (nm)	WAXS	KSW	2.14	12.44	12.93
		SW	9.33	11.84	13.53
		HW	4.55	9.11	10.01
		SG	2.66	11.59	12.85
		Graphite		28.70	
	García-Negrón et al. [55]	KSW	4.49	6.90	22.37
		SW	4.66	14.09	34.88
		HW	4.54	8.68	30.23
		SG	5.55	24.08	24.74
		Graphite		23.13	
	McNutt et al. [102]	HW	1.00	1.40	3.40

There are notable differences between WAXS measurements and referenced works. When comparing to García-Negrón et al. we attribute the variations to the different peak fitting methods and scaling of WAXS data. We note that crystallite sizes provided by García-Negrón et al. are more consistent with graphite and complementary analyses such as pair distribution functions, therefore, are representative estimates of the actual graphitic structures in the lignin carbon powders. Figure 3-7 shows the density-density correlation functions of the lignin carbons from García-Negrón et al. exhibiting average radial distances larger than 50 Å. On the other hand, McNutt et al. crystal sizes are much smaller as supported by the density-density correlation function shown in Figure 2 of such reference.

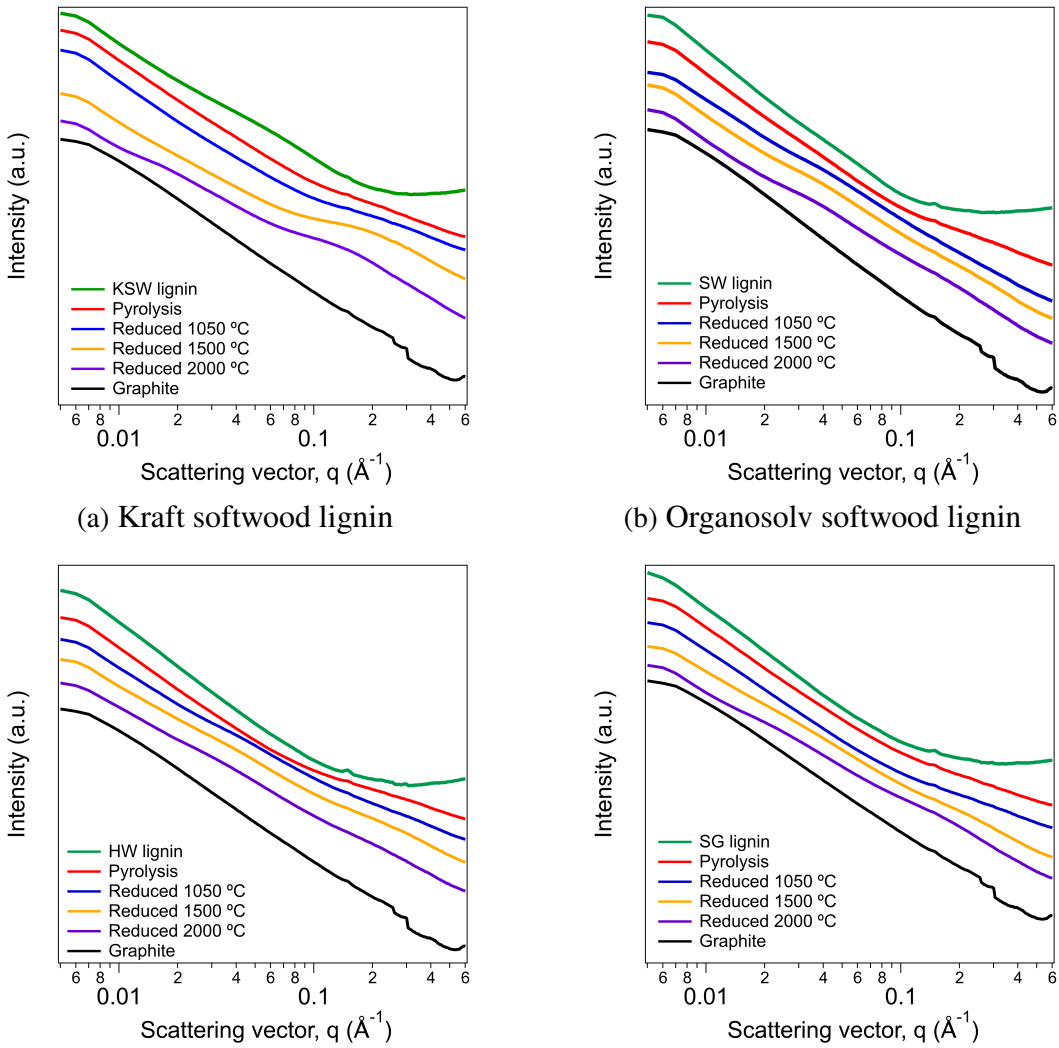
4.3.2 Analysis of Lignin as Function of Heat Treatment

As amorphous raw lignin is converted during pyrolysis stage it decomposes lignin releasing volatile organic compounds from the primary linkages in lignin and side chains, thus producing a carbon structure where changes in the scattering profile at both stages (raw and pyrolysis) are distinctive at $0.1 \leq q \leq 0.6$ Å^{-1}. The scattering signal changes from an upward curve to a downward incline for all lignin powders indicating formation of flat interfaces after pyrolysis step. In the mesoscopic region, differences are observed in the range of q that satisfies the Porod law where scattering profiles of the powder samples vary notably as reduction temperature is increased and graphitization progresses. A clear evolution of ordered structures becomes apparent as heat treatment is increased, denoted by mild broad features corresponding to levels of Porod fits.

Table 4-1 presents an inverse relationship between the magnitude of the Porod exponent and heat treatments. As reduced temperature increases the exponent's magnitude decreases until reaching $n_{L3} \approx 3$ at 2000 °C suggesting an increase in polydispersity, additional aggregations of small particles, void spaces, or a combination of these. Scattering data can produce same patterns for cases where pores and aggregate structures map to the same wave vectors. We support our observations by complementing scattering analysis with micrographs discussed in section 3.3 [55]. From the Porod fits, note that lignin samples can be separated into two groups: (1) KSW and SG and (2) SW and HW. KSW and SG have the greatest change in n_{L3} during the transition from reduced carbon at 1050 to 1500 °C. On the other hand, SW and HW have the greatest change in n_{L3} between pyrolysis and reduced carbon at 1050 °C. Also, at 2000 °C the magnitude of n_{L3} is slightly below 3 for KSW and SG, and the reverse is true for SW and HW. From our previous studies with these materials, it is known that amorphous carbon when carbonized creates turbostratic graphenes. Also, the total density of the carbon composites decreases with increasing

reduction temperature. McNutt et al. performed molecular dynamic simulations on the carbon composites supporting the aforementioned [102]. We do not have any indication of pore structures; thus, we infer the decrease in density is due to the combination of larger graphene sheets (up to approximately 30 nm) with a higher degree of disorder that in turn creates internal nanometer void spaces. These characteristic structures are responsible for the broad peaks appearing at Porod level $L2$ in the scattering profiles, see Figure 4-5. SEM and TEM images of these carbonaceous materials (see Figures 3-10 and 4-1) validate the elongation of graphene sheets with increase in temperature, the existence of particle aggregates with internal void spaces, and agglomerates [53, 55]. In Porod level $L1$, exponents' magnitude varies approximately between $n_{L1} = 2$ at 1050 °C, $n_{L1} = 2.9$ at 1500 °C and $n_{L1} = 3.3$ at 2000 °C. The exponent dependence is ascribed to changes in surface roughness where initial bent layers of graphene become stacks of crumpled layers, and eventually decreasing in roughness at higher reduction temperatures but do not reach the value of graphite ($n_{L1} = 3.53$) [147].

Figure 4-6 presents changes in WAXS data during carbonization for each lignin feedstock. The (002) plane peak sharpens as reduction temperature increases due to a gradual increase of sp^2-bonded carbons with the changes occurring from 1050 to 1500 °C, and predominant at 2000 °C, refer to Figure 4-6 [121, 147, 163]. Also, the peak position in q shifts to the right (i.e., smaller length scale) with increasing heat treatment corresponding to evolution of ordered crystals and more packed graphene layers as shown in Table 4-2 where d-spacings reach 0.34 nm for lignin carbon powders reduced at 2000 °C, matching that of graphite's. Ishimaru et al. found that in carbonized wood disordered crystals and amorphous phases decrease significantly while crystallites with stacking planes clearly develop at heat treatments above 1400 °C. For crystal sizes, results agree with the expected behavior, that is, they increase at higher reduction temperatures. This observation indicates significant microstructural ordering for these lignin carbons occurred at heat treatments close to 1500 °C. Nevertheless, all lignin carbons have crystallite sizes below half of graphite's size. In Figure 4-7 x-ray scattering profile from two beamlines from (BNL and APS) provided a clear picture of the structure variation at different length scales. After converting APS x-ray powder diffraction from 2θ to q and merging to BNL scattering data, additional crystallographic planes corresponding to graphitic structure were revealed. This highlights the benefits of being able to gather data from multiple synchrotron sources in order to get more structural information of carbon materials and enable comparisons for validation.



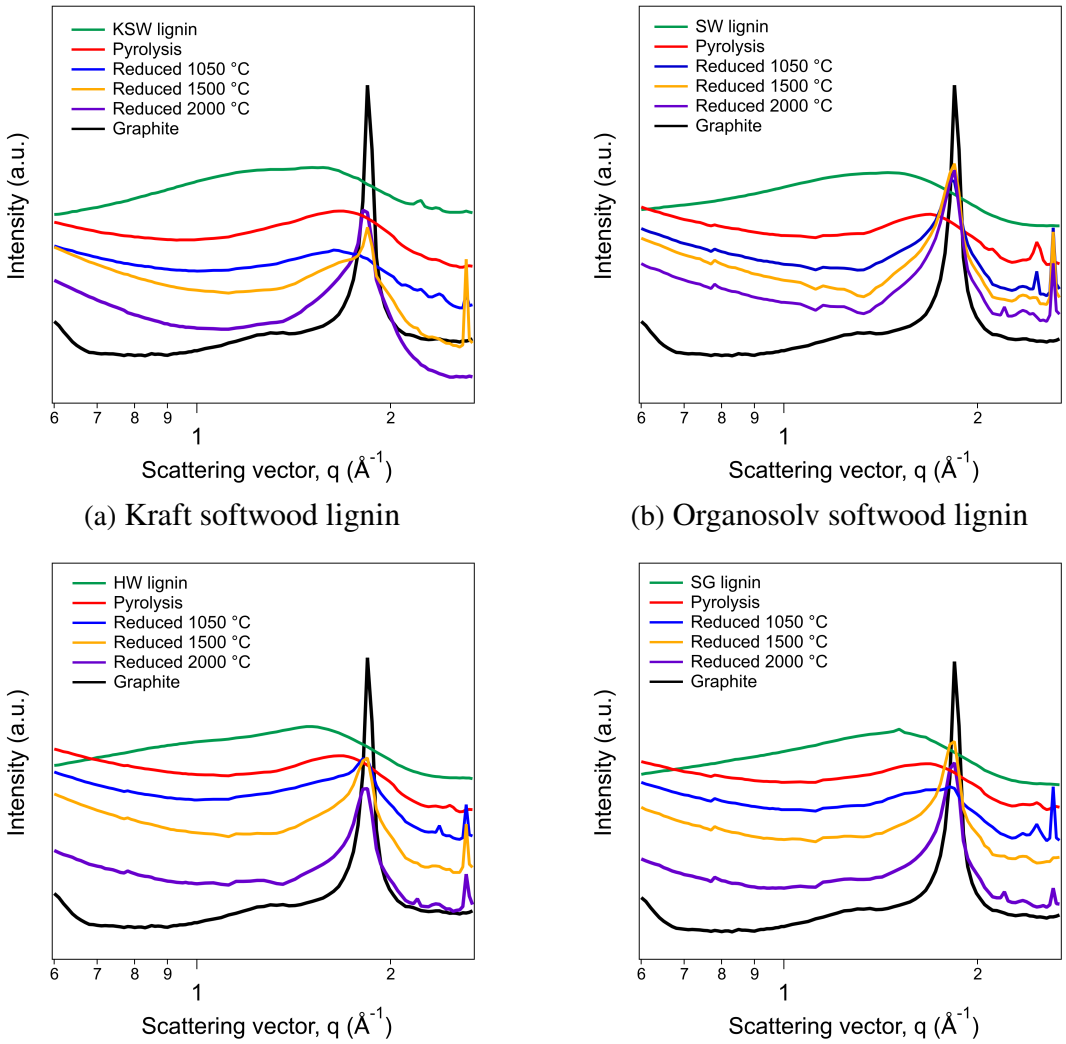
(a) Kraft softwood lignin

(b) Organosolv softwood lignin

(c) Organosolv hardwood lignin

(d) Organosolv switchgrass lignin

Figure 4-5. SAXS log-log intensity profiles for all lignin-derived powder samples. Fluctuations in scattering signal increase during carbonization among a single lignin feedstock evidencing partial graphitization.



(a) Kraft softwood lignin

(b) Organosolv softwood lignin

(c) Organosolv hardwood lignin

(d) Organosolv switchgrass lignin

Figure 4-6. WAXS log-log intensity profiles for all lignin-derived powder samples. Fluctuations in scattering signal increase during carbonization among a single lignin feedstock evidencing partial graphitization.

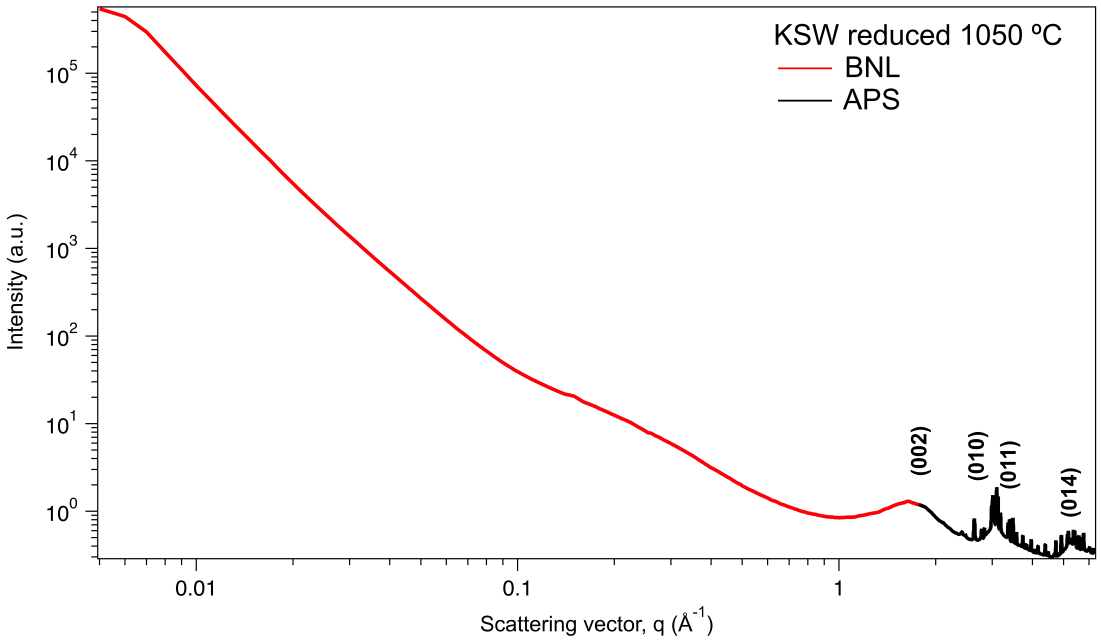


Figure 4-7. Log-log intensity profile of scattering data measured at BNL and Advanced Photon Source for KSW reduced at 1050 °C. The APS data was collected in 2θ, converted to q in the range of $1.78 \leq q \leq 6.2$ Å^{-1}, and merged. At high q the graphitic peaks corresponding to crystallographic planes (002), (010), (011), and (014) are present. Additional small peaks are due to contaminants from ball milling (Fe), refer to Figure 2 from [55].

4.3.3 Conclusion

X-ray scattering is a fundamental technique used to resolve the structural evolution and morphological characteristics of complex systems at distinct length scales. This work applies SAXS and WAXS analyses to evaluate thermochemical conversion of lignin powders (softwood, hardwood, and switchgrass) into carbonized powders. Feedstock-dependent and processing-dependent analyses considering raw lignin and heat-treated lignin after pyrolysis and reduction temperatures of 1050, 1500, and 2000 °C are presented. Scattering data indicates that structural changes occur at a wider range of domain sizes for the carbon powders, and high reduction temperature (i.e., $\geq$ 1500 °C) is the primary driver for the development of ordered and turbostratic graphene domains. Both qualitative and quantitative methods were used to describe the isotropic systems associated with hierarchical structures where crystallites form graphene sheets in particles of different sizes which in turn form aggregates and agglomerates. The scattering profiles were interpreted in two separate regions: mesoscopic and WAXS, where the former pertains to SAXS and describes particle aggregation, void spaces, and graphene stacking.

Lignin carbons exhibit variations at multiple levels of the mesoscopic region, particularly KSW, which presented broad peaks after reduction at 1500 °C indicative of larger graphitic structures than its lignin counterparts. Power law dependence methods were applied to each mesoscopic level. As reduced temperature increased the low q Porod exponent's magnitude decreased to approximately 3 at 2000 °C suggesting an increase in polydispersity, additional aggregations of small particles, void spaces, or a combination of these. The absence of pore structures suggests that stacking of ordered and disordered graphene sheets ($\sim$ 30nm) govern the scattering signal in the mesoscopic region.

Furthermore, we considered the existence of surface fractals in the most graphitic lignin carbons after examination of the high q Porod exponent which hints at a decrease in surface roughness with KSW and SG having the least rough surfaces. SAXS and WAXS, complemented with previous TEM analysis, confirm a significant increase in microstructural ordering occurs at 1500 °C with KSW reaching thermochemical stabilization first. Moreover, comparisons of crystallite sizes and crystallographic distances at varying heat treatments were used to identify the lignin materials with higher graphitization and their response to thermochemical changes. In WAXS study, the peak corresponding to (002) plane is readily apparent as carbonization progresses, shifting to higher scattering vectors with d-spacings matching that of graphite's. We conclude that carbon composites from softwoods and SG produce more ordered structures than HW

composites. This work extends previous lignin studies, paving way to elucidate processing-structure-property relationships for lignin-derived carbons and its implications in a wide range of applications.

CHAPTER 5
CONCLUSIONS

5.1 Chapter Conclusions

5.1.1 HRDF Model Development for Carbon Composite

The structures of lignin carbon composites that possess both amorphous and nanocrystalline domains have been investigated through the hierarchical decomposition of the RDF. For the study, experimental neutron scattering signatures of reduced carbon composites were interpreted using a computationally tractable model. The model achieves a reduction in computational effort up to six orders of magnitude relative to molecular dynamics simulation, making the routine tool available for complex materials. The use of the model provides both quantitative and qualitative insight into the structure of the composite, providing parameters such as volume fraction of crystalline and amorphous phases and crystallite sizes. Furthermore, the model provides parameters not directly generated from the simulation including the interface width for diffuse interfaces. The model can be generally extended to other composite materials making it suitable for MD simulation that requires high performance computation. Ultimately, these models are complementary to improve materials processing.

5.1.2 Structural Characterization of Lignin Carbon Composite

In Chapter 3, understanding the atomic and microstructural properties of renewable materials that can serve as graphite substitutes is an essential step toward low-cost and high-availability carbon-based products. The use of materials characterization techniques, such as XRD, PDF, TEM, 2D-HSQC, and elemental analysis, structural relationships of lignin carbon composites were identified as a function of feedstock, carbonization temperatures, and environment conditions. The samples evaluated included kraft softwood, organosolv hardwood, organosolv softwood, and organosolv switchgrass as function of reduction temperatures (i.e., 1050, 1500, and 2000 °C). The carbon composites exhibit hybrid nanostructure, composed of graphitic nanocrystallites and amorphous carbon domains. Also, after the pyrolysis stage, peaks become sharper due to the formation of graphitic structures, and only particular non-graphitic species remain. This trend is further observed at high reduction temperatures (2000 °C) where significant peaks that remain correspond to graphite and reveal larger crystal sizes. PDF analysis short-range features increased in intensity and long-range features appear after carbonization. This confirms the growth of graphene sheets as occupancy increases in C-C distances and assemble in the carbon material as both crystalline (stacked graphitic nanocrystallites) and amorphous (disordered graphene fragments) domains. Also, elemental analysis supported the increase in carbon

content during carbonization reaching above 90% at the reduction stages. We note that KSW and SG carbon composites contain the most graphitic structures and were produced from either kraft lignin with high G content or organosolv lignin with high G and H content, as measured via qualitative analysis. PCA suggests that there are intrinsic structural properties dependent on feedstock and wood extraction method, and independent from humidity, observed in the pyrolysis and reduction stages of carbon composites. In HR-TEM micrographs, all lignin carbon composites exhibit significant nanocrystallites at 2000 °C, and specifically, KSW and SG being the most graphitic. In conclusion, after characterization of the nano and mesostructures of lignin carbon composites KSW and SG suggest a more favorable sources for graphite substitutes, relative to HW and SW.

5.1.3 Feedstock and Processing Structure Analyses via X-ray Scattering for Lignin-Derived Carbon

Chapter 4, x-ray scattering is a fundamental technique used to resolve the structural evolution and morphological characteristics at distinct length scales of complex systems. SAXS and WAXS analyses were used to evaluate thermochemical conversion of lignin powders into carbonized powders. Scattering data indicates that structural changes occur at a wider range of domain sizes for the carbon powders, and high reduction temperature (i.e., $\geq$ 1500 °C) is the primary driver for the development of ordered and turbostratic graphene domains. Both qualitative and quantitative methods were used to describe the isotropic systems associated with hierarchical structures where crystallites form graphene sheets in particles of different sizes which in turn form aggregates and agglomerates. The scattering profiles were interpreted as three separate regions: Guinier, mesoscopic, and WAXS, where the first two regions pertain to SAXS and describe particle aggregation, void spaces, and graphene stacking. In the Guinier region, all lignin powders produced scattering profiles generally ascribed to particle aggregation, independent of processing treatment. Lignin carbons exhibit variations at multiple levels of the mesoscopic region, particularly KSW, which presented broad peaks after reduction at 1500 °C indicative of larger graphitic structures than its lignin counterparts. Power law dependence methods were applied to each mesoscopic level. As reduced temperature increased the low q Porod exponent's magnitude decreased to approximately 3 at 2000 °C suggesting an increase in polydispersity, additional aggregations of small particles, void spaces, or a combination of these. The absence of pore structures suggests that stacking of elongated ordered and disordered graphene sheets ($\sim$ 30nm) govern the scattering signal in the mesoscopic regime. Furthermore, we considered the existence of surface fractals in the most graphitic lignin carbons after

examination of the high q Porod exponent which hints at a decrease in surface roughness with KSW and SG having the least rough surfaces. SAXS and WAXS, complemented with previous TEM analysis, confirm a significant increase in microstructural ordering occurs at 1500 °C with KSW reaching thermochemical stabilization first. Moreover, comparisons of crystallite sizes and crystallographic distances at varying heat treatments were used to identify the lignin materials with higher graphitization and their response to thermochemical changes. In the WAXS study, the peak corresponding to (002) plane is readily apparent as carbonization progresses, shifting to higher scattering vectors with d-spacings matching that of graphite's. Peak fits established SW reached the highest crystal sizes followed by KSW and SG, which agrees with previous work [55]. We conclude that carbon composites from softwoods and SG produces a more ordered structure. This work extends previous lignin studies, paving the way to elucidate processing-structure-property relationships for lignin-derived carbons and its implications in a wide range of applications.

5.2 Impact and Significance

Our rapid technological progress motivates innovative research in carbon production to serve a wide variety of applications due to carbon's multifunctionality. Therefore, using sustainable alternatives such as, lignin, can reduce the cost for producing carbon. In our research, one of the goals is to establish processing-structure-properties relationships during conversion of lignin feedstocks from different plant sources to produce carbon. The implementation of a hierarchical decomposition model from radial distribution function was built to represent three temperatures of carbonization for the carbon composites. Such models help understand the materials structure at the atomic level and compared to experimental data. These approximations allow us to understand the complex systems and adapt structural parameters to refine the model. In general, the model can support similar complex systems and be extended to the other composite materials. The advantage of this model is that we can predict structural information that is needed for high computational performances. This model served as a precursor to new and more complete models currently being developed.

The extensive characterization of lignin feedstocks allows understanding the processing-structure relationships of carbon composite as a function of carbonization. Specifically, differences in carbon structures composed of nanocrystallites and amorphous domains depend on heat treatment. The study validates qualitatively that the monomer G and H content present in the KSW and SG are the ones that contain most graphitic structures from the x-ray studies. Guaiacyl content seems to have greater effect on improving graphitization

than other monomers found in lignin polymers. A key observation is that ordering of carbonaceous structures depend on lignin type and extraction method. Elemental analysis indicated that lignins extracted from organosolv softwoods exhibited higher content of oxygen when compared to kraft softwood. Thus, the condensed structures in KSW improve graphitization. Lastly, carbon composites were resolved at different scales measured via small angle and wide angle x-ray scattering, and pair distribution functions. At short distances the hexagonal nature in graphite is present and for these systems in-plane carbon-carbon distances which are coherent lengths of the domains. WAXS studies provide complementary evidence that the interlayer distances are observed to be decreasing at higher temperatures. Also, in SAXS at lower scattering wavevectors we only see larger structures in the scattering profile that describes particle aggregation, void spaces and graphene stacking for all the lignin carbon composites. This scattering complements and is consistent with TEM observation from the two reduction temperatures where the material exhibits larger graphene stacks and crystals layers. The systematic characterization and processing techniques used in this work serve as basis for understanding how to modify the lignin structure when synthesizing carbon products for specific structure-property applications.

Moreover, this work encourages the need for a global market development of carbon composites which can have high-impact in areas of applied sciences, electronics, biomedical, energy, aerospace, and other areas that the carbon properties offer. Reduction of energy systems dependent on fossil fuels is one of the challenges that needs to be addressed for future energy generation, conversion, and storage. Significant contributions towards improving development of materials from renewable sources is desirable with the goal of reducing life-cycle carbon emissions. Structural modifications and physical properties of lignin carbon composites can be addressed to improve generation and control of carbon products. Overall, this research elucidates evolution of ordered and graphitic nanostructure of bio-based carbon composites and its connection to both feedstock source and carbonization in order to establish processing-structure-properties-perfomance relationships.

5.3 Future Work

Comprehensive characterization of lignin-derived carbons is an active area of research and this work contributes processing-structure relationships of softwood, hardwood, and switchgrass as a function of extraction method and carbonization. Yet, the chemical transformations and their control are not fully understood during raw lignin carbonization. For example, what are the optimal feedstock-specific processing conditions to create

different type of lignin-derived carbon such as fibers, powders, foams, and films? This inquiry is amplified by the complex interplay between lignin nature, extraction method and impurities, processing temperature and rate, and environment. We established the presence of contaminants in our materials after ball milling with stainless steel grinding media which seem to affect properties of the lignin carbons. Alternative grinding media need to be investigated to reduce or prevent the presence of these contaminants.

Due to challenges of isolating the complex and highly branch lignin structure their molecular weights needed to be understood. For this we can study the Fourier-transform ion cyclotron resonance (FT-ICR) mass spectrometer that determines the mass-to-charge ratio of ions within a magnetic field. FT-ICR can measure masses, mass accuracy, mass range, dynamics range, and kinetics of chemical reactions depending on the magnetic field's strength. The study enables determining the elemental composition of thousands of fragments in a lignin sample. Also, the heteroatom class can be detected providing highest relative abundance from the negative ion electrospray ionization (ESI) FT-ICR for oxygen atoms (O_8) class per molecule [25] Such study can be used to correlate the heteroatoms found in the raw lignin with the graphitic evolution. Moreover, chemical formula and other parameters serve as input to model these complex systems. Gel permeation chromatography is a related technique where we can estimate average molecular weights, polydispersity, average number molecular weights in lignin.

Rate of thermochemical conversion reaction at each stage during carbonization can be measure using thermogravimetric analyzer. These parameters can be used to construct a kinetic model to calculate the activation energy, distribution of activation energy, and the frequency factor. The kinetic model can be used to identify the decomposition temperature of specific functional groups and the temperature of when graphitization starts and stabilizes. For example, Chapter 4 KSW begins graphitization by 1500 °C and other studies establish this temperature to be at 1400 °C. Ideally, we can identify these graphitization temperature for all lignin types and extraction methods. Raman spectroscopy measures inelastic scattering in all type of graphene and is used to determine the number and orientation of layers, types of preferred sites for functional groups (edge), defects and disorder, and sp^2-bonded carbon allotropes [48]. By applying Raman scattering at each carbonization stage of lignin we can resolve chemical affinity of functional groups, and variations of ordered and disordered structures, properties that cannot be measured via elastic scattering techniques.

It is important to have a front to end cost analysis for lignin carbon production, that is cost of raw lignin considering extraction methods, carbonization, and application. This is important for estimating manufacturing large scale production of lignin carbons. All the characterization conducted in this work allow room for material optimization for the choice of lignin when manufacture and processed the material to specific desired applications such as batteries, capacitors, and absorbents. Taking all these ideas into account can provide a formal means to establish processing-structure-property performance relationships for sustainable bio-derived carbons.

REFERENCES

[1] Erich Adler. Lignin chemistry–Past, present and future. *Wood Science and Technology*, 11(3):169–218, 1977.

[2] David Martin Alonso, Sikander H Hakim, Shengfei Zhou, Wangyun Won, Omid Hosseinaei, Jingming Tao, Valerie Garcia-Negron, Ali Hussain Motagamwala, Max A Mellmer, Kefeng Huang, et al. Increasing the revenue from lignocellulosic biomass: Maximizing feedstock utilization. *Science advances*, 3(5):e1603301, 2017.

[3] Abla Alzagameem, Basma El Khaldi-Hansen, Dominik Büchner, Michael Larkins, Birgit Kamm, Steffen Witzleben, and Margit Schulze. Lignocellulosic biomass as source for lignin-based environmentally benign antioxidants. *Molecules*, 23(10): 2664, 2018.

[4] F Badaczewski, MO Loeh, T Pfaff, S Dobrotka, D Wallacher, D Clemens, J Metz, and BM Smarsly. Peering into the structural evolution of glass-like carbons derived from phenolic resin by combining small-angle neutron scattering with an advanced evaluation method for wide-angle x-ray scattering. *Carbon*, 141:169–181, 2019.

[5] Pratima Bajpai. *Biermann's Handbook of Pulp and Paper: Volume 1: Raw Material and Pulp Making*. Elsevier, 2018.

[6] Pratima Bajpai. Value-added products from lignin. In *Biotechnology for Pulp and Paper Processing*, pages 561–571. Springer, 2018.

[7] Prabuddha Bansal, Mélanie Hall, Matthew J Realff, Jay H Lee, and Andreas S Bommarius. Multivariate statistical analysis of x-ray data from cellulose: A new method to determine degree of crystallinity and predict hydrolysis rates. *Bioresource technology*, 101(12):4461–4471, 2010.

[8] José Leobardo Banuelos, Guang Feng, Pasquale F Fulvio, Song Li, Gernot Rother, Sheng Dai, Peter T Cummings, and David J Wesolowski. Densification of ionic liquid molecules within a hierarchical nanoporous carbon structure revealed by small-angle scattering and molecular dynamics simulation. *Chemistry of Materials*, 26(2):1144–1153, 2013.

[9] G Beaucage. 2.14—combined small-angle scattering for characterization of hierarchically structured polymer systems over nano-to-micron meter: part ii theory. *Polymer science: a comprehensive reference. Elsevier, Amsterdam*, pages 399–409, 2012.

[10] Rogier Besselink, TM Stawski, AES Van Driessche, and Liane G Benning. Not just fractal surfaces, but surface fractal aggregates: Derivation of the expression for the structure factor and its applications. *The Journal of Chemical Physics*, 145(21): 211908, 2016.

[11] Simon JL Billinge. Nanoscale structural order from the atomic pair distribution function (PDF): There's plenty of room in the middle. *Journal of Solid State Chemistry*, 181(7):1695–1700, 2008.

[12] Simon JL Billinge. The rise of the x-ray atomic pair distribution function method: a series of fortunate events. *Philosophical Transactions of the Royal Society A*, 377 (2147):20180413, 2019.

[13] SJL Billinge, V Petkov, and Th Proffen. Structure on different length scales from powder diffraction: The real-space pair-distribution function PDF technique. *Commission on Powder Diffraction of the International Union of Crystallography Newsletter*, (24), 2000.

[14] BIOPRO Baden-Wurttemberg. Bioeconomy products. https://www.biooekonomie-bw.de/en/bw/definition/bioeconomy-products, 2019. Accessed: 2019-11-09.

[15] Salah Bouazizi, Salah Nasr, Nejmeddine Jaîdane, and Marie-Claire Bellissent-Funel. Local order in aqueous NaCl solutions and pure water: X-ray scattering and molecular dynamics simulations study. *The Journal of Physical Chemistry B*, 110 (46):23515–23523, 2006.

[16] Joseph J Bozell, Stuart K Black, Michele Myers, Deborah Cahill, W Paul Miller, and Sunkyu Park. Solvent fractionation of renewable woody feedstocks: Organosolv generation of biorefinery process streams for the production of biobased chemicals. *Biomass and bioenergy*, 35(10):4197–4208, 2011.

[17] Joseph J Bozell, CJ O'Lenick, and Stacy Warwick. Biomass fractionation for the biorefinery: Heteronuclear multiple quantum coherence–nuclear magnetic resonance investigation of lignin isolated from solvent fractionation of switchgrass. *Journal of agricultural and food chemistry*, 59(17):9232–9242, 2011.

[18] JL Braun, KM Holtman, and JF Kadla. Lignin-based carbon fibers: Oxidative thermostabilization of kraft lignin. *Carbon*, 43(2):385–394, 2005.

[19] Mihai Brebu and Cornelia Vasile. Thermal degradation of lignin—A review. *Cellulose Chemistry & Technology*, 44(9):353, 2010.

[20] Annette M Brenner, Bruce D Adkins, Stephen Spooner, and Burtron H Davis. Porosity by small-angle x-ray scattering (saxs): comparison with results from mercury penetration and nitrogen adsorption. *Journal of non-crystalline solids*, 185 (1-2):73–77, 1995.

[21] C Francisco Buitrago, Dan S Bolintineanu, Michelle E Seitz, Kathleen L Opper, Kenneth B Wagener, Mark J Stevens, Amalie L Frischknecht, and Karen I Winey. Direct comparisons of x-ray scattering and atomistic molecular dynamics simulations for precise acid copolymers and ionomers. *Macromolecules*, 48(4):1210–1220, 2015.

[22] Leichang Cao, KM Iris, Yaoyu Liu, Xiuxiu Ruan, Daniel CW Tsang, Andrew J Hunt, Yong Sik Ok, Hocheol Song, and Shicheng Zhang. Lignin valorization for the production of renewable chemicals: State-of-the-art review and future prospects. *Bioresource technology*, 269:465–475, 2018.

[23] Ewellyn A Capanema, Mikhail Y Balakshin, and John F Kadla. A comprehensive approach for quantitative lignin characterization by NMR spectroscopy. *Journal of agricultural and food chemistry*, 52(7):1850–1860, 2004.

[24] Juan C Carvajal, Álvaro Gómez, and Carlos A Cardona. Comparison of lignin extraction processes: Economic and environmental assessment. *Bioresource technology*, 214:468–476, 2016.

[25] Sabornie Chatterjee, Amy Clingenpeel, Amy McKenna, Orlando Rios, and Alexander Johs. Synthesis and characterization of lignin-based carbon materials with tunable microstructure. *Rsc Advances*, 4(9):4743–4753, 2014.

[26] Sabornie Chatterjee, Tomonori Saito, Orlando Rios, and Alexander Johs. Lignin based carbon materials for energy storage applications. In *Green Technologies for the Environment*, pages 203–218. ACS Publications, 2014.

[27] SV Chavan, PU Sastry, and AK Tyagi. Fractal and agglomeration behavior in Gd and Sm doped CeO_2 nano-crystalline powders. *Journal of alloys and compounds*, 457(1-2):440–446, 2008.

[28] Peter J Chupas, Karena W Chapman, Hailong Chen, and Clare P Grey. Application of high-energy x-rays and pair-distribution-function analysis to nano-scale structural studies in catalysis. *Catalysis Today*, 145(3-4):213–219, 2009.

[29] Peter J Chupas, Karena W Chapman, and Gregory J Halder. Elucidating the structure of surface acid sites on γ-Al_2O_3. *Journal of the American Chemical Society*, 133(22): 8522–8524, 2011.

[30] Kevin Cowtan. Phase problem in x-ray crystallography, and its solution. *e LS*, 2001.

[31] Bernard Dennis Cullity and Stuart R Stock. *Elements of X-ray Diffraction*, volume 3. Prentice hall New Jersey, 2001.

[32] Zhong Dai, Xiaojuan Shi, Huan Liu, Haiming Li, Ying Han, and Jinghui Zhou. High-strength lignin-based carbon fibers via a low-energy method. *RSC advances*, 8(3): 1218–1224, 2018.

[33] Dominik Daisenberger, Thierry Deschamps, Bernard Champagnon, Mohamed Mezouar, Raúl Quesada Cabrera, Mark Wilson, and Paul F McMillan. Polyamorphic amorphous silicon at high pressure: Raman and spatially resolved x-ray scattering and molecular dynamics studies. *The Journal of Physical Chemistry B*, 115(48): 14246–14255, 2011.

[34] Damien Dambournet, Karena W Chapman, Marina V Koudriachova, Peter J Chupas, Ilias Belharouak, and Khalil Amine. Combining the pair distribution function and computational methods to understand lithium insertion in brookite TiO_2. *Inorganic chemistry*, 50(13):5855–5857, 2011.

[35] Andrew M Danby, Michael D Lundin, and Bala Subramaniam. Valorization of grass lignins: Swift and selective recovery of pendant aromatic groups with ozone. *ACS Sustainable Chemistry & Engineering*, 6(1):71–76, 2017.

[36] Paul J De Wild, Wouter JJ Huijgen, and Richard JA Gosselink. Lignin pyrolysis for profitable lignocellulosic biorefineries. *Biofuels, Bioproducts and Biorefining*, 8(5): 645–657, 2014.

[37] M Fatih Demirbas. Biorefineries for biofuel upgrading: a critical review. *Applied energy*, 86:S151–S161, 2009.

[38] Kamal B Dhungana, Luiz FO Faria, Boning Wu, Min Liang, Mauro CC Ribeiro, Claudio J Margulis, and Edward W Castner Jr. Structure of cyano-anion ionic liquids: X-ray scattering and simulations. *The Journal of chemical physics*, 145(2):024503, 2016.

[39] Patrícia SB dos Santos, Xabier Erdocia, Darci A Gatto, and Jalel Labidi. Characterisation of kraft lignin separated by gradient acid precipitation. *Industrial crops and products*, 55:149–154, 2014.

[40] James WE Drewitt, Sandro Jahn, Viviana Cristiglio, Aleksei Bytchkov, Marlene Leydier, Séverine Brassamin, Henry E Fischer, and Louis Hennet. The structure of liquid calcium aluminates as investigated using neutron and high energy x-ray diffraction in combination with molecular dynamics simulation methods. *Journal of Physics: Condensed Matter*, 23(15):155101, 2011.

[41] Jincheng Du and L René Corrales. Understanding lanthanum aluminate glass structure by correlating molecular dynamics simulation results with neutron and x-ray scattering data. *Journal of non-crystalline solids*, 353(2):210–214, 2007.

[42] Jincheng Du, Chris J Benmore, Rene Corrales, Robert T Hart, and JK Richard Weber. A molecular dynamics simulation interpretation of neutron and x-ray diffraction measurements on single phase $Y_2O_3--Al_2O_3$ glasses. *Journal of Physics: Condensed Matter*, 21(20):205102, 2009.

[43] Takeshi Egami and Simon JL Billinge. *Underneath the Bragg peaks: Structural analysis of complex materials*. Elsevier, 2003.

[44] Jon H Eggert, Gunnar Weck, Paul Loubeyre, and Mohamed Mezouar. Quantitative structure factor and density measurements of high-pressure fluids in diamond anvil cells by x-ray diffraction: Argon and water. *Physical Review B*, 65(17):174105, 2002.

[45] CL Farrow, P Juhas, JW Liu, D Bryndin, ES Božin, J Bloch, Th Proffen, and SJL Billinge. PDFfit2 and PDFgui: Computer programs for studying nanostructure in crystals. *Journal of Physics: Condensed Matter*, 19(33):335219, 2007.

[46] D Ferdous, AK Dalai, SK Bej, and RW Thring. Pyrolysis of lignins: Experimental and kinetics studies. *Energy & Fuels*, 16(6):1405–1412, 2002.

[47] Javier Fernández-Rodríguez, Xabier Erdocia, Fabio Hernández-Ramos, María González Alriols, and Jalel Labidi. Lignin separation and fractionation by ultrafiltration. In *Separation of Functional Molecules in Food by Membrane Technology*, pages 229–265. Elsevier, 2019.

[48] Andrea C Ferrari and Denis M Basko. Raman spectroscopy as a versatile tool for studying the properties of graphene. *Nature nanotechnology*, 8(4):235–246, 2013.

[49] Geoffroy Ferru, Donatien Gomes Rodrigues, Laurence Berthon, Olivier Diat, Pierre Bauduin, and Philippe Guilbaud. Elucidation of the structure of organic solutions in solvent extraction by combining molecular dynamics and x-ray scattering. *Angewandte Chemie International Edition*, 53(21):5346–5350, 2014.

[50] Hidemine Furuya, M Mondello, Hyung-Jin Yang, Ryong-Joon Roe, RW Erwin, CC Han, and SD Smith. Molecular dynamics simulation of atactic polystyrene. 2. Comparison with neutron scattering data. *Macromolecules*, 27(20):5674–5680, 1994.

[51] Nidia C Gallego, Cristian I Contescu, Harry M Meyer III, Jane Y Howe, Roberta A Meisner, E Andrew Payzant, Michael J Lance, Sang Y Yoon, Matthew Denlinger, and David L Wood III. Advanced surface and microstructural characterization of natural graphite anodes for lithium ion batteries. *Carbon*, 72:393–401, 2014.

[52] Valerie García-Negrón. Processing-property-structure relationships of carbonaceous materials derived from renewable lignin products. *Master's Thesis, University of Tennessee*, 2017.

[53] Valerie García-Negrón, Nathan D Phillip, Jianlin Li, Claus Daniel, David Wood, David J Keffer, Orlando Rios, and David P Harper. Processing–structure–property relationships for lignin-based carbonaceous materials used in energy-storage applications. *Energy Technology*, 5(8):1311–1321, 2017.

[54] Valerie García-Negrón, Akinola D Oyedele, Eduardo Ponce, Orlando Rios, David P Harper, and David J Keffer. Evaluation of nano-and mesoscale structural features in composite materials through hierarchical decomposition of the radial distribution function. *Journal of Applied Crystallography*, 51(1):76–86, 2018.

[55] Valerie García-Negrón, Dayton G Kizzire, Orlando Rios, David J Keffer, and David P Harper. Elucidating nano and meso-structures of lignin carbon composites: A comprehensive study of feedstock and temperature dependence. *Carbon*, 161:856–869, 2020.

[56] MA Gardner, John C Dore, AN North, D Cazorla-Amoros, C Salinas-Martinez de Lecea, and M-C Bellissent-Funel. Structural studies of microporous carbons by neutron diffraction. *Carbon*, 34(7):857–860, 1996.

[57] Paul Geladi and Bruce R Kowalski. Partial least-squares regression: A tutorial. *Analytica chimica acta*, 185:1–17, 1986.

[58] Sébastien Gillet, Mario Aguedo, Laurène Petitjean, ARC Morais, AM da Costa Lopes, RM Łukasik, and PT Anastas. Lignin transformations for high value applications: Towards targeted modifications using green chemistry. *Green Chemistry*, 19(18):4200–4233, 2017.

[59] Paola Giudicianni, Giuseppe Cardone, and Raffaele Ragucci. Cellulose, hemicellulose and lignin slow steam pyrolysis: Thermal decomposition of biomass components mixtures. *Journal of Analytical and Applied Pyrolysis*, 100:213–222, 2013.

[60] Wolfgang G Glasser. About making lignin great again-some lessons from the past. *Frontiers in chemistry*, 7:565, 2019.

[61] Azadeh Goudarzi, Li-Ting Lin, and Frank K Ko. X-ray diffraction analysis of kraft lignins and lignin-derived carbon nanofibers. *Journal of Nanotechnology in Engineering and Medicine*, 5(2), 2014.

[62] Yadhu N Guragain, Alvaro I Herrera, Praveen V Vadlani, and Om Prakash. Lignins of bioenergy crops: A review. *Natural product communications*, 10(1): 1934578X1501000141, 2015.

[63] Gonzalo Gutierrez and Börje Johansson. Molecular dynamics study of structural properties of amorphous Al_2O_3. *Physical Review B*, 65(10):104202, 2002.

[64] Robert Hayes, Silvia Imberti, Gregory G Warr, and Rob Atkin. Amphiphilicity determines nanostructure in protic ionic liquids. *Physical Chemistry Chemical Physics*, 13(8):3237–3247, 2011.

[65] Cyril Heitner, Don Dimmel, and John Schmidt. *Lignin and lignans: Advances in chemistry*. CRC press, 2016.

[66] Servann Herou, Maria Crespo Ribadeneyra, Rajesh Madhu, Vicente Araullo-Peters, Anders Jensen, Philipp Schlee, and Magdalena Titirici. Ordered mesoporous carbons from lignin: a new class of biobased electrodes for supercapacitors. *Green chemistry*, 21(3):550–559, 2019.

[67] Nancy J Hess, Gregory K Schenter, Michael R Hartman, Luc L Daemen, Thomas Proffen, Shawn M Kathmann, Christopher J Mundy, Monika Hartl, David J Heldebrant, Ashley C Stowe, et al. Neutron powder diffraction and molecular simulation study of the structural evolution of ammonia borane from 15 to 340 K. *The Journal of Physical Chemistry A*, 113(19):5723–5735, 2009.

[68] HL Hintz and SA Lawal. Pulping and bleaching. *Reference Module in Materials Science and Materials Engineering*, 2018.

[69] Omid Hosseinaei, David P Harper, Joseph J Bozell, and Timothy G Rials. Role of physicochemical structure of organosolv hardwood and herbaceous lignins on carbon fiber performance. *ACS Sustainable Chemistry & Engineering*, 4(10):5785–5798, 2016.

[70] Omid Hosseinaei, David Harper, Joseph Bozell, and Timothy Rials. Improving processing and performance of pure lignin carbon fibers through hardwood and herbaceous lignin blends. *International journal of molecular sciences*, 18(7):1410, 2017.

[71] Yong Huang, Yijing Duan, Shi Qiu, Meng Wang, Chao Ju, Hui Cao, Yunming Fang, and Tianwei Tan. Lignin-first biorefinery: a reusable catalyst for lignin depolymerization and application of lignin oil to jet fuel aromatics and polyurethane feedstock. *Sustainable Energy & Fuels*, 2(3):637–647, 2018.

[72] Greg Hura, Daniela Russo, Robert M Glaeser, Teresa Head-Gordon, Matthias Krack, and Michele Parrinello. Water structure as a function of temperature from x-ray scattering experiments and ab initio molecular dynamics. *Physical Chemistry Chemical Physics*, 5(10):1981–1991, 2003.

[73] Jan Ilavsky. Nika: software for two-dimensional data reduction. *Journal of Applied Crystallography*, 45(2):324–328, 2012.

[74] Jan Ilavsky and Peter R Jemian. Irena: Tool suite for modeling and analysis of small-angle scattering. *Journal of Applied Crystallography*, 42(2):347–353, 2009.

[75] Kengo Ishimaru, Toshimitsu Hata, Paul Bronsveld, Takashi Nishizawa, and Yuji Imamura. Characterization of sp^2-and sp^3-bonded carbon in wood charcoal. *Journal of wood science*, 53(5):442–448, 2007.

[76] David A Jacques and Jill Trewhella. Small-angle scattering for structural biology—Expanding the frontier while avoiding the pitfalls. *Protein science*, 19(4): 642–657, 2010.

[77] Charl J Jafta, Albrecht Petzold, Sebastian Risse, Daniel Clemens, Dirk Wallacher, Günter Goerigk, and Matthias Ballauff. Correlating pore size and shape to local disorder in microporous carbon: a combined small angle neutron and x-ray scattering study. *Carbon*, 123:440–447, 2017.

[78] Farideh Jalilehvand, Daniel Spångberg, Patric Lindqvist-Reis, Kersti Hermansson, Ingmar Persson, and Magnus Sandström. Hydration of the calcium ion. An EXAFS, large-angle x-ray scattering, and molecular dynamics simulation study. *Journal of the American Chemical Society*, 123(3):431–441, 2001.

[79] Ju-Won Jeon, Libing Zhang, Jodie L Lutkenhaus, Dhrubojyoti D Laskar, John P Lemmon, Daiwon Choi, Manjula I Nandasiri, Ali Hashmi, Jie Xu, Radha K Motkuri, et al. Controlling porosity in lignin-derived nanoporous carbon for supercapacitor applications. *ChemSusChem*, 8(3):428–432, 2015.

[80] Bo Jiang, Tor Grande, and Sverre M Selbach. Local structure of disordered $Bi_{0\cdot 5}K_{0\cdot 5}TiO_3$ investigated by pair distribution function analysis and first-principles calculations. *Chemistry of Materials*, 29(10):4244–4252, 2017.

[81] Guozhan Jiang, Daniel J Nowakowski, and Anthony V Bridgwater. A systematic study of the kinetics of lignin pyrolysis. *Thermochimica Acta*, 498(1-2):61–66, 2010.

[82] Ian T Jolliffe. Graphical representation of data using principal components. *Principal component analysis*, pages 78–110, 2002.

[83] Karolina Jurkiewicz, Łukasz Hawełek, Katarzyna Balin, Jacek Szade, Flavia L Braghiroli, Vanessa Fierro, Alain Celzard, and Andrzej Burian. Conversion of natural tannin to hydrothermal and graphene-like carbons studied by wide-angle x-ray scattering. *The Journal of Physical Chemistry A*, 119(32):8692–8701, 2015.

[84] Armin Eraghi Kazzaz and Pedram Fatehi. Technical lignin and its potential modification routes: A mini-review. *Industrial Crops and Products*, 154:112732, 2020.

[85] Marlene Kienberger. Potential applications of lignin. In *Economics of Bioresources*, pages 183–193. Springer, 2019.

[86] Marjatta Kleen, Gunnar Lindblad, and Stefan Backa. Quantification of lignin and carbohydrates in kraft pulps using analytical pyrolysis and multivariate data analysis. *Journal of analytical and applied pyrolysis*, 25:209–227, 1993.

[87] Mike Kleinert and Tanja Barth. Towards a lignincellulosic biorefinery: direct one-step conversion of lignin to hydrogen-enriched biofuel. *Energy & Fuels*, 22(2):1371–1379, 2008.

[88] Victor Krayzman and Igor Levin. Reverse monte carlo refinements of nanoscale atomic correlations using powder and single-crystal diffraction data. *Journal of Applied Crystallography*, 45(1):106–112, 2012.

[89] Norbert Kucerka, Bryan W Holland, Chris G Gray, Bruno Tomberli, and John Katsaras. Scattering density profile model of POPG bilayers as determined by molecular dynamics simulations and small-angle neutron and x-ray scattering experiments. *The Journal of Physical Chemistry B*, 116(1):232–239, 2011.

[90] Adarsh Kumar, Anushree Anushree, Jitendra Kumar, and Thallada Bhaskar. Utilization of lignin: A sustainable and eco-friendly approach. *Journal of the Energy Institute*, 2019.

[91] RV Kurahatti, AO Surendranathan, SA Kori, Nirbhay Singh, AV Ramesh Kumar, and Saurabh Srivastava. Defence applications of polymer nanocomposites. *Defence Science Journal*, 60(5):551–563, 2010.

[92] Rosemary K Le, Bradley J Harris, Ifeyinwa J Iwuchukwu, Barry D Bruce, Xiaolin Cheng, Shuo Qian, William T Heller, Hugh O'Neill, and Paul D Frymier. Analysis of the solution structure of Thermosynechococcus elongatus photosystem i in n-dodecyl-β-d-maltoside using small-angle neutron scattering and molecular dynamics simulation. *Archives of biochemistry and biophysics*, 550:50–57, 2014.

[93] J-M Leyssale, J-P Da Costa, Christian Germain, Patrick Weisbecker, and GL Vignoles. Structural features of pyrocarbon atomistic models constructed from transmission electron microscopy images. *Carbon*, 50(12):4388–4400, 2012.

[94] Changzhi Li, Xiaochen Zhao, Aiqin Wang, George W Huber, and Tao Zhang. Catalytic transformation of lignin for the production of chemicals and fuels. *Chemical reviews*, 115(21):11559–11624, 2015.

[95] Chen Li. Value added products from lignin and biomass derivatives. *Doctor of Philosophy (PhD), Dissertation, Civil/Environmental Engineering, Old Dominion University*, 2018. doi: 10.25777/84gn-0y65.

[96] Tao Li, Andrew J Senesi, and Byeongdu Lee. Small angle x-ray scattering for nanoparticle research. *Chemical reviews*, 116(18):11128–11180, 2016.

[97] Stephen Y Lin and Carlton W Dence. *Methods in lignin chemistry*. Springer Science & Business Media, 2012.

[98] Yan-Jia Liou and Wu-Jang Huang. Quantitative analysis of graphene sheet content in wood char powders during catalytic pyrolysis. *Journal of Materials Science & Technology*, 29(5):406–410, 2013.

[99] Ana Lourenço and Helena Pereira. Compositional variability of lignin in biomass. *Lignin - Trends and applications. InTech*, pages 65–98, 2018.

[100] Hodásová L'udmila, Jablonskỳ Michal, Škulcová Andrea, and Ház Aleš. Lignin, potential products and their market value. *Wood Research*, 60(6):973–986, 2015.

[101] Vickie E Lynch, Jose M Borreguero, Debsindhu Bhowmik, Panchapakesan Ganesh, Bobby G Sumpter, Thomas E Proffen, and Monojoy Goswami. An automated analysis workflow for optimization of force-field parameters using neutron scattering data. *Journal of Computational Physics*, 340:128–137, 2017.

[102] Nicholas W McNutt, Orlando Rios, Mikhail Feygenson, Thomas E Proffen, and David J Keffer. Structural analysis of lignin-derived carbon composite anodes. *Journal of Applied Crystallography*, 47(5):1577–1584, 2014.

[103] Nicholas W McNutt, Qifei Wang, Orlando Rios, and David J Keffer. Entropy-driven structure and dynamics in carbon nanocrystallites. *Journal of Nanoparticle Research*, 16(4):2365, 2014.

[104] Nicholas W McNutt, Marshall McDonnell, Orlando Rios, and David J Keffer. Li-ion localization and energetics as a function of anode structure. *ACS applied materials & interfaces*, 9(8):6988–7002, 2017.

[105] Nicholas W McNutt, Orlando Rios, Vasileios Maroulas, and David J Keffer. Interfacial li-ion localization in hierarchical carbon anodes. *Carbon*, 111:828–834, 2017.

[106] DA McQuarrie. Statistical mechanics university science books. *Sausalito, CA*, 2000.

[107] Nathan Meek, Dayakar Penumadu, Omid Hosseinaei, David Harper, Stephen Young, and Timothy Rials. Synthesis and characterization of lignin carbon fiber and composites. *Composites Science and Technology*, 137:60–68, 2016.

[108] Tünde Megyes, Imre Bakó, Tamás Radnai, Tamás Grósz, Kersti Hermansson, Michael Probst, et al. X-ray and neutron diffraction studies and molecular dynamics simulations of liquid DMSO. *Physical Chemistry Chemical Physics*, 6(9):2136–2144, 2004.

[109] Daniel Montané, Vanessa Torné-Fernández, and Vanessa Fierro. Activated carbons from lignin: Kinetic modeling of the pyrolysis of kraft lignin activated with phosphoric acid. *Chemical Engineering Journal*, 106(1):1–12, 2005.

[110] Yusuke Morikawa, Shin-ichi Nishimura, Ryu-ichi Hashimoto, Masato Ohnuma, and Atsuo Yamada. Mechanism of sodium storage in hard carbon: An x-ray scattering analysis. *Advanced Energy Materials*, 10(3):1903176, 2020.

[111] Adriana M Navarro-Suárez, Javier Carretero-González, Vladimir Roddatis, Eider Goikolea, Julie Ségalini, Edurne Redondo, Teófilo Rojo, and Roman Mysyk. Nanoporous carbons from natural lignin: study of structural–textural properties and application to organic-based supercapacitors. *RSC Advances*, 4(89):48336–48343, 2014.

[112] Reinhard B Neder and Vladimir I Korsunskiy. Structure of nanoparticles from powder diffraction data using the pair distribution function. *Journal of Physics: Condensed Matter*, 17(5):S125, 2005.

[113] Reinhard B Neder and Thomas Proffen. *Diffuse Scattering and Defect Structure Simulations: A cook book using the program DISCUS*, volume 11. Oxford University Press, 2008.

[114] M Ben Ohoud, F Obrecht, L Gatineua, P Levitz, and H Van Damme. Surface area, mass fractal dimension, and apparent density of powders. *Journal of colloid and interface science*, 124(1):156–161, 1988.

[115] Daniel Olds, H-W Wang, and Katharine Page. DShaper: An approach for handling missing low-Q data in pair distribution function analysis of nanostructured systems. *Journal of Applied Crystallography*, 48(6):1651–1659, 2015.

[116] MH Oliveira Jr, PF Barbieri, IL Torriani, and FC Marques. Saxs analysis of graphitic amorphous carbon. *Thin Solid Films*, 516(2-4):316–319, 2007.

[117] Akinola Oyedele, Nicholas W Mcnutt, Orlando Rios, and David J Keffer. Hierarchical model for the analysis of scattering data of complex materials. *JOM*, 68 (6):1583–1588, 2016.

[118] Katharine Page, Thomas Proffen, Humberto Terrones, Mauricio Terrones, Lily Lee, Yan Yang, Susanne Stemmer, Ram Seshadri, and Anthony K Cheetham. Direct observation of the structure of gold nanoparticles by total scattering powder neutron diffraction. *Chemical physics letters*, 393(4-6):385–388, 2004.

[119] Katharine Page, Matthew W Stoltzfus, Young-Il Kim, Thomas Proffen, Patrick M Woodward, Anthony K Cheetham, and Ram Seshadri. Local atomic ordering in $BaTaO_2N$ studied by neutron pair distribution function analysis and density functional theory. *Chemistry of materials*, 19(16):4037–4042, 2007.

[120] Katharine Page, Taylor C Hood, Th Proffen, and Reinhard B Neder. Building and refining complete nanoparticle structures with total scattering data. *Journal of Applied Crystallography*, 44(2):327–336, 2011.

[121] Hyunchul Park, Minho Kim, Fan Xu, Cheolsoo Jung, Soon Man Hong, and Chong Min Koo. In situ synchrotron wide-angle x-ray scattering study on rapid lithiation of graphite anode via direct contact method for li-ion capacitors. *Journal of Power Sources*, 283:68–73, 2015.

[122] Eric Pefoute, Ludovic Martin-Gondre, Jacques Ollivier, Jean-Christophe Soetens, Margarita Russina, and Arnaud Desmedt. Modeling the THF clathrate hydrate dynamics by combining molecular dynamics and quasi-elastic neutron scattering. *Chemical Physics*, 496:24–34, 2017.

[123] Joaquín Peralta, Gonzalo Gutiérrez, and José Rogan. Structural and vibrational properties of amorphous GeO_2: A molecular dynamics study. *Journal of Physics: Condensed Matter*, 20(14):145215, 2008.

[124] R Perret and W Ruland. X-ray small-angle scattering of non-graphitizable carbons. *Journal of Applied Crystallography*, 1(5):308–313, 1968.

[125] Joseph Peterson, James TenCate, Th Proffen, Timothy Darling, Heinz Nakotte, and Katharine Page. Quantifying amorphous and crystalline phase content with the atomic pair distribution function. *Journal of Applied Crystallography*, 46(2):332–336, 2013.

[126] V Petkov, Y Ren, S Kabekkodu, and D Murphy. Atomic pair distribution functions analysis of disordered low-Z materials. *Physical Chemistry Chemical Physics*, 15 (22):8544–8554, 2013.

[127] Valeri Petkov. Pair distribution functions analysis. *Characterization of Materials*, pages 1–14, 2002.

[128] Loukas Petridis, Sai Venkatesh Pingali, Volker Urban, William T Heller, Hugh M O'Neill, Marcus Foston, Arthur Ragauskas, and Jeremy C Smith. Self-similar

multiscale structure of lignin revealed by neutron scattering and molecular dynamics simulation. *Physical Review E*, 83(6):061911, 2011.

[129] Albrecht Petzold, Anika Juhl, Jonas Scholz, Boris Ufer, Günter Goerigk, Michael Fröba, Matthias Ballauff, and Simone Mascotto. Distribution of sulfur in carbon/sulfur nanocomposites analyzed by small-angle x-ray scattering. *Langmuir*, 32(11):2780–2786, 2016.

[130] Andraž Polak, Mounir Tarek, Matija Tomšič, Janez Valant, Nataša Poklar Ulrih, Andrej Jamnik, Peter Kramar, and Damijan Miklavčič. Structural properties of archaeal lipid bilayers: Small-angle x-ray scattering and molecular dynamics simulation study. *Langmuir*, 30(28):8308–8315, 2014.

[131] Igor Pro. 6; wavemetrics inc. *Lake Oswego, Oregon, USA*, 2011.

[132] Th Proffen. Neutron total scattering analysis of nanoparticles. *JOM*, 64(1):112–116, 2012.

[133] Th Proffen and SJL Billinge. PDFFIT, a program for full profile structural refinement of the atomic pair distribution function. *Journal of Applied Crystallography*, 32(3): 572–575, 1999.

[134] Th Proffen, SJL Billinge, T Egami, and D Louca. Structural analysis of complex materials using the atomic pair distribution function—a practical guide. *Zeitschrift für Kristallographie-Crystalline Materials*, 218(2):132–143, 2003.

[135] Thomas Proffen and RB Neder. DISCUS: A program for diffuse scattering and defect-structure simulation. *Journal of applied crystallography*, 30(2):171–175, 1997.

[136] Thomas Proffen, Katharine L Page, Sylvia E McLain, Bjorn Clausen, Timothy W Darling, James A TenCate, Seung-Yub Lee, and Ersan Ustundag. Atomic pair distribution function analysis of materials containing crystalline and amorphous phases. *Zeitschrift für Kristallographie-Crystalline Materials*, 220(12):1002–1008, 2005.

[137] Hengfei Qin, Shifei Kang, Yongkui Huang, Siyu Liu, Yao Fang, Xi Li, and Yangang Wang. Lignin based synthesis of carbon nanocages assembled from graphitic layers with hierarchical pore structure. *Materials Letters*, 159:463–465, 2015.

[138] Xiangyun Qiu, Jeroen W Thompson, and Simon JL Billinge. PDFgetX2: A GUI-driven program to obtain the pair distribution function from x-ray powder diffraction data. *Journal of Applied Crystallography*, 37(4):678–678, 2004.

[139] John Ralph, Knut Lundquist, Gösta Brunow, Fachuang Lu, Hoon Kim, Paul F Schatz, Jane M Marita, Ronald D Hatfield, Sally A Ralph, Jørgen Holst Christensen, et al. Lignins: Natural polymers from oxidative coupling of 4-hydroxyphenyl-propanoids. *Phytochemistry Reviews*, 3(1-2):29–60, 2004.

[140] S Román, JF González, CM González-García, and F Zamora. Control of pore development during CO_2 and steam activation of olive stones. *Fuel Processing Technology*, 89(8):715–720, 2008.

[141] Roger M Rowell. *Handbook of wood chemistry and wood composites*. CRC press, 2012.

[142] Wilhelm Ruland and Bernd Smarsly. X-ray scattering of non-graphitic carbon: an improved method of evaluation. *Journal of applied crystallography*, 35(5):624–633, 2002.

[143] David W Rutherford, Robert L Wershaw, Colleen E Rostad, and Charlene N Kelly. Effect of formation conditions on biochars: Compositional and structural properties of cellulose, lignin, and pine biochars. *Biomass and Bioenergy*, 46:693–701, 2012.

[144] William J Sagues, Ankush Jain, Dylan Brown, Salonika Aggarwal, Antonio Suarez, Matthew Kollman, Seonghyun Park, and Dimitris S Argyropoulos. Are lignin-derived carbon fibers graphitic enough? *Green Chemistry*, 21(16):4253–4265, 2019.

[145] B Sahouli, S Blacher, F Brouers, R Sobry, G Van den Bossche, H Darmstadt, and C Roy. Saxs characterization of pyrolytic carbon blacks. In *MATERIALS RESEARCH SOCIETY SYMPOSIUM PROCEEDINGS*, volume 407, pages 39–44. Materials Research Society, 1996.

[146] Vasudev P Saraf, Wolfgang G Glasser, Garth L Wilkes, and James E McGrath. Engineering plastics from lignin. vi. structure–property relationships of peg-containing polyurethane networks. *Journal of applied polymer science*, 30(5):2207–2224, 1985.

[147] Damien Saurel, Julie Segalini, María Jauregui, Afshin Pendashteh, Barbara Daffos, Patrice Simon, and Montse Casas-Cabanas. A saxs outlook on disordered

carbonaceous materials for electrochemical energy storage. *Energy Storage Materials*, 21:162–173, 2019.

[148] Friederike Saxe, Michaela Eder, Gunthard Benecke, Barbara Aichmayer, Peter Fratzl, Ingo Burgert, and Markus Rüggeberg. Measuring the distribution of cellulose microfibril angles in primary cell walls by small angle x-ray scattering. *Plant Methods*, 10(1):1–8, 2014.

[149] Heimo Schnablegger and Yashveer Singh. The SAXS guide: getting acquainted with the principles. *Austria: Anton Paar GmbH*, pages 1–124, 2011.

[150] Marco Sette, Heiko Lange, and Claudia Crestini. Quantitative HSQC analyses of lignin: A practical comparison. *Computational and structural biotechnology journal*, 6(7):e201303016, 2013.

[151] Lawrie B Skinner, Congcong Huang, Daniel Schlesinger, Lars GM Pettersson, Anders Nilsson, and Chris J Benmore. Benchmark oxygen-oxygen pair-distribution function of ambient water from x-ray diffraction measurements with a wide Q-range. *The Journal of chemical physics*, 138(7):074506, 2013.

[152] Michael R Snowdon, Amar K Mohanty, and Manjusri Misra. A study of carbonized lignin as an alternative to carbon black. *ACS Sustainable Chemistry & Engineering*, 2(5):1257–1263, 2014.

[153] CM Sorensen and GM Wang. Size distribution effect on the power law regime of the structure factor of fractal aggregates. *Physical Review E*, 60(6):7143, 1999.

[154] Felipe Souto, Veronica Calado, and Nei Pereira Jr. Lignin-based carbon fiber: A current overview. *Materials Research Express*, 5(7):072001, 2018.

[155] Aneta Szczygielska, A Jabłońska, Andrzej Burian, John C Dore, V Honikimaki, and JB Nagy. Radial distribution function analysis of carbon nanotubes. *Acta Physica Polonica A*, 98(5):611–617, 2000.

[156] Elena Ten and Wilfred Vermerris. Recent developments in polymers derived from industrial lignin. *Journal of Applied Polymer Science*, 132(24), 2015.

[157] Wyatt E Tenhaeff, Orlando Rios, Karren More, and Michael A McGuire. Highly robust lithium ion battery anodes from lignin: An abundant, renewable, and low-cost material. *Advanced Functional Materials*, 24(1):86–94, 2014.

[158] Amélie Tribot, Ghenima Amer, Maarouf Abdou Alio, Hélène de Baynast, Cédric Delattre, Agnès Pons, Jean-Denis Mathias, Jean-Marc Callois, Christophe Vial, Philippe Michaud, et al. Wood-lignin: Supply, extraction processes and use as bio-based material. *European Polymer Journal*, 2019.

[159] Matthew G Tucker, Martin T Dove, and David A Keen. Application of the reverse monte carlo method to crystalline materials. *Journal of applied crystallography*, 34 (5):630–638, 2001.

[160] Matthew G Tucker, David A Keen, Martin T Dove, Andrew L Goodwin, and Qun Hui. RMCProfile: Reverse monte carlo for polycrystalline materials. *Journal of Physics: Condensed Matter*, 19(33):335218, 2007.

[161] Ulla Vainio, Natalia Maximova, Bo Hortling, Janne Laine, Per Stenius, Liisa Kaarina Simola, Janis Gravitis, and Ritva Serimaa. Morphology of dry lignins and size and shape of dissolved kraft lignin particles by x-ray scattering. *Langmuir*, 20(22):9736–9744, 2004.

[162] HG Van Oss. Us geological survey, mineral commodity summaries, january 2013, 2013.

[163] M Beatriz Vázquez-Santos, Amelia Martínez-Alonso, Juan MD Tascón, Jean-Noël Rouzaud, Erik Geissler, and Krisztina László. Complementary x-ray scattering and high resolution imaging of nanostructure development in thermally treated PBO fibers. *Carbon*, 49(9):2960–2970, 2011.

[164] Singaravelu Vivekanandhan, Manjusri Misra, and Amar Kumar Mohanty. Microscopic, structural, and electrical characterization of the carbonaceous materials synthesized from various lignin feedstocks. *Journal of Applied Polymer Science*, 132 (15), 2015.

[165] Michael E Wall, Andrew H Van Benschoten, Nicholas K Sauter, Paul D Adams, James S Fraser, and Thomas C Terwilliger. Conformational dynamics of a crystalline protein from microsecond-scale molecular dynamics simulations and diffuse x-ray scattering. *Proceedings of the National Academy of Sciences*, 111(50):17887–17892, 2014.

[166] Dereca Watkins, Md Nuruddin, Mahesh Hosur, Alfred Tcherbi-Narteh, and Shaik Jeelani. Extraction and characterization of lignin from different biomass resources. *Journal of Materials Research and Technology*, 4(1):26–32, 2015.

[167] Patrick Weisbecker, Jean-Marc Leyssale, Henry E Fischer, Veijo Honkimäki, Maëva Lalanne, and Gérard L Vignoles. Microstructure of pyrocarbons from pair distribution function analysis using neutron diffraction. *Carbon*, 50(4):1563–1573, 2012.

[168] Hanne Wikberg, Taina Ohra-aho, Filoklis Pileidis, and Maria-Magdalena Titirici. Structural and morphological changes in kraft lignin during hydrothermal carbonization. *ACS Sustainable Chemistry & Engineering*, 3(11):2737–2745, 2015.

[169] Elena Willinger. Analysis of local structure by atomic pair distribution function, 2016. Lecture Series Winter Semester 2016/2017, Modern Methods in Heterogeneous Catalysis Research, Department of Inorganic Chemistry, Fritz Haber Institute. http://hdl.handle.net/11858/00-001M-0000-002D-CA0B-3, 2017.

[170] Chongling Yang, Huige Wei, Litao Guan, Jiang Guo, Yiran Wang, Xingru Yan, Xi Zhang, Suying Wei, and Zhanhu Guo. Polymer nanocomposites for energy storage, energy saving, and anticorrosion. *Journal of Materials Chemistry A*, 3(29): 14929–14941, 2015.

[171] Lin Yang. py4xs. https://github.com/NSLS-II-LIX/py4xs, 2020.

[172] Anita Zeidler, Kamil Wezka, Ruth F Rowlands, Dean AJ Whittaker, Philip S Salmon, Annalisa Polidori, James WE Drewitt, Stefan Klotz, Henry E Fischer, Martin C Wilding, et al. High-pressure transformation of SiO_2 glass from a tetrahedral to an octahedral network: A joint approach using neutron diffraction and molecular dynamics. *Physical review letters*, 113(13):135501, 2014.

[173] Bo Zhang, Hua-Jiang Huang, and Shri Ramaswamy. Reaction kinetics of the hydrothermal treatment of lignin. In *Biotechnology for Fuels and Chemicals*, pages 487–499. Springer, 2007.

[174] Xiaodong Zhang, Min Xu, Rongfeng Sun, and Li Sun. Study on biomass pyrolysis kinetics. *Journal of engineering for gas turbines and power*, 128(3):493–496, 2006.

[175] Ping Zhou, Peter Papanek, Roland Lee, John E Fischer, and William A Kamitakahara. Local structure and vibrational spectroscopy of disordered carbons for Li batteries: Neutron scattering studies. *Journal of The Electrochemical Society*, 144(5):1744–1750, 1997.

APPENDICES

APPENDIX A

SUPPLEMENTARY DATA FOR CHAPTER 2

A.1 Derivation of the radial distribution function (RDF) between two parallel discs

The derivation of the model for the mesoscale RDF components can be found at https://doi.org/10.1107/S1600576717016843/po5109sup1.pdf

A.2 Code to Evaluate Disc-Disc RDF

A.2.1 Driver

```
%
%  gofr_discdisc_test.m
%
%  This script calls gofr_discdisc.m
%
% use:
% g = gofr_discdisc_test
%
%
%  authors: David J. Keffer & Akinola D. Oyedele
%  Dept. of Materials Science & Engineering
%  University of Tennessee
%  dkeffer@utk.edu
%  last updated:  June 1, 2017
%
clear all;
close all;
format long;
%
%  discretize radial dimension
```

```
%
rmin = 0.0;
rmax = 50.0;
dr = 0.01;
rvec = [rmin:dr:rmax];
nr = length(rvec);
%
%  test system parameters
%
%  rp1 must be less than or equal to rp2
rp1 = 7.0;
rp2 = 10.0;
dp = 3.4;
%
%  compute RDF
%
g = zeros(nr,1);
g = gofr_discdisc(dp,rp1,rp2,nr,rvec);
%
%  plot RDF
%
%
%  plot RDF
%
figure(1);
plot(rvec,g,'r-');
xlabel(' separation');
ylabel(' radial distribution function ');
%
%  check volume
%
vol1 = pi*rp1^2;
vol2 = pi*rp2^2;
volprod = vol1*vol2;
%
```

```
integral = 0.0;
cumulative = zeros(nr,1);
for i = 2:1:nr
base = rvec(i) - rvec(i-1);
height1 = 4.0*pi*rvec(i-1)^2*g(i-1);
height2 = 4.0*pi*rvec(i)^2*g(i);
area = 0.5*base*(height1 + height2);
cumulative(i) = cumulative(i-1) + area;
integral = integral + area;
end
%
%  plot cumulative RDF
%
figure(2);
plot(rvec,cumulative,'k-');
xlabel(' separation');
ylabel(' cumulative distribution function ');
%
%  error checking
%
diff = (integral - volprod)/volprod;
fprintf(1, ' analytical %e numerical %e error %e \n',volprod
   ,integral,diff);
```

A.2.2 Functions

```
function g = gofr_discdisc(dp,rp1,rp2,nr,rvec)
%
%  gofr_discdisc
%
%  This code calculates the contribution to the radial
   distribution function
%  due to the atoms distributed uniformly over two discs of
   radius rp1 and rp2
%  and separated by a distance p.
%
```

```
%  The RDF is returned in units of area squared.
%  The RDF IS normalized by a factor of 1.0/(4.0*pi*r^2).
%  The value of rp1 must be less than or equal to rp2.
%
% use:
% g = gofr_discdisc(dp,rp1,rp2,nr,rvec)
%
% inputs:
% dp:  distance between particles
% rp1:  radius of particle 1
% rp2:  radius of particle 2
% nr:  number of radial points to evaluate function
% rvec:  vector of radial positions
%
% outputs:
% g:  radial distribution function
%
%  authors: David J. Keffer & Akinola D. Oyedele
%  Dept. of Materials Science & Engineering
%  University of Tennessee
%  dkeffer@utk.edu
%  last updated:  June 1, 2017
%
% input parameters
%
fvec = zeros(nr,1); % d/dr
g = zeros(nr,1); % Radial distribution function

for i = 1:1:nr
    r = rvec(i);

    if (r <= dp)  %  no contribution until r is bigger than
       dp
        fvec(i) = 0;
```

```
else
    rx =  sqrt( r*r - dp*dp);
    drxdr = r/rx;
    rp1min_cond = rx-rp2;
    rp1min = abs(rp1min_cond);
    rp1max = min(rp2+rx,rp1);
    test = rp2*rp2+rx*rx-rp1min*rp1min;
    if test > 0
        result = pi/2.0;
    else
        result = -pi/2.0;
    end
    if rp1min_cond <= 0    % Encapsulated+overlap or only
        overlap
        if rp1min < rp1max   % Encapsulated plus overlap
            den = eqn_den(rp2,rx,rp1max);
            num = eqn_num(rp2,rx,rp1max);

            if rp1max == rp1
                drp1maxdr = 0;
            elseif rp1max == rp2 + rx
                drp1maxdr = drxdr;
            end
            %
            % Area of overlap  % Term 1
            f1_u = eqn_f1_u(rp2,rx,rp1max,drxdr,den,
               drp1maxdr);
            drp1mindr = (rp1min_cond/rp1min)*drxdr;
            dFdrx = -2*pi*rp2*rp2*rx*result;
            f1_l = dFdrx*drxdr;
            f1 = f1_u - f1_l;
            % Term 2
            f2_u = eqn_f2_u(rp2,rx,rp1max,drxdr,den,
               drp1maxdr);
            dFdrx = 2*pi*pi*rx*rp1min*rp1min;
```

```
            dFdrp1min = 2*pi*pi*rx*rx*rp1min;
            f2_l1 = dFdrx*drxdr + dFdrp1min*drp1mindr;
            dFdrx = -2*pi*rx*rp2*rp2*result;
            f2_l3 = dFdrx*drxdr;
            f2_l = f2_l1 + f2_l3;
            f2 = f2_u - f2_l;
            % Term 3
            f3 = eqn_f3(rp2,rx,rp1max,drxdr,num,drp1maxdr
               ,result);
            %
            area_overlap = f1 +f2 +f3;
            %
            % Area of encapsulated
            dFdrx = 2*pi*pi*rx*rp1min*rp1min;
            dFdrp1min = 2*pi*pi*rx*rx*rp1min;
            drp1mindr = (rx - rp2)/(abs(rx-rp2))*drxdr;
            area_small = dFdrx*drxdr + dFdrp1min*
               drp1mindr;
            % Area of overlap plus encapsulated
            fvec(i) = area_overlap +area_small;

        else    % Encapsulated only
            dFdrx = 2*pi*pi*rx*rp1*rp1;
            fvec(i) = dFdrx*drxdr;
        end

    else   % Encapsulates+overlap or only overlap
        if rp1min < rp1max   % Encapsulates plus overlap
            den = eqn_den(rp2,rx,rp1max);
            num = eqn_num(rp2,rx,rp1max);
            if rp1max == rp1
                drp1maxdr = 0;
            elseif rp1max == rp2 + rx
                drp1maxdr = drxdr;
            end
```

```
            %
            % Area that encapsulates % Term 1
            f1_u = eqn_f1_u(rp2,rx,rp1max,drxdr,den,
               drp1maxdr);
            drp1mindr = (rp1min_cond/rp1min)*drxdr;
            dFdrp1min = 2*pi*pi*rp2*rp2*rp1min;
            f1_l1 = dFdrp1min*drp1mindr;
            dFdrx = -2*pi*rp2*rp2*rx*result;
            f1_l3 = dFdrx*drxdr;
            f1_l = f1_l1 + f1_l3;
            f1 = f1_u - f1_l;
            % Term 2
            f2_u = eqn_f2_u(rp2,rx,rp1max,drxdr,den,
               drp1maxdr);
            dFdrx = -2*pi*rp2*rp2*rx*result;
            f2_l = dFdrx*drxdr;
            f2 = f2_u - f2_l;
            % Term 3
            f3 = eqn_f3(rp2,rx,rp1max,drxdr,num,drp1maxdr
               ,result);
            %
            % Area of overlap
            area_overlap = f1 +f2 +f3;
            %
            % Area of overlap plus area that encapsulates
            dFdrp1min = 2*pi*pi*rp2*rp2*rp1min;
            drp1mindr = (rx - rp2)/(abs(rx-rp2))*drxdr;
            area_large = dFdrp1min*drp1mindr;
            fvec(i) = area_overlap +area_large;

        else   % Encapsulates only
            fvec(i) = 0;
        end
    end
end
```

```
end

fac = 1.0/(4.0*pi);
for i = 2:1:nr
    fac2 = fac/(rvec(i)*rvec(i));
    g(i) = fac2*fvec(i);
end
end


function result = eqn_den(rp2,rx,rp1max)
result = (-rp2*rp2*rp2*rp2+2*rp2*rp2*(rx*rx+rp1max*rp1max)-(
   rx*rx-rp1max*rp1max)^2);
end


function result = eqn_num(rp2,rx,rp1max)
result =(rp2+rx-rp1max)*(rp2-rx+rp1max)*(-rp2+rx+rp1max)*(
   rp2+rx+rp1max);
end


function result = eqn_f1_u(rp2,rx,rp1max,drxdr,den,drp1maxdr
   )
dFdrx = 2*pi*rp2*rp2*rp1max*rp1max*rx/sqrt(den);
dFdrp1max_1 = 2*pi*rp2*rp2*rp1max*acos((rp2*rp2-rx*rx+rp1max
   *rp1max)/(2*rp2*rp1max));
dFdrp1max_2 = pi*rp2*rp2*rp1max*(rp2*rp2-rx*rx-rp1max*rp1max
   )/sqrt(den);
dFdrp1max = dFdrp1max_1 + dFdrp1max_2;
f1_u1 = dFdrx*drxdr + dFdrp1max*drp1maxdr;
%
dFdrx = -pi*rp2*rp2*rx*(rp2*rp2-rx*rx+rp1max*rp1max)/sqrt(
   den);
```

```
dFdrp1max = -pi*rp2*rp2*rp1max*(rp2*rp2+rx*rx-rp1max*rp1max)
   /sqrt(den);
f1_u2 = dFdrx*drxdr + dFdrp1max*drp1maxdr;
%
dFdrx_1 = -pi*rp2*rp2*rx*(-rp2*rp2+rx*rx+rp1max*rp1max)/sqrt
   (den);
dFdrx_2 = - 2*pi*rp2*rp2*rx*atan((rp2*rp2+rx*rx-rp1max*
   rp1max)/sqrt(den));
dFdrx = dFdrx_1 + dFdrx_2;
dFdrp1max = 2*pi*rp2*rp2*rx*rx*rp1max/sqrt(den);
f1_u3 = dFdrx*drxdr + dFdrp1max*drp1maxdr;
%
result =  f1_u1 + f1_u2 + f1_u3;
end


function result = eqn_f2_u(rp2,rx,rp1max,drxdr,den,drp1maxdr
   )
fac = 2*pi*rp1max*rx*acos((rx*rx-rp2*rp2+rp1max*rp1max)/(2*
   rx*rp1max));
dFdrx = rp1max*fac-(rp2*rp2+rx*rx-rp1max*rp1max)*pi*rp1max*
   rp1max*rx/sqrt(den);
dFdrp1max = rx*fac-(rp2*rp2-rx*rx+rp1max*rp1max)*pi*rp1max*
   rx*rx/sqrt(den);
f2_u1 = dFdrx*drxdr + dFdrp1max*drp1maxdr;
%
dFdrx = pi*rx*(rp2^4+rp1max^4+2*rx^4-3*rp1max^2*rx^2-2*rp2
   ^2*rp1max^2-3*rp2*rp2*rx*rx)/sqrt(den);
dFdrp1max = -pi*rp1max*rx*rx*(rp2*rp2+rx*rx-rp1max*rp1max)/
   sqrt(den);
f2_u2 = dFdrx*drxdr + dFdrp1max*drp1maxdr;
%
dFdrx_1 = -pi*rp2*rp2*rx*(-rp2*rp2+rx*rx+rp1max*rp1max)/sqrt
   (den);
```

```
dFdrx_2 = -2*pi*rp2*rp2*rx*atan((rp2*rp2+rx*rx-rp1max*rp1max
   )/sqrt(den));
dFdrx = dFdrx_1 + dFdrx_2;
dFdrp1max = 2*pi*rp2*rp2*rx*rx*rp1max/sqrt(den);
f2_u3 = dFdrx*drxdr + dFdrp1max*drp1maxdr;
%
result =  f2_u1 + f2_u2 + f2_u3;
end


function result = eqn_f3(rp2,rx,rp1max,drxdr,num,drp1maxdr,
   result)
% Term 3: Upper limit
dFdrx = (pi*rp2*rp2*rp1max*rp1max*rx + pi*rp2*rp2*rx*rx*rx
   +2*pi*(rp1max^2)*(rx^3) -pi*rx*rp1max^4-pi*(rx^5))/sqrt(
   num);
dFdrp1max = (pi*rp1max*(rp2^4) + pi*rp1max*(rx^4) +pi*(
   rp1max^5) -2*pi*(rp2^2)*(rp1max^3)-2*pi*(rx^2)*(rp1max^3)
   )/sqrt(num);
f3_u1 = dFdrx*drxdr + dFdrp1max*drp1maxdr;
dFdrx = pi*rp2*rp2*rx*(-rp2*rp2+rx*rx+rp1max*rp1max)/sqrt(
   num)+2*pi*rp2*rp2*rx*atan((rp2*rp2+rx*rx-rp1max*rp1max)/(
   sqrt(num)));
dFdrp1max = -2*pi*rp2*rp2*rx*rx*rp1max/sqrt(num);
f3_u2 = dFdrx*drxdr + dFdrp1max*drp1maxdr;
f3_u = f3_u1 + f3_u2;
% Term 3: Lower limit
dFdrx = 2*pi*rp2*rp2*rx*result;
f3_l2 = dFdrx*drxdr;
f3_l = f3_l2;
%
result = f3_u - f3_l;
end
```

A.3 Code to Evaluate Sphere-Sphere RDF

A.3.1 Driver

```
%
%  gofr_spheresphere_test.m
%
%  This script calls gofr_spheresphere.m
%
% use:
% g = gofr_spheresphere_test
%
%
%  authors: David J. Keffer & Akinola D. Oyedele
%  Dept. of Materials Science & Engineering
%  University of Tennessee
%  dkeffer@utk.edu
%  last updated:  June 1, 2017
%
clear all;
close all;
format long;
%
%  discretize radial dimension
%
rmin = 0.0;
rmax = 50.0;
dr = 0.01;
rvec = [rmin:dr:rmax];
nr = length(rvec);
%
%  test system parameters
%
rp1 = 7.0;
rp2 = rp1;
dp = 25.0;
%
```

```
%  compute RDF
%
g = zeros(nr,1);
g = gofr_spheresphere(dp,rp1,rp2,nr,rvec);
%
%  normalize by 4*pi*r^2
%
pi = 2.0*asin(1.0);
gnorm = zeros(nr,1);
for i = 2:1:nr
    fac = 1.0/(4.0*pi*rvec(i)^2);
    gnorm(i) = fac*g(i);
end
%
%  plot RDF
%
figure(1);
plot(rvec,gnorm,'k-');
xlabel(' separation');
ylabel(' radial distribution function ');
legend('scaled by 4*pi*r^2');
%
figure(2);
plot(rvec,g,'r-');
xlabel(' separation');
ylabel(' radial distribution function ');
legend('unscaled');

%
%  check volume
%
vol1 = 4.0/3.0*pi*rp1^3;
vol2 = 4.0/3.0*pi*rp2^3;
volprod = vol1*vol2;
%
```

```
integral = 0.0;
integralnorm = 0.0;
cumulative = zeros(nr,1);
for i = 2:1:nr
    base = rvec(i) - rvec(i-1);
    height1n = 4.0*pi*rvec(i-1)^2*gnorm(i-1);
    height2n = 4.0*pi*rvec(i)^2*gnorm(i);
    height1 = g(i-1);
    height2 = g(i);
    area = 0.5*base*(height1 + height2);
    areanorm = 0.5*base*(height1n + height2n);
    cumulative(i) = cumulative(i-1) + areanorm;
    integral = integral + area;
    integralnorm = integralnorm + areanorm;
end
%
%  plot cumulative RDF
%
figure(3);
plot(rvec,cumulative,'k-');
xlabel(' separation');
ylabel(' cumulative distribution function ');
%
%  error checking
%
diff = (integral - volprod)/volprod;
diffnorm = (integralnorm - volprod)/volprod;
fprintf(1, ' analytical %e numerical %e errors %e %e \n',
   volprod,integral,diff,diffnorm);
```

A.3.2 Functions

```
%
%  gofr_spheresphere
%
```

```
%  This code calculates the contribution to the radial
   distribution function
%  due to the atoms distributed uniformly over two spheres
   of radius rp1 and rp2
%  and separated by a distance p.
%
%  The RDF is returned in units of volume squared.
%  The RDF is NOT normalized by a factor of 1.0/(4.0*pi*r^2)
   .
%  For this version, the value of rp1 equal to rp2.
%
% use:
% g = gofr_spheresphere(dp,rp1,rp2,nr,rvec)
%
% inputs:
% dp:  distance between particles
% rp1:  radius of particle 1
% rp2:  radius of particle 2
% nr:  number of radial points to evaluate function
% rvec:  vector of radial positions
%
% outputs:
% g:  radial distribution function
%
%  authors: David J. Keffer & Akinola D. Oyedele
%  Dept. of Materials Science & Engineering
%  University of Tennessee
%  dkeffer@utk.edu
%  last updated:  June 1, 2017
%
function g = gofr_spheresphere(dp,rp1,rp2,nr,rvec)
%
% input parameters
%
fvec = zeros(nr,1); % d/dr
```

```
g = zeros(nr,1); % Radial distribution function
rb = dp;
%
%  create the volume as a function of r for this value of
   rp1
%
rmin = rb-rp1-rp2;
rlim1 =rb-rp2;
rlim2 = rb-rp2+rp1;
rlim3 = rb+rp2;
rmax = rb+rp1+rp2;

for i = 1:1:nr
    r = rvec(i);
    %
    if r <= rmin
        % Case I: No overlap
        fvec(i) = 0;

    elseif (r > rmin) && (r <= rlim1)
        % Case II A: Some overlap at some points in sphere 1
        fvec(i) = caseIIa(r,rp1,rp2,rb);

    elseif (r > rlim1) && (r < rlim2)
        % Case II* A: Some overlap at some points in sphere
          1
        fr_II_star_A_1 = caseIIstar_A1 (r,rp2,rb);
        fr_II_star_A_2 = caseIIstar_A2 (r,rp1,rp2,rb);
        fvec(i) = fr_II_star_A_1 + fr_II_star_A_2;

    elseif (r >= rlim2) && (r <= rlim3)
        % Case III A: Some overlap at some points in sphere
          1
        fr_IIIA_1 = caseIII_A1 (r,rp2,rb);
        fr_IIIA_2 = caseIII_A2 (r,rp1,rp2,rb);
```

```
        fr_IIIA = fr_IIIA_1 + fr_IIIA_2;
        %
        % Case III B: All overlap at some points in sphere 1
        fr_IIIB = caseIII_B (r,rp1,rp2,rb);
        fvec(i) = fr_IIIA + fr_IIIB;

    elseif (r > rlim3) && (r < rmax)
        % Case III* A: Some overlap at some points in sphere
            1
        fr_III_star_A = caseIIIstar_A (r,rp1,rp2,rb);
        %
        % Case III* B
        fr_III_star_B_1 = 16/3*pi^2*rp2^3*(-rb-rp2+r)^2;
        fr_III_star_B_2 = caseIIIstar_B2(r,rp1,rp2,rb);
        fr_III_star_B = fr_III_star_B_1 + fr_III_star_B_2;
        fvec(i) = fr_III_star_A + fr_III_star_B;

    elseif r >= rmax
        % Case IV: All overlap at all points in sphere 1 and
            2
        fvec(i) = 0;
    end
end

% fac = 1.0/(4.0*pi);
for i = 2:1:nr
    %fac2 = fac/(rvec(i)*rvec(i));
    fac2 = 1.0; % NOTE: keffer added this
    g(i) = fac2*fvec(i);
end
end


function result=caseIIa(r,rp1,rp2,rb)
Fac1 = ((rp2^2*rb-rp2*rb^2+rp2*rp1^2-rb*r^2)/(rp2-rb));
```

```
Fac2 = -168*r*rp1^5*rp2^2+84*Fac1^(5/2)*rp2*rb^2*r/(rp2-rb);
Fac3 = -5040*rp2^4*r^4-2016*rp2^7*r-6048*r^5*rp2^3-42*rp2^2*
   rb^5*r;
Fac4 = 420*rp2^2*Fac1^(3/2)*rb^3*r/(rp2-rb)+3486*rb*rp2^6*r;
Fac5 = -840*r^3*Fac1^(3/2)*rp2^2-840*r^3*Fac1^(3/2)*rb^2;
Fac6 = 630*r^5*Fac1^(1/2)*rb^3/(rp2-rb)+840*rp2^4*r*Fac1
   ^(3/2);
Fac7 = -2100*rb*rp1^2*rp2^4*r+840*rp2^2*r*Fac1^(3/2)*rb
   ^2+2016*rp2^2*r^6;
Fac8 = -10080*r^4*rp2^3*rb-210*rp2*rb^5*r^2+2100*rp2*rb^3*r
   ^4;
Fac9 = 3486*rp2*r^6*rb-1008*rp2^6*rb^2+2016*rp2^7*rb+1008*
   rp2^8;
Fac10 = -1260*rb^2*r^3*rp2^3-2310*rb^2*rp2^5*r+1680*r^3*Fac1
   ^(3/2)*rp2*rb;
Fac11 = -1260*r^5*Fac1^(1/2)*rp2*rb^2/(rp2-rb)-1680*rp2^3*r*
   Fac1^(3/2)*rb;
Fac12 = Fac2+Fac3+Fac4+Fac5+Fac6+Fac7+Fac8+Fac9+Fac10+Fac11;
Fac13 = 2520*rp2^3*r^3*Fac1^(1/2)*rb^2/(rp2-rb)+336*r*Fac1
   ^(5/2)*rp2*rb;
Fac14 = -840*r^3*Fac1^(3/2)*rp2*rb^2/(rp2-rb)-5838*rp2*r^5*
   rb^2;
Fac15 = 11886*rp2^2*r^5*rb-420*rp2^3*rb^4*r+1260*rp2^4*rb^3*
   r;
Fac16 = -420*rp2^2*rb^3*r^3+12180*rb*r^4*rp2^3-210*rb*r^2*
   rp2^5;
Fac17 = -1260*rb^3*r^2*rp2^3-9240*rb^2*r^4*rp2^2+840*rb^2*r
   ^2*rp2^4;
Fac18 = 840*rp2^4*r*rp1^3-840*r^3*rp1^3*rp2^2+42*rp2*r*rb^6;
Fac19 = 6048*rb^2*r^5*rp2+5040*rp2^2*r^4*rb^2-4032*r^6*rp2*
   rb;
Fac20 = -2016*rp2^7*rb+6048*rp2^3*r^5+2016*rb^2*r^6+2016*rp2
   ^7*r;
Fac21 = Fac12+Fac13+Fac14+Fac15+Fac16+Fac17+Fac18+Fac19+
   Fac20;
```

```
Fac22 = 420*rp2*rb^4*r^3+2016*rp2^5*r*rb^2+5040*rp2^4*r^4;
Fac23 = 630*rb*rp1^4*rp2*r^2-1680*rb^2*rp1^3*rp2*r^2-12096*r
   ^5*rp2^2*rb;
Fac24 = -2520*rb^2*rp1^2*rp2^2*r^2-2100*rb*rp1^2*rp2*r^4;
Fac25 = 1260*r^3*rb*rp1^2*rp2^2-1260*r^3*rb^2*rp1^2*rp2;
Fac26 = 840*r^3*rp1^3*rp2*rb-840*rp2^3*r*rp1^3*rb-1008*rp2
   ^8;
Fac27 = -4032*r*rp2^6*rb+1008*rb^2*rp2^6-2016*rp2^2*r^6;
Fac28 = -840*r*rp1^3*rp2^2*rb^2+840*r*rp1^3*rp2*rb^3;
Fac29 = -420*r*rb^4*rp1^2*rp2+168*r*rp1^5*rp2*rb+630*r*rb*
   rp1^4*rp2^2;
Fac30 = -168*r*Fac1^(5/2)*rb^2+630*r^5*Fac1^(1/2)*rp2^2*rb/(
   rp2-rb);
Fac31 = -1260*rp2^4*r^3*Fac1^(1/2)*rb/(rp2-rb);
Fac32 = Fac21+Fac22+Fac23+Fac24+Fac25+Fac26+Fac27+Fac28+
   Fac29+Fac30+Fac31;
Fac33 = -168*r*Fac1^(5/2)*rp2^2+1680*rb*rp1^3*rp2^2*r^2;
Fac34 = 630*rp2^4*Fac1^(1/2)*rb^3*r/(rp2-rb);
Fac35 = -42*Fac1^(5/2)*rp2^2*rb*r/(rp2-rb);
Fac36 = -840*rp2^3*Fac1^(3/2)*rb^2*r/(rp2-rb)+840*rp2^2*rb
   ^4*r^2;
Fac37 = 630*rp2^6*Fac1^(1/2)*rb*r/(rp2-rb)+1260*rb*rp1^2*rp2
   ^3*r^2;
Fac38 = -1260*rp2^2*r^3*Fac1^(1/2)*rb^3/(rp2-rb)+2100*rb*r
   ^3*rp2^4;
Fac39 = 420*rp2^4*Fac1^(3/2)*rb*r/(rp2-rb)+1260*rb^3*rp1^2*
   rp2*r^2;
Fac40 = 420*r^3*Fac1^(3/2)*rb^3/(rp2-rb)+1260*rp2^3*r*rb^2*
   rp1^2;
Fac41 = -630*r*rb^2*rp1^4*rp2+420*r*rb^3*rp1^2*rp2^2;
Fac42 = -42*Fac1^(5/2)*rb^3*r/(rp2-rb);
Fac43 = -1260*rp2^5*Fac1^(1/2)*rb^2*r/(rp2-rb);
Fac44 = +420*r^3*Fac1^(3/2)*rp2^2*rb/(rp2-rb);
Fac45 = Fac32+Fac33+Fac34+Fac35+Fac36+Fac37+Fac38+Fac39+
   Fac40+Fac41+Fac42;
```

```
Fac46 = Fac43+Fac44;
result = 1/1260*pi^2*(Fac45+Fac46)/rp2/(rp2-rb)/rb;
end


function result = caseIIstar_A1 (r,rp2,rb)
Fac0 = 6*rp2^2+(-2*r-2*rp2)*(6*rp2-6*r);
Fac1 = 2/5*(r-rb+rp2)^6-8/5*r*(r-rb+rp2)^5;
Fac2 = 4*rp2*r-2*r^2-2*rp2^2+4*rb^2;
Fac3 = 2*(r+rp2)^2*(6*rp2-6*r)-24*r*rb^2;
Fac4 = 2*(r+rp2)*(2*r+2*rp2)+2*(r+rp2)^2-12*rp2*r+6*r^2+Fac0
   ;
Fac5 = 2/3*(r+rp2)^2+2/3*(-2*r-2*rp2)*(2*r+2*rp2)+Fac2;
Fac6 = 2*Fac4*rb+4*(r+rp2)*(6*rp2*r-3*r^2-3*rp2^2)+Fac3;
Fac7 = (r+rp2)^2*(2*r+2*rp2)+(-2*r-2*rp2)*(6*rp2*r-3*r^2-3*
   rp2^2);
Fac8 = (r+rp2)^2+(-2*r-2*rp2)*(2*r+2*rp2)+6*rp2*r-3*r^2-3*
   rp2^2;
Fac9 = 2*rb^4+2*Fac7*rb+2*(r+rp2)^2*(6*rp2*r-3*r^2-3*rp2^2)
   +2*Fac8*rb^2;
Fac10 = Fac1+Fac5*(r-rb+rp2)^4+1/3*Fac6*(r-rb+rp2)^3+Fac9*(r
   -rb+rp2)^2;
result = 1/6*pi^2*Fac10/rb;
end


function result = caseIIstar_A2 (r,rp1,rp2,rb)
Fac1 = ((rp2^2*rb-rp2*rb^2+rp2*rp1^2-rb*r^2)/(rp2-rb));
Fac2 = -1260*r^5*Fac1^(1/2)*rp2*rb^2/(rp2-rb)-1680*rp2^3*r*
   Fac1^(3/2)*rb;
Fac3 = -6930*rp2*rb^5*r^2+2520*rp2^3*r^3*Fac1^(1/2)*rb^2/(
   rp2-rb);
Fac4 = 336*r*Fac1^(5/2)*rp2*rb+1008*rp2^8;
Fac5 = 12978*rp2*r^5*rb^2-19026*rp2^2*r^5*rb-24780*rb*r^3*
   rp2^4;
```

```
Fac6 = 24570*rb^2*rp2^5*r+420*rp2^2*Fac1^(3/2)*rb^3*r/(rp2-
   rb);
Fac7 = 630*rp2^6*Fac1^(1/2)*rb*r/(rp2-rb)+420*r^3*Fac1^(3/2)
   *rb^3/(rp2-rb);
Fac8 = -168*r*Fac1^(5/2)*rb^2-41580*rb^3*r^2*rp2^3+68040*rb
   ^2*r^4*rp2^2;
Fac9 = -7140*rp2^3*rb^4*r-12180*rp2^4*rb^3*r;
Fac10 = -840*r^3*Fac1^(3/2)*rp2^2+630*r^5*Fac1^(1/2)*rp2^2*
   rb/(rp2-rb);
Fac11 = -840*r^3*Fac1^(3/2)*rb^2+630*r^5*Fac1^(1/2)*rb^3/(
   rp2-rb);
Fac12 = 27720*rp2^2*rb^4*r^2-2646*rp2*r*rb^6-13986*rb*rp2^6*
   r;
Fac13 = 9366*rp2^2*rb^5*r-81060*rp2^2*rb^3*r^3;
Fac14 = Fac2+Fac3+Fac4+Fac5+Fac6+Fac7+Fac8+Fac9+Fac10+Fac11+
   Fac12+Fac13;
Fac15 = -1260*rp2^5*Fac1^(1/2)*rb^2*r/(rp2-rb)-41580*rb*r^4*
   rp2^3;
Fac16 = -42*Fac1^(5/2)*rb^3*r/(rp2-rb)-168*r*Fac1^(5/2)*rp2
   ^2;
Fac17 = -1260*rp2^4*r^3*Fac1^(1/2)*rb/(rp2-rb)+1680*rb*rp1
   ^3*rp2^2*r^2;
Fac18 = 27720*rb^2*r^2*rp2^4-6048*rb^6*rp2^2+8064*rp2^3*rb
   ^5;
Fac19 = 3360*rp2^4*rb^4-42*Fac1^(5/2)*rp2^2*rb*r/(rp2-rb);
Fac20 = 840*rp2^4*r*rp1^3-840*r^3*rp1^3*rp2^2+1344*rp2*rb^7;
Fac21 = -840*rp2^3*Fac1^(3/2)*rb^2*r/(rp2-rb)-20160*rp2^5*rb
   ^3;
Fac22 = -2100*rb*rp1^2*rp2^4*r-12096*r^5*rp2^2*rb-4032*r*rp2
   ^6*rb;
Fac23 = -546*rp2*r^6*rb+1008*rb^2*rp2^6+21168*rp2^6*rb
   ^2-4032*r^6*rp2*rb;
Fac24 = Fac14+Fac15+Fac16+Fac17+Fac18+Fac19+Fac20+Fac21+
   Fac22+Fac23;
```

```
Fac25 = -2016*rp2^7*rb+6048*rb^2*r^5*rp2+5040*rp2^2*r^4*rb
   ^2;
Fac26 = 2016*rp2^5*r*rb^2+2016*rb^2*r^6+2016*rp2^7*r-31500*
   rp2*rb^3*r^4;
Fac27 = 2016*rp2^2*r^6+630*rb*rp1^4*rp2*r^2-1680*rb^2*rp1^3*
   rp2*r^2;
Fac28 = 1260*rb*rp1^2*rp2^3*r^2-2520*rb^2*rp1^2*rp2^2*r^2;
Fac29 = 1260*rb^3*rp1^2*rp2*r^2+1260*r^3*rb*rp1^2*rp2^2;
Fac30 = 1260*rp2^3*r*rb^2*rp1^2+840*r^3*rp1^3*rp2*rb+6048*
   rp2^3*r^5;
Fac31 = 2016*rp2^2*r^6+5040*rp2^4*r^4+2016*rp2^7*r-2100*rb*
   rp1^2*rp2*r^4;
Fac32 = -10080*r^4*rp2^3*rb-840*rp2^3*r*rp1^3*rb-840*r*rp1
   ^3*rp2^2*rb^2;
Fac33 = 420*r*rb^3*rp1^2*rp2^2-420*r*rb^4*rp1^2*rp2+168*r*
   rp1^5*rp2*rb;
Fac34 = -630*r*rb^2*rp1^4*rp2+1680*r^3*Fac1^(3/2)*rp2*rb;
Fac35 = Fac24+Fac25+Fac26+Fac27+Fac28+Fac29+Fac30+Fac31+
   Fac32+Fac33+Fac34;
Fac36 = Fac35+630*r*rb*rp1^4*rp2^2+420*rp2^4*Fac1^(3/2)*rb*r
   /(rp2-rb);
Fac37 = 79380*rb^2*r^3*rp2^3-6930*rb*r^2*rp2^5+840*rp2^4*r*
   Fac1^(3/2);
Fac38 = 6048*r^5*rp2^3+420*r^3*Fac1^(3/2)*rp2^2*rb/(rp2-rb);
Fac39 = 840*r*rp1^3*rp2*rb^3-1260*rp2^2*r^3*Fac1^(1/2)*rb
   ^3/(rp2-rb);
Fac40 = 5040*rp2^4*r^4-840*r^3*Fac1^(3/2)*rp2*rb^2/(rp2-rb)
   -8736*rp2^7*rb;
Fac41 = 27300*rp2*rb^4*r^3+630*rp2^4*Fac1^(1/2)*rb^3*r/(rp2-
   rb);
Fac42 = 84*Fac1^(5/2)*rp2*rb^2*r/(rp2-rb)-168*r*rp1^5*rp2
   ^2+1008*rp2^8;
Fac43 = -1260*r^3*rb^2*rp1^2*rp2+840*rp2^2*r*Fac1^(3/2)*rb
   ^2;
Fac44 = Fac36+Fac37+Fac38+Fac39+Fac40+Fac41+Fac42+Fac43;
```

```
result = 1/1260*pi^2*(Fac44)/rp2/(rp2-rb)/rb;
end


function result = caseIII_A1 (r,rp2,rb)
Fac0 = 6*rp2^2+(-2*r-2*rp2)*(6*rp2-6*r);
Fac1 = -2/5*(rb+rp2-r)^6-8/5*r*(rb+rp2-r)^5;
Fac2 = 4*rp2*r-2*r^2-2*rp2^2+4*rb^2;
Fac3 = 2*(r+rp2)^2*(6*rp2-6*r)-24*r*rb^2;
Fac4 = 2*(r+rp2)*(2*r+2*rp2)+2*(r+rp2)^2-12*rp2*r+6*r^2+Fac0
   ;
Fac5 = 2/3*(r+rp2)^2+2/3*(-2*r-2*rp2)*(2*r+2*rp2)+Fac2;
Fac6 = 2*Fac4*rb+4*(r+rp2)*(6*rp2*r-3*r^2-3*rp2^2)+Fac3;
Fac7 = (r+rp2)^2*(2*r+2*rp2)+(-2*r-2*rp2)*(6*rp2*r-3*r^2-3*
   rp2^2);
Fac8 = (r+rp2)^2+(-2*r-2*rp2)*(2*r+2*rp2)+6*rp2*r-3*r^2-3*
   rp2^2;
Fac9 = 2*rb^4+2*Fac7*rb+2*(r+rp2)^2*(6*rp2*r-3*r^2-3*rp2^2)
   +2*Fac8*rb^2;
Fac10 = Fac1-Fac5*(rb+rp2-r)^4+1/3*Fac6*(rb+rp2-r)^3-Fac9*(
   rb+rp2-r)^2;
result = 1/6*pi^2*Fac10/rb;
end


function result = caseIII_A2 (r,rp1,rp2,rb)
Fac1 = ((-rp2^2*rb-rp2*rb^2+rp2*rp1^2+rb*r^2)/(rb+rp2));
Fac2 = 420*rp2^2*Fac1^(3/2)*rb^3*r/(rb+rp2)-6930*rp2*rb^5*r
   ^2;
Fac3 = 840*rp2^3*Fac1^(3/2)*rb^2*r/(rb+rp2);
Fac4 = 2016*rp2^7*r-1260*rp2^4*r^3*Fac1^(1/2)*rb/(rb+rp2)
   +8064*rp2^3*rb^5;
Fac5 = 630*r^5*Fac1^(1/2)*rp2^2*rb/(rb+rp2)-840*rp2^4*r*Fac1
   ^(3/2);
```

```
Fac6 = -31500*rp2*rb^3*r^4+12978*rp2*r^5*rb^2+19026*rp2^2*r
   ^5*rb;
Fac7 = 26460*rb*r^3*rp2^4+79380*rb^2*r^3*rp2^3+1050*rb^2*rp2
   ^5*r;
Fac8 = 1260*rp2^5*Fac1^(1/2)*rb^2*r/(rb+rp2);
Fac9 = 420*rp2^4*Fac1^(3/2)*rb*r/(rb+rp2);
Fac10 = -420*r*rb^4*rp1^2*rp2-168*r*rp1^5*rp2*rb+27300*rp2*
   rb^4*r^3;
Fac11 = -9366*rp2^2*rb^5*r+81060*rp2^2*rb^3*r^3-41580*rb*r
   ^4*rp2^3;
Fac12 = -3570*rb*r^2*rp2^5-41580*rb^3*r^2*rp2^3-68040*rb^2*r
   ^4*rp2^2;
Fac13 = -24360*rb^2*r^2*rp2^4-7140*rp2^3*rb^4*r+420*rp2^4*rb
   ^3*r;
Fac14 = 3360*rp2^4*rb^4-2646*rp2*r*rb^6+2226*rb*rp2^6*r;
Fac15 = Fac2+Fac3+Fac4+Fac5+Fac6+Fac7+Fac8+Fac9+Fac10+Fac11+
   Fac12+Fac13;
Fac16 = 840*rp2^4*r*rp1^3-840*r^3*rp1^3*rp2^2+1344*rp2*rb^7;
Fac17 = -630*r*rb*rp1^4*rp2^2+1680*rb*rp1^3*rp2^2*r^2+Fac14;
Fac18 = 1680*r^3*Fac1^(3/2)*rb*rp2+1008*rp2^8*-1+6048*rb^6*
   rp2^2;
Fac19 = -840*rp2^2*r*Fac1^(3/2)*rb^2+6048*r^5*rp2^3;
Fac20 = -42*Fac1^(5/2)*rp2^2*rb*r/(rb+rp2);
Fac21 = 2016*r^6*-1*rb^2-2016*r*rp2^7*-1+5040*r^4*rp2^4*-1;
Fac22 = -6048*r^5*-1*rp2^3-12096*-1*rp2^2*rb*r^5-27720*rp2
   ^2*rb^4*r^2;
Fac23 = 4032*-1*rp2*rb*r^6+840*r^3*Fac1^(3/2)*rb^2-2016*rp2
   ^5*-1*rb^2*r;
Fac24 = -2520*rp2^3*r^3*Fac1^(1/2)*rb^2/(rb+rp2)-5040*rp2^4*
   r^4;
Fac25 = -1008*rp2^8+630*r^5*Fac1^(1/2)*rb^3/(rb+rp2)+630*rb*
   rp1^4*rp2*r^2;
Fac26 = 1680*rb^2*rp1^3*rp2*r^2+1260*rb*rp1^2*rp2^3*r^2;
Fac27 = Fac15+Fac16+Fac17+Fac18+Fac19+Fac20+Fac21+Fac22+
   Fac23+Fac24+Fac25;
```

```
Fac28 = 840*r^3*Fac1^(3/2)*rb^2*rp2/(rb+rp2)+420*rb*rp1^2*
   rp2^4*r+Fac26;
Fac29 = -2016*rp2^2*r^6+5040*r^4*-1*rb^2*rp2^2-6048*r^5*-1*
   rb^2*rp2;
Fac30 = -1008*rp2^6*rb^2-4032*-1*rp2^6*rb*r+10080*-1*rp2^3*
   rb*r^4;
Fac31 = 2016*-1*rp2^7*rb+1008*rp2^6*-1*rb^2-2016*rp2^7*rb;
Fac32 = 2520*rb^2*rp1^2*rp2^2*r^2-2100*rb*rp1^2*rp2*r^4;
Fac33 = -1260*r^3*rb*rp1^2*rp2^2-1260*r^3*rb^2*rp1^2*rp2;
Fac34 = 1260*rp2^3*r*rb^2*rp1^2-840*r^3*rp1^3*rp2*rb-168*r*
   rp1^5*rp2^2;
Fac35 = 840*rp2^3*r*rp1^3*rb-630*r*rb^2*rp1^4*rp2-840*r*rp1
   ^3*rp2^2*rb^2;
Fac36 = -840*r*rp1^3*rp2*rb^3-420*r*rb^3*rp1^2*rp2^2+168*r*
   Fac1^(5/2)*rb^2;
Fac37 = 420*r^3*Fac1^(3/2)*rb^3/(rb+rp2)+168*r*Fac1^(5/2)*
   rp2^2;
Fac38 = -546*rp2*r^6*rb-1680*rp2^3*r*Fac1^(3/2)*rb+2016*r
   ^6*-1*rp2^2;
Fac39 = -42*Fac1^(5/2)*rb^3*r/(rb+rp2)+1260*rb^3*rp1^2*rp2*r
   ^2;
Fac40 = 840*r^3*Fac1^(3/2)*rp2^2-1260*rp2^2*r^3*Fac1^(1/2)*
   rb^3/(rb+rp2);
Fac41 = 1260*r^5*Fac1^(1/2)*rb^2*rp2/(rb+rp2)+336*r*Fac1
   ^(5/2)*rb*rp2;
Fac42 = 630*rp2^6*Fac1^(1/2)*rb*r/(rb+rp2);
Fac43 = 630*rp2^4*Fac1^(1/2)*rb^3*r/(rb+rp2);
Fac44 = 420*r^3*Fac1^(3/2)*rp2^2*rb/(rb+rp2);
Fac45 = -84*Fac1^(5/2)*rp2*rb^2*r/(rb+rp2);
Fac46 = Fac38+Fac39+Fac40+Fac41+Fac42+Fac43+Fac44+Fac45;
Fac47 = Fac27+Fac28+Fac29+Fac30+Fac31+Fac32+Fac33+Fac34+
   Fac35+Fac36+Fac37;
result = 1/1260*pi^2*(Fac46+Fac47)/rp2/(rb+rp2)/rb;
end
```

```
function result = caseIII_B (r,rp1,rp2,rb)
Fac1 = 8/3*pi^2*rp2^3;
Fac2 = 1/2*rp2/(rb+rp2)-1/2;
Fac3 = rp1^2-(rb+rp2-r)^2;
Fac4 = 1/2*(-rp2^2*rb-rp2*rb^2+rb*r^2)/(rb+rp2)-1/2*rb^2;
Fac5 = -Fac2*(rb+rp2-r)^3-rb*(rb+rp2-r)^2;
result = Fac1*(-Fac5+1/2*rb*r/(rb+rp2)*Fac3+1/2*Fac4*(2*rb
   +2*rp2-2*r))/rb;
end


function result = caseIIIstar_A (r,rp1,rp2,rb)
Fac1 = ((-rp2^2*rb-rp2*rb^2+rp2*rp1^2+rb*r^2)/(rb+rp2));
Fac2 = 1260*rp2^5*Fac1^(1/2)*rb^2*r/(rb+rp2)-210*rp2*rb^5*r
   ^2;
Fac3 = -2016*rp2^7*r-6048*r^5*rp2^3+420*rp2^4*Fac1^(3/2)*rb*
   r/(rb+rp2);
Fac4 = -1260*r^3*rb*rp1^2*rp2^2+630*r^5*Fac1^(1/2)*rb^3/(rb+
   rp2);
Fac5 = -840*r*rp1^3*rp2^2*rb^2-630*r*rb^2*rp1^4*rp2+840*rp2
   ^3*r*rp1^3*rb;
Fac6 = 1260*rp2^3*r*rb^2*rp1^2+168*r*Fac1^(5/2)*rb^2+2100*
   rp2*rb^3*r^4;
Fac7 = -840*r*rp1^3*rp2*rb^3+420*r^3*Fac1^(3/2)*rb^3/(rb+rp2
   );
Fac8 = 1260*r^5*Fac1^(1/2)*rb^2*rp2/(rb+rp2)+840*r^3*Fac1
   ^(3/2)*rp2^2;
Fac9 = -840*rp2^4*r*Fac1^(3/2)-840*rp2^2*r*Fac1^(3/2)*rb^2;
Fac10 = -630*r*rb*rp1^4*rp2^2-168*r*rp1^5*rp2*rb-420*r*rb^4*
   rp1^2*rp2;
Fac11 = 1680*rb*rp1^3*rp2^2*r^2-42*Fac1^(5/2)*rb^3*r/(rb+rp2
   );
Fac12 = 2016*r^6*-1*rb^2+5040*r^4*rp2^4*-1-2016*r*rp2
   ^7*-1+42*rp2*r*rb^6;
```

```
Fac13 = Fac2+Fac3+Fac4+Fac5+Fac6+Fac7+Fac8+Fac9+Fac10+Fac11+
   Fac12;
Fac14 = -1260*rp2^2*r^3*Fac1^(1/2)*rb^3/(rb+rp2)-6048*r
   ^5*-1*rp2^3;
Fac15 = 2016*r^6*-1*rp2^2-42*Fac1^(5/2)*rp2^2*rb*r/(rb+rp2);
Fac16 = 3486*rp2*r^6*rb-2016*0*rp2^2*rb*r^6+1008*rp2^6*rb^2;
Fac17 = 2016*-1*rp2^7*rb+1008*rp2^8+2016*rp2^7*rb+420*rb*rp1
   ^2*rp2^4*r;
Fac18 = 2016*rp2^2*r^6-2100*rb*rp1^2*rp2*r^4+1260*rb^3*rp1
   ^2*rp2*r^2;
Fac19 = 10080*-1*rp2^3*rb*r^4-4032*-1*rp2^6*rb*r-6048*r
   ^5*-1*rb^2*rp2;
Fac20 = -5838*rp2*r^5*rb^2+4032*-1*rp2*rb*r^6-12096*-1*rp2
   ^2*rb*r^5;
Fac21 = -11886*rp2^2*r^5*rb-420*rb*r^3*rp2^4-1260*rb^2*r^3*
   rp2^3;
Fac22 = 1050*rb^2*rp2^5*r+840*rp2^4*r*rp1^3-840*r^3*rp1^3*
   rp2^2;
Fac23 = -1806*rb*rp2^6*r+420*rp2*rb^4*r^3+42*rp2^2*rb^5*r;
Fac24 = Fac13+Fac14+Fac15+Fac16+Fac17+Fac18+Fac19+Fac20+
   Fac21+Fac22+Fac23;
Fac25 = 12180*rb*r^4*rp2^3-3570*rb*r^2*rp2^5-1260*rb^3*r^2*
   rp2^3;
Fac26 = 9240*rb^2*r^4*rp2^2-1680*rp2^3*r*Fac1^(3/2)*rb-4200*
   rb^2*r^2*rp2^4;
Fac27 = 420*rp2^4*rb^3*r-168*r*rp1^5*rp2^2-2016*rp2^5*-1*rb
   ^2*r;
Fac28 = 840*r^3*Fac1^(3/2)*rb^2*rp2/(rb+rp2)+336*r*Fac1
   ^(5/2)*rb*rp2;
Fac29 = -2520*rp2^3*r^3*Fac1^(1/2)*rb^2/(rb+rp2)+1008*rp2
   ^6*-1*rb^2;
Fac30 = 2520*rb^2*rp1^2*rp2^2*r^2+1260*rb*rp1^2*rp2^3*r
   ^2+5040*rp2^4*r^4;
Fac31 = 420*rp2^2*Fac1^(3/2)*rb^3*r/(rb+rp2)+1008*rp2^8*-1;
```

```
Fac32 = 1680*rb^2*rp1^3*rp2*r^2+630*r^5*Fac1^(1/2)*rp2^2*rb
   /(rb+rp2);
Fac33 = Fac24+Fac25+Fac26+Fac27+Fac28+Fac29+Fac30+Fac31+
   Fac32;
Fac34 = Fac33+630*rp2^4*Fac1^(1/2)*rb^3*r/(rb+rp2)+168*r*
   Fac1^(5/2)*rp2^2;
Fac35 = -84*Fac1^(5/2)*rp2*rb^2*r/(rb+rp2)-1260*r^3*rb^2*rp1
   ^2*rp2;
Fac36 = 1680*r^3*Fac1^(3/2)*rb*rp2+630*rp2^6*Fac1^(1/2)*rb*r
   /(rb+rp2);
Fac37 = -840*r^3*rp1^3*rp2*rb+5040*r^4*-1*rb^2*rp2^2-420*rp2
   ^3*rb^4*r;
Fac38 = 840*r^3*Fac1^(3/2)*rb^2+840*rp2^3*Fac1^(3/2)*rb^2*r
   /(rb+rp2);
Fac39 = 630*rb*rp1^4*rp2*r^2+420*r^3*Fac1^(3/2)*rp2^2*rb/(rb
   +rp2);
Fac40 = -1260*rp2^4*r^3*Fac1^(1/2)*rb/(rb+rp2)-840*rp2^2*rb
   ^4*r^2;
Fac41 = -420*r*rb^3*rp1^2*rp2^2+420*rp2^2*rb^3*r^3;
Fac42 = Fac34+Fac35+Fac36+Fac37+Fac38+Fac39+Fac40+Fac41;
result = 1/1260*pi^2*(Fac42)/rp2/(rb+rp2)/rb;
end


function result = caseIIIstar_B2(r,rp1,rp2,rb)
Fac1 = 8/3*pi^2*rp2^3;
Fac2 = 1/2*rp2/(rb+rp2)-1/2;
Fac3 = rp1^2-(-rb-rp2+r)^2;
Fac4 = 1/2*(-rp2^2*rb-rp2*rb^2+rb*r^2)/(rb+rp2)-1/2*rb^2;
Fac5 = -Fac2*(-rb-rp2+r)^3-rb*(-rb-rp2+r)^2;
result = Fac1*(Fac5+1/2*rb*r/(rb+rp2)*Fac3+1/2*Fac4*(2*rb+2*
   rp2-2*r))/rb;
end
```

APPENDIX B
SUPPLEMENTARY DATA FOR CHAPTER 3

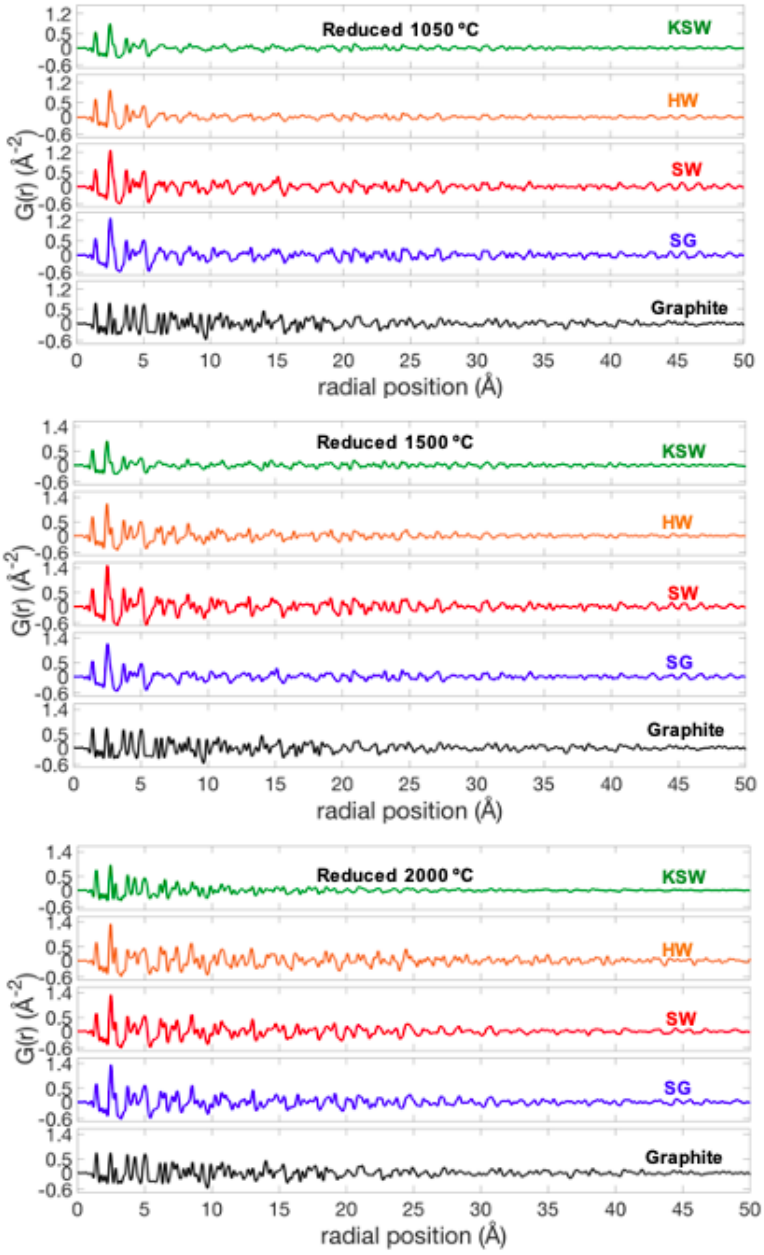


Figure B-1. PDF of carbon composites pyrolyzed in wet nitrogen with water density of 105 g m^{-3} and reduced at (top) 1050 °C, (middle) 1500 °C, and (bottom) 2000 °C.

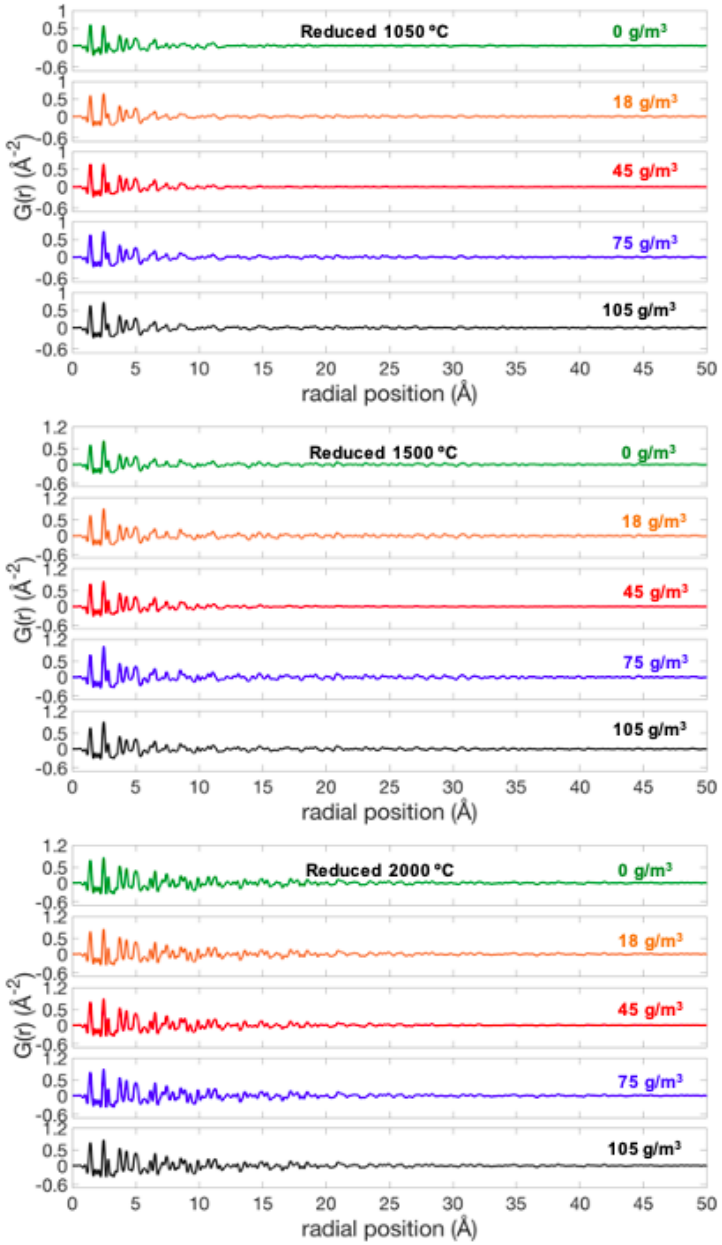


Figure B-2. Pair distribution functions of kraft softwood at increasing water densities: 0, 18, 45, 75, and 105 g m^{-3} during pyrolysis and after reduced at (top) 1050 °C, (middle) 1500 °C, and (bottom) 2000 °C collected at a synchrotron source.

Table B-1. C-C distances from reference and experimental data of composites reduced at 1050, 1500, and 2000 °C.

C-C pairs	Reference (Å) [3]	Experimental reduced 1050 °C				Experimental reduced 1500 °C				Experimental reduced 2000 °C			
		KSW (Å)	HW (Å)	SW (Å)	SG (Å)	KSW (Å)	HW (Å)	SW (Å)	SG (Å)	KSW (Å)	HW (Å)	SW (Å)	SG (Å)
C1 to C2	1.42	1.42	1.42	1.42	1.42	1.42	1.42	1.42	1.42	1.42	1.42	1.42	1.42
C1 to C3	2.47	2.47	2.49	2.5	2.5	2.48	2.49	2.49	2.49	2.46	2.48	2.48	2.48
C1 to C4	2.8	2.81	2.77	2.78	2.79	2.81	2.81	2.8	2.82	2.83	2.82	2.82	2.82
C1 to C5	3.77	3.74	3.74	3.73	3.73	3.74	3.74	3.73	3.74	3.75	3.74	3.74	3.74
C1 to C6	4.27	4.25	4.22	4.21	4.15	4.24	4.23	4.22	4.26	4.26	4.25	4.24	4.27
C1 to C7	5.01	5.01	5.01	5.02	5.01	5.00	5.00	5.01	4.97	4.99	4.98	4.98	4.97
C1 to C8	5.01	5.01	5.01	5.02	5.01	5.00	5.00	5.01	4.97	4.99	4.98	4.98	4.97

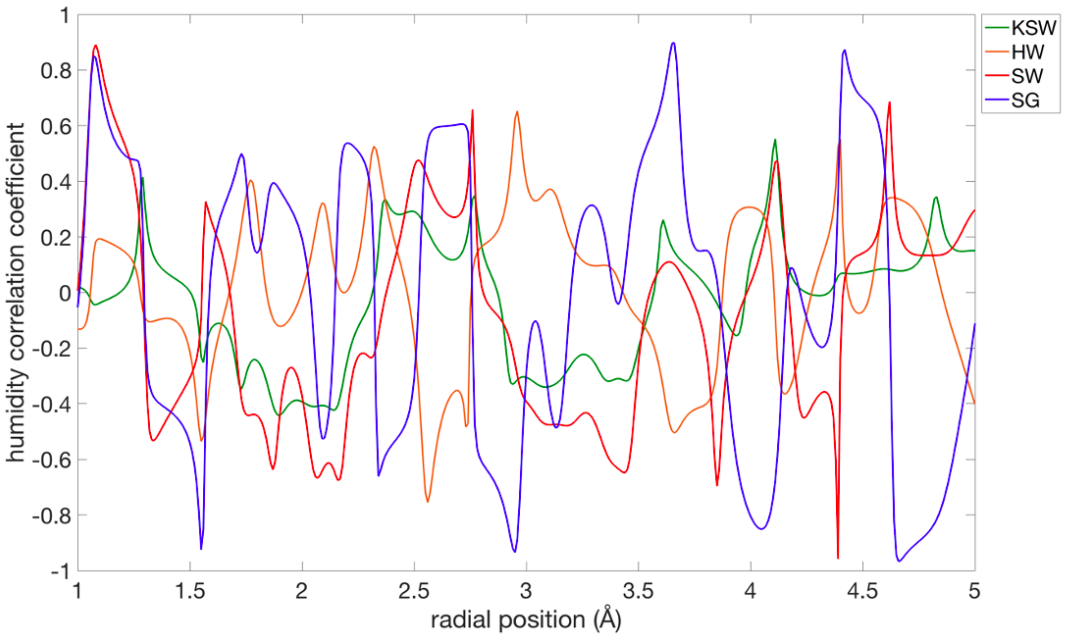


Figure B-3. a) Correlations of $G(r)$ for lignin feedstock with respect to humidity (water density). The coefficients correspond to a Pearson (linear) correlation for each radial position. Contrary to statistical analyses of temperature, humidity correlations of PDFs do not show a clear trend among the different lignin feedstocks. SG is the only feedstock to produce multiple high positive and negative correlations. we know that humidity manipulates microstructure (density of pores and sizes).

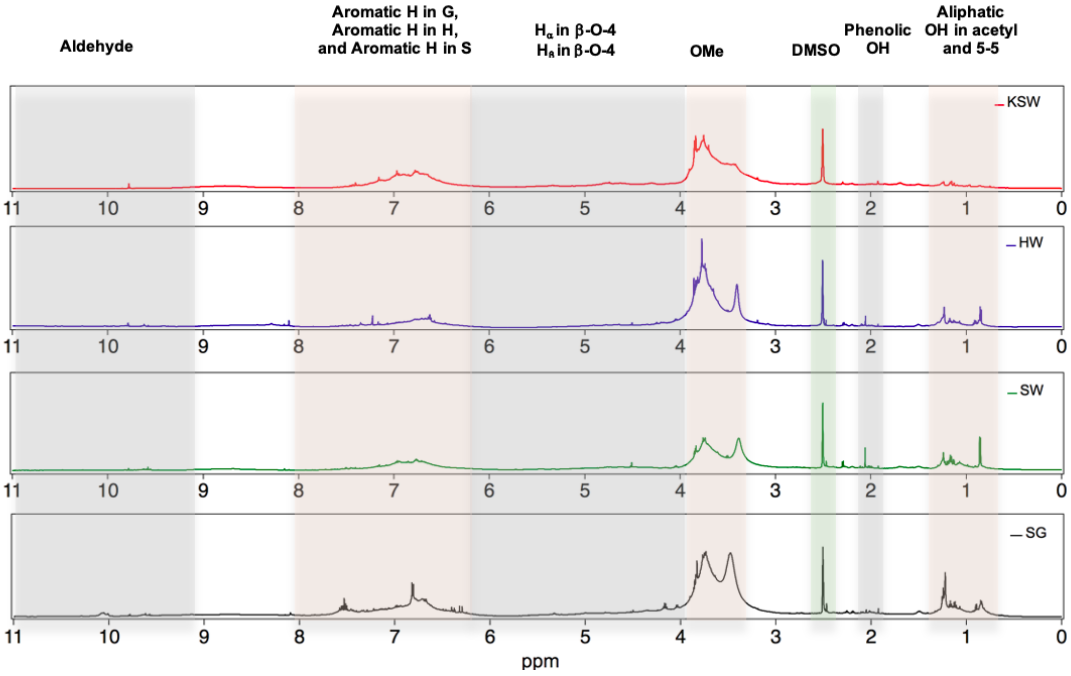


Figure B-4. ^{1}H-NMR spectra of lignin feedstocks (KSW, HW, SW, and SG) with typical functional groups in lignin.

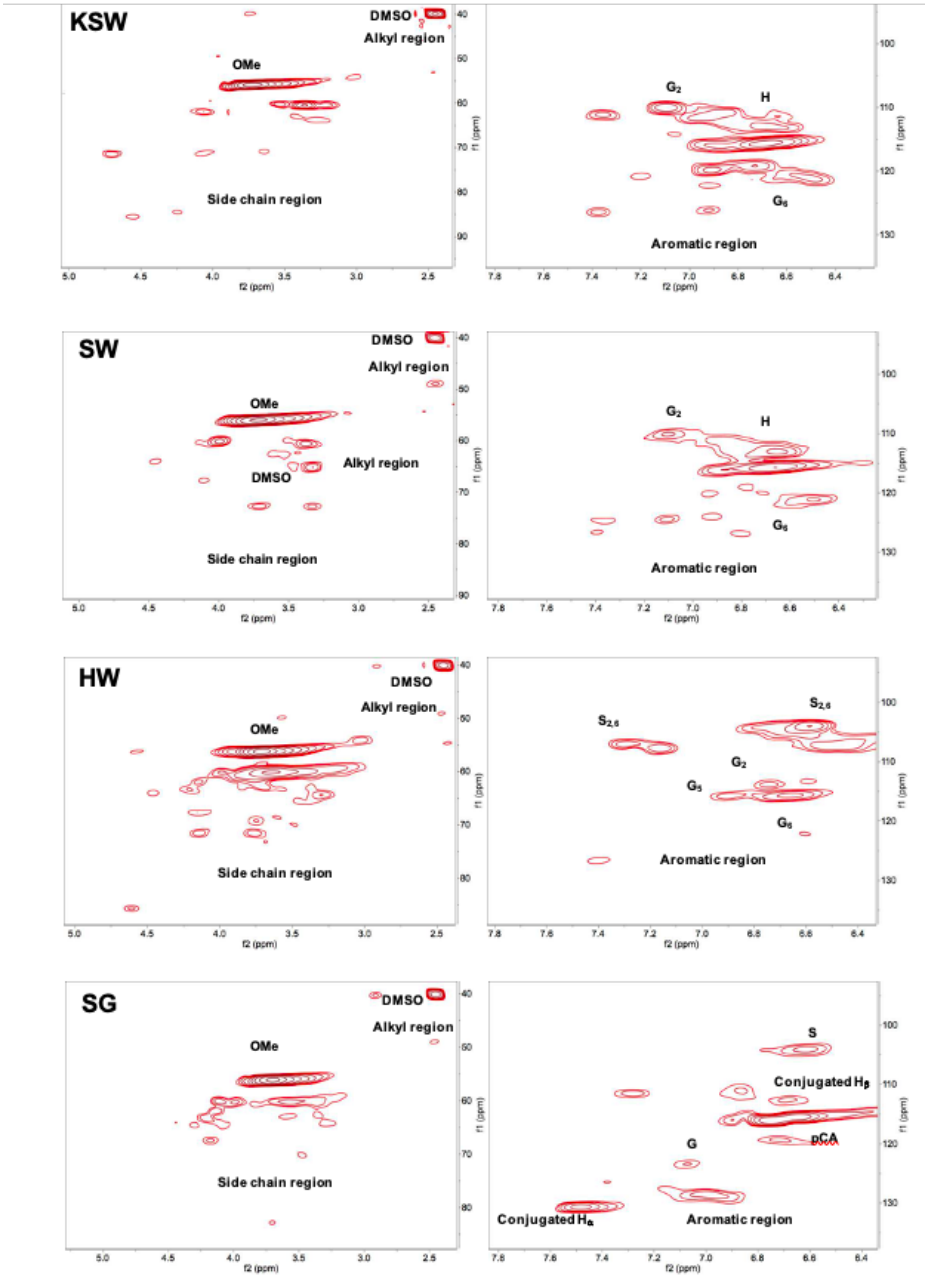


Figure B-5. Aromatic region, side chain region, and alkyl region from ^{13}C-^{1}H (HSQC) spectra of all lignin feedstocks. Syringyl (S) unit, guaiacyl (G) unit, *p*-hydroxyphenyl (H) unit, para-coumarates (pCA), methoxy (OMe), dimethyl sulfoside deuterated (DMSO).

Table B-2. 2D-NMR (^{13}C-^{1}H-HSQC) spectra of lignin feedstocks identifying the signal of principal groups.

Lignin feedstock	Signal location (^{13}C)	Signal location (^{1}H)	Designation [12, 69, 164, 166]	Absolute intensity	Relative abundance w.r.t. methoxy
KSW	121.17	6.5	unidentified	0.03	2.65
	119.87	6.91	C_6/H_6 in G units	0.05	4.42
	115.71	6.69	G C_5/H_5; P $C_{3,5}/H_{3,5}$	0.15	13.27
	111.18	6.9	G C_2/H_2	0.07	6.19
	111.03	7.36	C_5 in G units estherified at C-4; C_2 or C_6 in phenylcoumarans	0.01	0.88
	109.91	7.09	G C_2/H_2 or 4-O-5	0.03	2.65
	71.37	4.7	C_α/H_α in β-O-4	0.01	0.88
	61.92	4.06	Cγ/Hγ in P units	0.01	0.88
	60.43	3.36	Cγ/Hγ in side chains	0.07	6.19
	56.24	3.71	methoxy	1.13	100
	39.92	2.45	DMSO	0.13	11.5
	34.71	1.63	unidentified	0.01	0.88
	29.18	1.21	CH signals in extractives and aliphatic lignin chains	0.01	0.88
	17.13	1.09	unidentified	0.02	1.77
HW	115.57	6.65	G C_5/H_5; P $C_{3,5}/H_{3,5}$	0.06	3.21
	107.05	7.29	S $C_{2,6}/H_{2,6}$ with carbonyl at α-position of side chain	0.03	1.6
	104.07	6.59	S $C_{2,6}/H_{2,6}$	0.19	10.16
	71.58	4.14	C_α/H_α in β-O-4	0.01	0.53
	71.5	3.75	furanose OH	0.02	1.07
	67.48	4.14	γ-ethers	0.01	0.53
	64.24	3.30	C_γ /H_γ	0.03	1.60
	60.06	3.63	various C_γ /H_γ in side chain	0.56	29.95
	56.25	3.71	methoxy	1.87	100
	54.04	3.03	C_β/H_β in β-1	0.02	1.07
	52.16	2.24	solvent	0.01	0.53
	40.03	2.45	DMSO	0.09	4.81
	33.82	2.19	benzylic CH_2	0.01	0.53
	29.2	1.2	CH signals in extractives and aliphatic lignin chains	0.05	2.67
	26.64	2.45	unidentified	0.01	0.53
	24.69	1.45	CH signals in extractives and aliphatic lignin chains	0.02	1.07
	22.76	0.81	solvent	0.07	3.74
	15.4	1.06	unidentified	0.15	8.02

Table B-2. (continued)

Lignin feedstock	Signal location (^{13}C)	Signal location (^{1}H)	Designation [12, 69, 164, 166]	Absolute intensity	Relative abundance w.r.t. methoxy
SW	121.11	6.51	unidentified	0.01	0.92
	115.63	6.65	G C_5/H_5; P $C_{3,5}/H3_{3,5}$	0.19	17.43
	110.14	7.1	G C_2/H_2	0.01	0.92
	72.79	3.7	furanose OH	0.01	0.92
	65.14	3.34	aryl glycerol	0.02	1.83
	60.46	3.37	C_γ /H_γ in side chains	0.02	1.83
	60.25	4	C_γ /H_γ in P units	0.04	3.67
	55.58	3.71	methoxy	1.09	100
	39.98	2.45	DMSO	0.05	4.59
	33.7	2.19	benzylic CH_2	0.03	2.75
	28.97	1.19	CH signals in extractives and aliphatic lignin chains	0.09	8.26
	24.6	1.45	CH signals in extractives and aliphatic lignin chains	0.02	1.83
	24.22	1.12	unidentified	0.14	12.84
	22.59	0.81	solvent	0.14	12.84
	18.46	1.64	unidentified	0.01	0.92
	16.07	1.15	unidentified	0.2	18.35
SG	145.23	7.51	C_α/H_α in conjugated esters	0.02	1.64
	130.7	7.49	$C_{2,6}/H_{2,6}$ in P units	0.06	4.92
	128.55	6.99	F C_6/H_6	0.04	3.28
	115.73	6.65	G C_5/H_5; P $C_{3,5}/H3_{3,5}$	0.26	21.31
	111.48	7.28	C_5 in G units estherified at C-4; C_2 or C_6 in phenylcoumarans	0.01	0.82
	104.03	6.62	S $C_{2,6}/H_{2,6}$	0.03	2.46
	64.15	3.29	C_γ /H_γ in phenylcoumaran	0.01	0.82
	63.17	4.18	C_γ /H_γ with sterified γ-OH	0.03	2.46
	60.02	3.56	C_γ /H_γ in side chains	0.08	6.56
	59.89	4.11	C_γ /H_γ in P units	0.04	3.28
	56.02	3.7	methoxy	1.22	100
	39.88	2.45	DMSO	0.1	8.2
	33.85	2.17	benzylic CH_2	0.01	0.82
	31.77	1.33	CH signals in extractives and aliphatic lignin chains	0.01	0.82
	29.1	1.19	CH signals in extractives and aliphatic lignin chains	0.1	8.20
	26.87	2.43	unidentified	0.01	0.82
	22.69	0.81	solvent	0.07	5.74
	15.5	1.06	high field alkyls	0.17	13.93
	14.48	0.8	high field alkyls	0.03	2.46

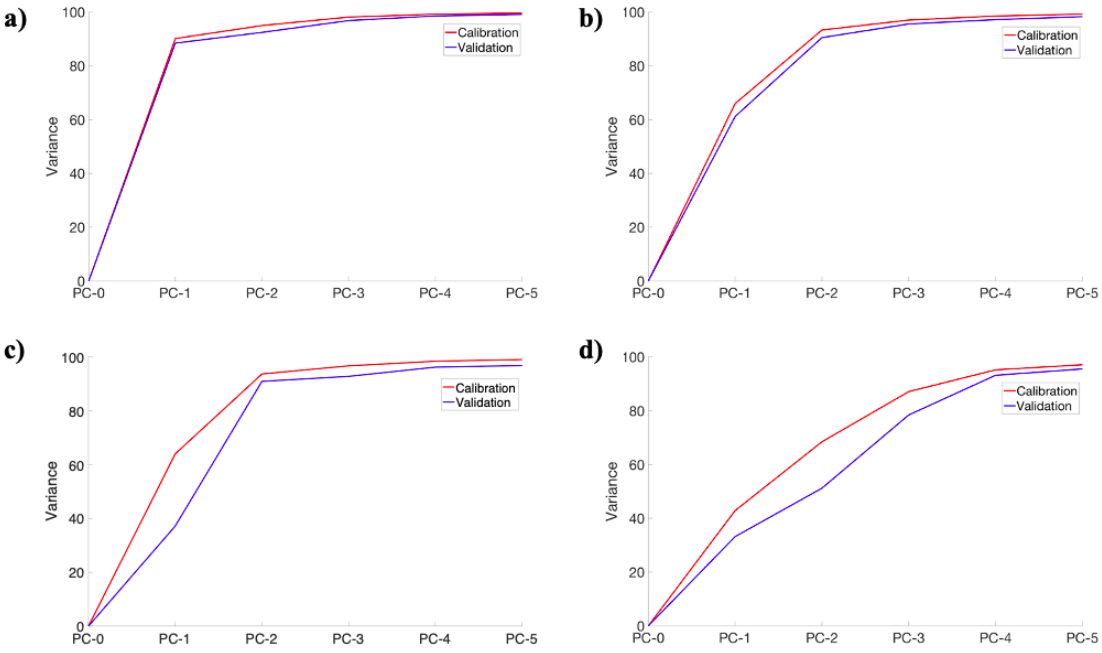


Figure B-6. Explained variances against principal components of a) pyrolyzed, b) all lignin reduced to 1050 °C, c) all lignin reduced to 2000 °C, and d) all lignin reduced to temperatures of 1050, 1500, and 2000 °C. These results are part of PCA shown in Figure 3-8.

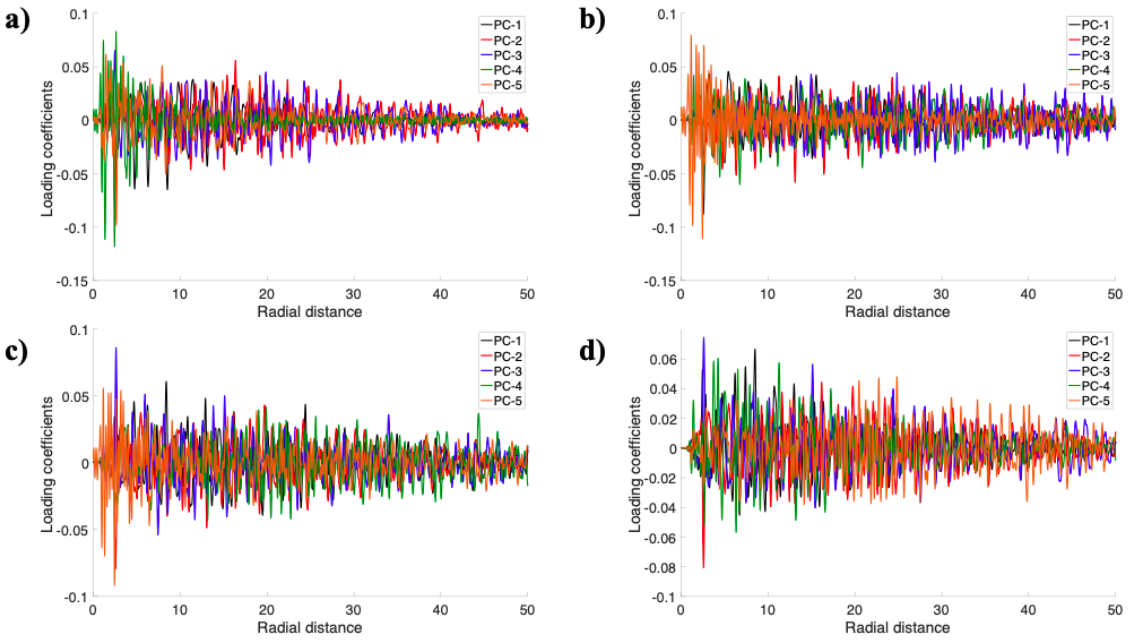


Figure B-7. Loadings against radial distance of each principal components of a) pyrolyzed, b) all lignin reduced to 1050 °C, c) all lignin reduced to 2000 °C, and d) all lignin reduced to temperatures of 1050, 1500, and 2000 °C. These results are part of PCA shown in Figure 3-8.

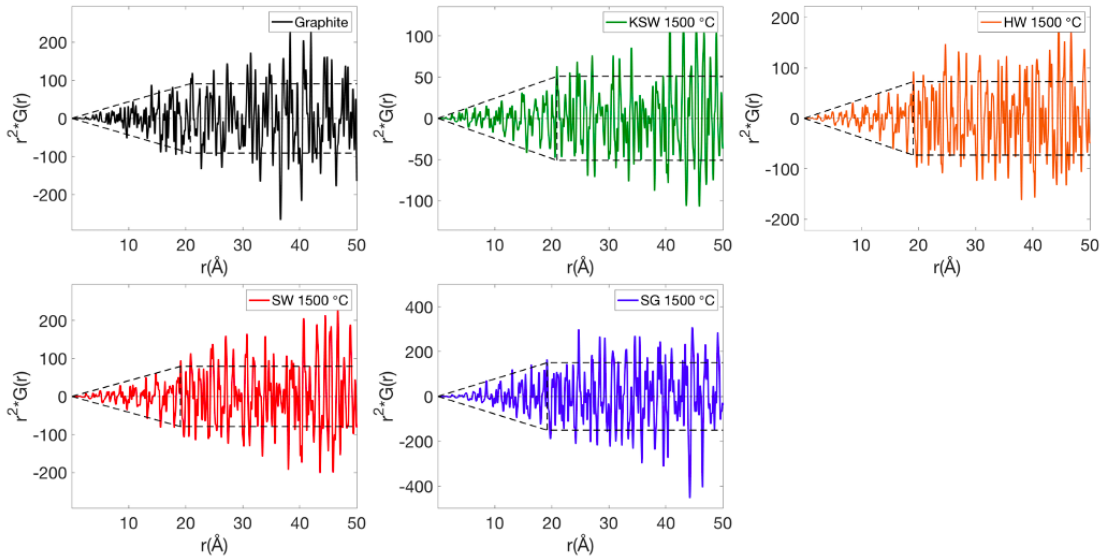


Figure B-8. Envelope function of $r^2G(r)$ for graphite standard and lignin carbons reduced at 1500 °C.

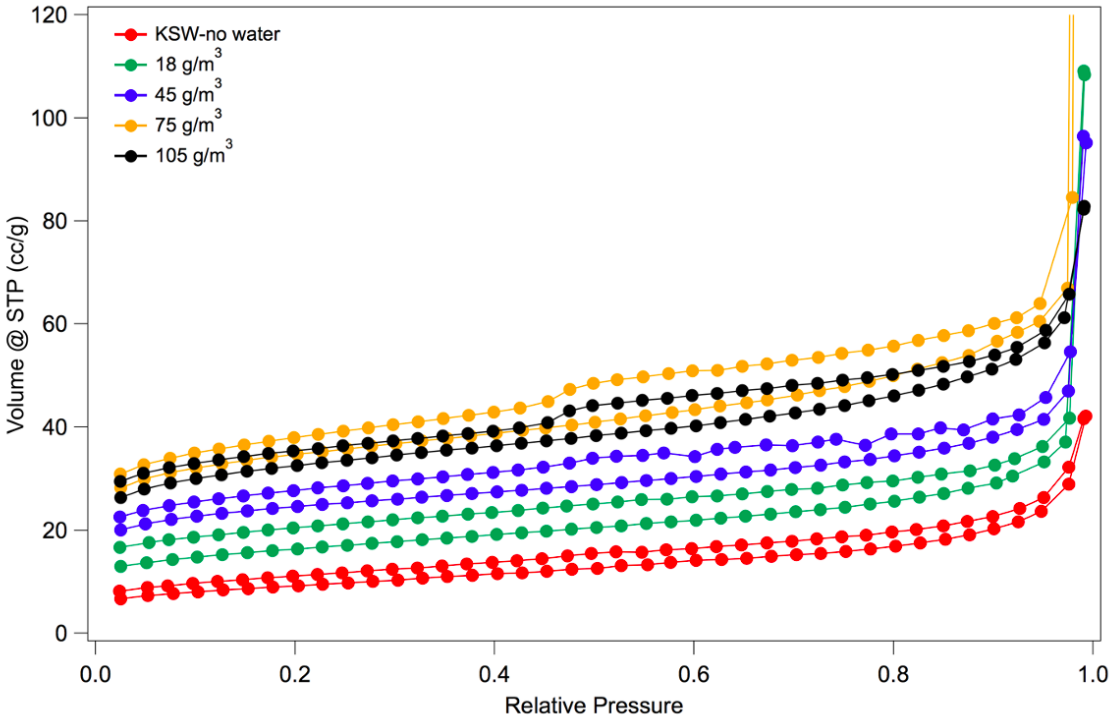


Figure B-9. Kraft softwood lignin under pyrolysis to different water content evaluating isotherms during desorption and adsorption respect to relative pressure.

VITA

Valerie García-Negrón was born in 1988 and raised in Ponce, Puerto Rico. She received a Bachelor of Science in Chemical Engineering from the Polytechnic University of Puerto Rico in 2012. From 2011 to 2014, she participated in several research internship appointments at Oak Ridge National Laboratory (ORNL) under the mentoring of Dr. Edgar Lara-Curzio from the Materials Science and Technology Division, where she characterized and evaluated ceramic seals in solid oxide fuel cells. By 2015, her passion for science encouraged her to enroll in a graduate program in Materials Science and Engineering (MSE) at the University of Tennessee in Knoxville jointly advised by Dr. David Keffer and Dr. David Harper. Her research on biomaterials motivated collaboration with the Center for Renewable Carbon and ORNL. In 2017 Ms. García-Negrón completed a Master of Science in MSE and continued the path towards a doctorate with the same group. Her current research is to understand processing-property-structure relationships of lignin carbon composites for energy storage applications. Valerie's research output consists of seven journal articles, accepted beam time proposals at national laboratories, and numerous posters and oral presentations. A recent achievement includes the 2^{nd} prize 2020 Graduate Student Award from the Cellulose and Renewable Materials Division from the American Chemical Society. Moreover, Valerie participated in the 21^{st} National School on X-ray and Neutron Scattering. Her current goals focuses in developing a career in material sciences. She wants to acquire a research position, learn managing skills, and increase her professional network. On the personal aspect she aspires to travel to other countries, become a stargaze hobbyist, and spend quality time with family.